

Spectral Domain Optical Coherence Tomography System Development for

In Vivo Ophthalmic Imaging

by

Mingtao Zhao

Department of Biomedical Engineering
Duke University

Date: September 17, 2009

Approved:

Joseph A. Izatt, Supervisor

David J. Brady

Vo-Dinh Tuan

Adam P. Wax

Anthony N. Kuo

Dissertation submitted in partial fulfillment of
the requirements for the degree of Doctor
of Philosophy in the Department of
Biomedical Engineering in the Graduate School
of Duke University

2009

ABSTRACT

Spectral Domain Optical Coherence Tomography System Development for

In Vivo Ophthalmic Imaging

by

Mingtao Zhao

Department of Biomedical Engineering
Duke University

Date: September 17, 2009

Approved:

Joseph A. Izatt, Supervisor

David J. Brady

Vo-Dinh Tuan

Adam P. Wax

Anthony N. Kuo

An abstract of a dissertation submitted in partial fulfillment of the requirements for the degree of Doctor of Philosophy in the Department of Biomedical Engineering in the Graduate School of Duke University

2009

Copyright by
Mingtao Zhao
2009

Abstract

Since its inception, spectral-domain optical coherence tomography (SDOCT) has become a powerful tool for noninvasive imaging of the human eye. In this manuscript, I describe the development of multiple low-cost, high resolution, real-time SDOCT constructions and imaging techniques optimized for rapid 3D imaging and analysis of the human eye in vivo. I have first derived the relationship of dispersion compensation coefficients in the complex conjugated case in 2006. Phase techniques such as polarization sensitive OCT (PSOCT) and Doppler OCT are described for extracting functional information from SDOCT imaging of the retina. A unique phase unwrapping method is presented to measure the total reflectivity, accumulative retardance, and fast axis orientation of the retinal nerve fiber layer (RNFL). A means to segment the polarization scrambling layer of the retinal pigment epithelium employing single camera sequential scan based PSOCT is shown. As an extension, a synthetic wavelength method will also be introduced for phase unwrapping in cellular imaging. Finally, an algorithm for 3D refraction correction accounting for refraction of OCT light in the cornea is described. 3D refraction correction of volumetric corneal datasets allows for the accurate estimation of corneal optical power, thickness, and wavefront aberrations from the corneal surfaces via Zernike spectrum analysis for clinical usage.

Dedication

Dedicated to my parents and wife.

Contents

Abstract	iv
List of Tables	ix
List of Figures	x
Acknowledgements	xiv
1 Introduction.....	1
1.1 Spectral Domain Optical Coherence Tomography	1
1.2 Retinal Imaging and Glaucoma.....	8
1.3 Anterior Segment Imaging, LASIK and Clinical Significance.....	15
1.4 Optical Coherence Tomography Technology Development for Retinal Imaging, Doppler Imaging, Synthetic Wavelength Phase Unwrapping.....	22
1.5 Polarization Sensitive Optical Coherence Tomography for Retinal Imaging...	23
1.6 Extraction of Clinical Refractive Parameters and Ocular Wave Aberration Measurement Using SDOCT.....	25
2 Optical Coherence Tomography Technology Development for Retinal Imaging and Phase Imaging	28
2.1 High Speed Fiber Based SDOCT for Retinal Imaging.....	28
2.1.1 Introduction	28
2.1.2 Methods.....	29
2.1.3 Dispersion Issue in Retina.....	31
2.1.4 Dispersion Issue in Complex Conjugate Case in Retina.....	34
2.1.5 Results.....	37
2.2 Extension of OCT Using Phase Sensitive Methods.....	40

2.2.1	Retinal Doppler Imaging.....	40
2.2.2	Methods and Results to Remove Doppler Bulk Motion.....	41
2.2.3	Methods and Results of Phase Unwrapping Using Synthetic Wavelength..	47
2.3	Summary.....	54
3	Functional Imaging with Polarization Sensitive SDOCT	56
3.1	Introduction.....	56
3.2	Simulation and Polarization State Selection	58
3.3	Materials and Methods of Free Space Based PSOCT.....	64
3.4	Materials and Methods of Fiber Based PSOCT	74
3.5	Results of Fiber Based PSOCT	77
3.6	Summary.....	79
4	Anterior Segment Imaging and Extraction of Clinical Refractive Parameters	81
4.1	Introduction.....	81
4.2	Methods of Anterior Segment Imaging.....	84
4.2.1	Nontelecentric Correction.....	86
4.2.2	3D Refraction Correction.....	87
4.2.3	Zernike 3D Interpolations for Radial Scan Patterns.....	90
4.3	Extraction of Clinical Refractive Parameters and Wave Aberration.....	94
4.3.1	Corneal Thickness Mapping.....	94
4.3.2	Corneal Wavefront Aberration Analysis	97
4.3.3	Refractive Curvature, and Best Fit Sphere Analysis	98
4.3.4	Measurement Refractive Index of Human Cornea.....	100

4.4	Statistical Experimental Design for Clinical Application	104
4.4.1	Statistical concepts	104
4.4.2	Preliminary Pilot Clinical Study Results.....	111
4.5	System Calibration and Phantom Results.....	112
4.5.1	Lateral Scanning Range Calibration	112
4.5.2	Axial Scanning Calibration	113
4.6	In vivo Results.....	117
4.6.1	Radial Scanning Mode.....	117
4.6.2	Error Analysis.....	128
4.6.3	Raster Scanning Mode	131
4.7	Summary.....	134
5	Future Works in Spectral Domain Optical Coherence Tomography.....	136
5.1	From High Speed SDOCT to Ultra High Speed SDOCT	136
5.2	Fiber Based Polarization Sensitive OCT.....	136
5.3	Brewster Angle to Improve Anterior Segment Imaging.....	137
5.4	Cellular Corneal Imaging Based on Light Scattering.....	139
5.5	Estimation of the Wave Aberration of Each Component in the Cornea.....	140
	References	141
	Biography.....	150

List of Tables

Table 1: Typical approaches for PS-OCT	24
Table 2: Measurement results of a phantom rigid contact lens.....	115
Table 3: Patient study---Curvature of top surface (<i>units in mm</i>)	119
Table 4: Patient study---Curvature of second surface (<i>units in mm</i>)	121
Table 5: Patient study---Overall corneal power (<i>units in Diopters</i>).....	122

List of Figures

Figure 1: Schematic layout of spectral domain optical coherence tomography	2
Figure 2: The human retinal structure.	9
Figure 3: Illustration of GDx scanning laser polarimetry.....	11
Figure 4: Corneal power calculation	20
Figure 5: Summary of the three main research projects	27
Figure 6: System design for real time SDOCT	29
Figure 7: The procedure for dispersion compensation.....	32
Figure 8: Complex conjugation	37
Figure 9: Measured SDOCT system sensitivity as a function of depth.....	38
Figure 10: Typical retinal SDOCT imaging results.....	39
Figure 11: Doppler imaging results.....	41
Figure 12: Doppler bulk motion removal.....	44
Figure 13: Doppler image after bulk motion removal.....	44
Figure 14: Doppler flow image	45
Figure 15: OCT elastography.....	48
Figure 16: Traditional phase unwrapping.....	49
Figure 17: Optical coherent signal at different central wavelengths	52
Figure 18: Simulation results of synthetic wavelength for phase unwrapping.	53
Figure 19: Phase images of human epithelial cheek cells.....	54
Figure 20: Illustration of the birefringence effects.....	58

Figure 21: Collagen fiber model and input polarization state scattering simulation.....	59
Figure 22: The absolute value of scattering electric field (customized in Matlab).....	61
Figure 23: The wavefront of light scattering in a collagen fiber (customized in Matlab) .	62
Figure 24: Customized FEM simulation	63
Figure 25: Schematic of the PSOCT system.....	64
Figure 26: The relationship between normalized OCT intensity and birefringence parameters.....	65
Figure 27: Fall off of the free space based polarization sensitive OCT.....	66
Figure 28: Quarter wave plate calibration.....	68
Figure 29: Fast axis orientation calibration of a quarter waveplate.....	69
Figure 30: Calibration of Berek compensator.....	70
Figure 31: In vivo human retinal imaging results	72
Figure 32: Illustration of fiber based polarization sensitive OCT system.....	75
Figure 33: Calibration results of the fast axis orientation.....	77
Figure 34: Retardance calibration results.....	78
Figure 35: Corneal imaging system	85
Figure 36: Illustration of the scanning distance D	86
Figure 37: Field curvature caused by the nontelecentric imaging optics.....	87
Figure 38: Demonstration of refraction correction	88
Figure 39: Radial scanning pattern. The scanning B-scan is designed to sweep through the apex.....	90
Figure 40: Demonstration of the re-sampling issue in the radial scanning pattern	91
Figure 41: Zernike fitting	93

Figure 42: Principle of searching intersection points between the surface normal equation of epithelial and refraction-corrected endothelial surface.....	95
Figure 43: Illustration of different Zernike wave aberration errors.....	97
Figure 44: Illustration of wavefront aberration analysis using Zernike spectrum analysis and ray tracing.....	98
Figure 45: Float images of different 3D fitting of a phantom contact lens.....	100
Figure 46: Saturated corneal image at perpendicular incidence case.....	102
Figure 47: Corneal image captured at a tilting incidence angle.....	103
Figure 48: Graphic representation of Bland-Altman plot.....	109
Figure 49: Lateral resolution calibration of SDOCT.....	113
Figure 50: Maximum imaging depth calibration using glass cover slip.....	114
Figure 51: Thickness map of RGP contact lens phantom.....	116
Figure 52: Best spherical fitting residual errors after 3D refraction correction.....	117
Figure 53: <i>In vivo</i> corneal image with radial scanning range of 6mm.....	118
Figure 54: Pachymetry mapping of an <i>in vivo</i> cornea.....	119
Figure 55: Comparison between OCT and topography.....	124
Figure 56: Comparison between OCT and Pentacam.....	125
Figure 57: Comparison between Topography and Pentacam.....	126
Figure 58: Performance summary of SDOCT, Pentacam and Topography.....	127
Figure 59: Sag error analysis.....	128
Figure 60: Calibration error analysis.....	130
Figure 61: 3D refraction correction.....	132

Figure 62: Three dimensional refraction correction and corneal thickness mapping after refraction correction processing..... 133

Figure 63: The incidence and refraction angle of the epithelium surface of an in vivo cornea..... 138

Acknowledgements

The author would like to thank his academic mentor Prof. Joseph A. Izatt of Duke University for his detailed instructions during his graduate education. Special thanks are extended to ophthalmic collaborator Prof. Anthony Kuo, M.D. , post-doctoral advisors Robert J. Zawadzki, Ph.D., Brian E. Applegate, Ph.D. and Yimin Wang, Ph.D. The support and help from family and the entire colleague was greatly appreciated, without which this effort could not have been completed. This research was sponsored in part by the National Institutes of Health and the Whitaker Foundation.

1 Introduction

1.1 Spectral Domain Optical Coherence Tomography

Spectral domain optical coherence tomography (SDOCT) also called Fourier domain OCT was first reported in optics communications in 1995[1]. Since there is no scanning component in the reference arm and thus can capture all the depth information in a single shot, SDOCT has demonstrated a ultra high speed, very stable phase, large sensitivity over traditional time domain OCT (TDOCT) as a non contact imaging technique . The imaging axial speed of SDOCT is only limited by the performance of photo detectors; the reported highest axial scan rate is up to 600 MHz[2] which is much faster than that of 4 KHz of a typical TDOCT system. The developments of broad band source, tunable laser source[3] and adaptive optics[4] have further pushed the axial resolution of SDOCT on the order of 2 μm .

The principle of SDOCT is based on traditional interferometer with broad band source[5]. The reference arm is fixed in SDOCT. The scattering back light from both reference arm and sample will cross correlate and then generate an interference fringe. Comparing to single wavelength based interferometer, the broad band wavelengths causes phase washout out of a certain optical path also call coherent length, l_c . The depth information is coded by this coherent length. After some mathematical decoding manipulation, mainly Fourier transform with respect to wave number, the sample

reflectivity, sample velocity can be retrieved individually. The schematic layout of SDOCT is illustrated in figure1. The mathematical description is illustrated in the following paragraph.

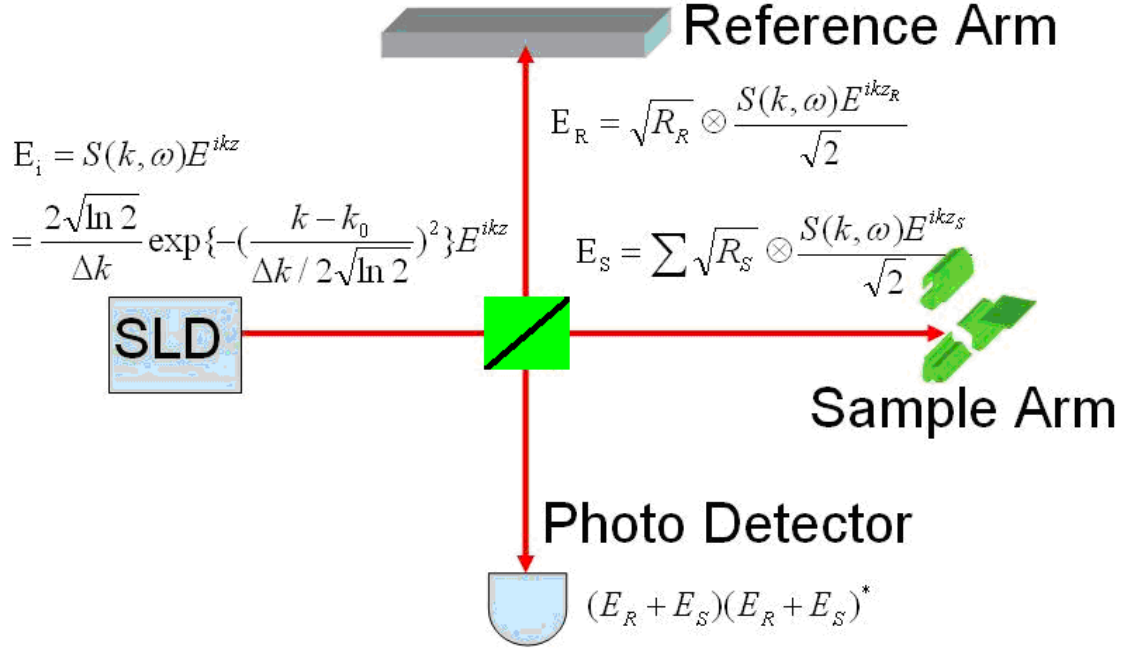


Figure 1: Schematic layout of spectral domain optical coherence tomography

Electric field is represented as scalar, stationary, ergodic real signal without considering polarization, quantization and dispersion for simplification. The scattering light signal in a single scattering case is described as following[1],

$$D[k] = [\sqrt{R_r} \sqrt{s(k)} E_R + \sqrt{R_s} \sqrt{s(k)} E_S] [\sqrt{R_r} \sqrt{s(k)} E_R + \sqrt{R_s} \sqrt{s(k)} E_S]^* \quad (1a)$$

$$D[k] = s(k) \{ R_r |E_R|^2 + R_s |E_S|^2 + 2\sqrt{R_r R_s} \cos(2k\Delta z) \} \quad (1b)$$

Where k is the wave number, $D[k]$ is interference fringe signal,* means complex conjugate. E_R and E_S is the electric field of reference and sample arm separately; R_r and R_s is the reflectivity of reference and scattering sample. Δz is the optical path difference between reference and sample arms. The source power spectral density, $s(k)$ is,

$$s(k) = \frac{2\sqrt{\ln 2}}{\Delta k \sqrt{\pi}} \exp\left\{-\left[\frac{(k - k_0)2\sqrt{\ln 2}}{\Delta k}\right]^2\right\} \quad (2)$$

Considering a normal Gaussian distribution in the form of $f(x) = \frac{1}{\sigma\sqrt{2\pi}} \exp\left(-\frac{(x - x_0)^2}{2\sigma^2}\right)$, the full width at half maximum (FWHM) is $2\sqrt{2\ln 2}\sigma$ for above normal distribution of equation (2). In this case $\sigma = \frac{\Delta k}{2\sqrt{2\ln 2}}$, hence Δk is the FWHM for Gaussian distribution spectrum density source. To get the contrast signal which is the reflectivity of scattering points at different depths, a Fourier Transform with respect to wave number k is employed applying to the cross correlation term,

$$\int_{-\infty}^{\infty} s(k) 2\sqrt{R_r R_s} \cos(2k\Delta z) dk = 2\sqrt{R_r R_s} \cos(2k_0\Delta z) \exp\left[-\left(\frac{2\Delta z\sqrt{\ln 2}}{l_c}\right)^2\right] \quad (3)$$

Where k_0 is the central wave number; λ_0 is the central wavelength and l_c is the coherence length which determines the axial resolution of OCT.

$$l_c = \frac{2 \ln 2 \lambda_0^2}{\pi \Delta \lambda} \quad (4)$$

Hence the axial resolution of OCT is only dependent on the central wavelength and bandwidth instead of numerical aperture (NA), which makes it possible to get super axial resolution without using a higher NA. For example, increasing the bandwidth of light sources will directly improve the depth resolution with the same NA. The transverse resolution[6] of the OCT is dependent on the spot size, $\omega(z)$,

$$\omega(z) = \omega_F \sqrt{1 + \left(\frac{\lambda_0 z}{\pi \omega_F^2}\right)^2} \quad (5a)$$

$$\omega_F = \frac{\omega_p f}{\sqrt{z_1^2 + \pi^2 \omega_p^4 / \lambda^2}} \quad (5b)$$

Where ω_p is the minimum beam waist of the probe beam before focusing; f is the imaging focal length; z_1 is the distance between the beam waist of the unfocused probe beam and the imaging lens focal plane; z is the distance from the imaging beam waist of the imaging beam. As an extension, the transverse resolution of optical coherence microscopy (OCM)[7] is determined by the NA, which is

$$\text{Transverse_Resolution} = 1.22 \frac{\lambda_0}{NA} \quad (6)$$

In spectrometer based SDOCT, the limited spectrometer resolution will determine the maximum imaging depth of SDOCT. If the highest interferometric fringe

frequency is Z_{\max} , according to the property of Fourier transform, the corresponding period of the highest harmonic fringe[8] is

$$\delta k = \frac{1}{2} \frac{2\pi}{nZ_{\max}} = \frac{\pi}{nZ_{\max}} \quad (7)$$

n is the refractive index. According to Nyquist sampling theorem[9], the spectrometer has to resolve $\delta k / 2$ to identify the un-aliasing OCT signal.

Considering $\delta k = \frac{2\pi\lambda^2}{\delta\lambda}$, the measurement range of spectrometer is

$$Z_{\text{range}} = \frac{\lambda^2}{4n\delta\lambda} \quad (8)$$

Accordingly to get a target axial measurement depth, Z_{target} , the spectrometer resolution $\delta\lambda$ should at least be

$$\delta\lambda = \frac{\lambda^2}{4nZ_{\text{target}}} \quad (9)$$

The cross correlation electric field is linearly wavelength-dispersive on the focal plane of an infrared linear scan CCD (charge-coupled device) target. So the CCD detector can only discretely capture the real part of complex electric field. The lost imaginary part of the electric field, which is phase-shift 90° with respect to the real part, inevitably introduces the complex conjugation issue. The complex conjugate issue will also influence the dispersion compensation coefficients in the retinal SDOCT. I have first

addressed this issue in 2006 and the theoretical prediction result agrees very well with the experimental results. Since spectrometer based SDOCT outputs discrete electronic signal, discrete Fourier Transform (DFT) instead of continuous Fourier transform is implemented to retrieve the depth dependent reflectivities and phases which is associate with each layer. It is generally represented[10] by:

$$D[z_n] = \sum_{m=1}^M D[k_m] \exp[-j2\pi k_m z_n], n \in \{1, M\} \quad (10)$$

$D[k_m]$ is the discrete version of $D[k]$. The discrete imaging pixels of CCD spectrometer have a limit space ($14\mu\text{m}$) in our case which will form a fall-off of the measurement range. Mathematically the discrete pixel space which can be represented as a rectangular function, $\text{rect}(\frac{k}{\delta k / 2})$, will generate a depth dependent reflectivity

, $R(z)$:

$$R(z) = \left(\frac{\pi \delta \lambda \sin[\pi \delta \lambda \cdot z / \lambda^2]}{\lambda^2 \pi \delta \lambda \cdot z / \lambda^2} \right)^2 \quad (11)$$

Above Sinc function is usually called fall-off effect[11]. The equation shows that the magnitude of the reflectivity, $R(z)$, will be reduced with respect to increasing, z , by the limited spectrometer resolution $\delta \lambda$. To design a spectrometer with good performance, we have to balance the fall-off of, $R(z)$, measurement range Z_{range} , pixel

size and the overall length of CCD target on the focal plane. In addition, we should consider the Gaussian beam spot size of the CCD arrays to select suitable imaging lens.

The interferogram of SDOCT signal is detected based on the photoelectric signal. The photodiode sensor will generate photocurrent, which is close to shot-noise limited and has better linearity, offset and bandwidth performance compared to voltage measurement. The sensitivity of SDOCT has a much better performance than time-domain OCT (TDOCT). The main reason is SDOCT has N linear detectors which will greatly lower the noise standard deviation levels because of the averaging effects of Fourier transform. According to R. Leitgeb[12], the approximation sensitivity of SDOCT is :

$$\Sigma_{SDOCT} = \frac{[\frac{\rho\eta\tau P_0}{Nh\nu_0}]^2 \gamma_s \gamma_r R_r}{\frac{1}{N} \sigma_{noise}^2} = \frac{[\frac{\rho\eta\tau P_0}{h\nu_0}]^2 \gamma_s \gamma_r R_r}{N(\sigma_{shot}^2 + \sigma_{excess}^2 + \sigma_{receiver}^2)} \quad (12)$$

Where ρ is spectrometer efficiency; η is the detector quantum efficiency; τ is integration time; P_0 is the overall incident sample power; h is the Plank constant; ν_0 is the central frequency; N is the overall pixel numbers of the CCD detector ; γ_s and γ_r are the exit power from the sample and reference arm of the interferometer; R_r is the reflectivity of the reference arm; The rests are the different noises. Equation (12) shows that the sensitivity advantages of SDOCT over TDOCT around 30 dB. Another SDOCT is

called swept source OCT (SSOCT)[1]. Basically the encoded sample spectrum is obtained by sweeping a broad band spectrum generated from a narrow band laser source. Its sensitivity analysis is similar to SDOCT and extended by Choma in 2003[10]. In summary, SDOCT has two main advantages over TDOCT:

- SDOCT permits much faster image acquisition rates (up to 30,000 A-scans/sec in commercially available systems) than the conventional time-domain approach (4 KHz). The most recently reported imaging speed in biological imaging is up to 600MHz in swept source OCT .
- The sensitivity of SDOCT theoretically is in excess of 100dB with incident power of 700 μ w and it is 20-30 dB higher than that of TDOCT.

The revolutionary advancement of SDOCT has recently made it as a powerful new tool for noninvasive human retinal imaging. I have demonstrated *in vivo* ophthalmic imaging of human retina. Those projects are volumetric retinal imaging, which include Doppler, optical coherence elastography and synthetic wavelength imaging, polarization sensitive OCT, anterior segment imaging and extraction of clinical refractive parameters from spectral domain-optical coherence tomography of the cornea.

1.2 Retinal Imaging and Glaucoma

The eye is usually divided into two parts, the anterior segment and posterior segment. The anterior segment includes cornea, aqueous humor, iris, and crystalline

lens. The posterior segment consists of vitreous gel, optic nerve, macula, fovea and retina. The anatomy of eye is illustrated in the following figure.

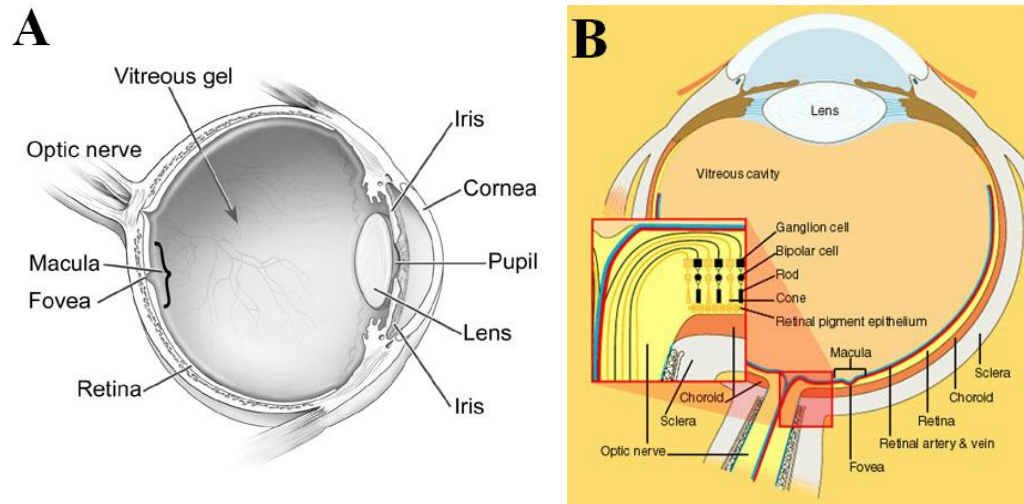


Figure 2: The human retinal structure.

A: Anatomy of eye. (National Eye Institute, National Institutes of Health Reference # NEA09). B: the retina part mainly consists of optical nerve fiber, ganglion cell, bipolar cell, rod & cone, and retinal pigment epithelium. Source: www.kellogg.umich.edu/.../section-retina.htm. University of Michigan

Glaucoma is the leading cause of visual impairment for Americans[13], which is a group of diseases which can degrade or even damage the optical nerve. Basically glaucoma is related to the dysfunction or death of retinal ganglion cell[14]. Currently there are five imaging tools for glaucoma detection, which are fundus camera, confocal scanning laser ophthalmology (CSLO), scanning laser polarimetry and optical coherence tomography respectively.

Fundus camera is a specially designed ophthalmoscope[14] which utilizes a camera to record the inaccessible interior surface of the eye. The fundus photography can provide good contrast images of the retina, optic disc, macula and posterior pole. Combining with angiography, a very high-contrast image of the vessels in retina can be produced. However, fundus camera can only give an en-face image of the retina. No depth information or quantitative information of the optic nerve fiber layer can be provided.

Heidelberg Retina Tomograph (HRT, Heidelberg Engineering GmbH; Heidelberg, Germany) is a kind of confocal scanning laser ophthalmology technique[14], which employ a pinhole to select the image plane and reject the scattering light which is out of focus. CSLO can achieve high resolution image with depth selectivity and is particularly useful in mapping the retinal surface around optic nerve head (ONH). In addition, CSLO can provide approximately estimation of the thickness of optic nerve fiber layer. Clinically the thickness estimation is not that accurate. So it is difficult to be quantitatively used for glaucoma discrimination.

Scanning laser polarimetry was first demonstrated for *in vivo* glaucoma diagnostic in 1995. The latest version of above device is called the GDx (Carl Zeiss Meditec, Vista, California). The current GDx can both measure the birefringence effects in cornea and retina. Since the retinal optic nerve fiber layer (RNFL) is on the top surface

of the retina with a diameter around 120 nm[15], the parallel bundled retinal nerve fibres have different refractive index with respect to the different vibration direction of the incident electric field. As a result, the RNFL will introduce a amount of phase shift which is related to the orientation and thickness of the RNFL. Estimation of the thickness of RNFL can be obtained by converting from a 0.67nm of phase shift equal to 1 μm of fiber[14]. With the help of computer artificial intelligent algorithm, the thickness of the RNFL can be extracted to help discriminate the glaucoma. The new GDx-ECC method can provide more accurate estimation of a variety of parameters derived from the RNFL measurements. One disadvantage of GDx is that it can only give the overall en-face projection of the phase shift. The depth resolved information is lost. The following figure shows the phase shift (retardance) of RNFL around ONH[16].

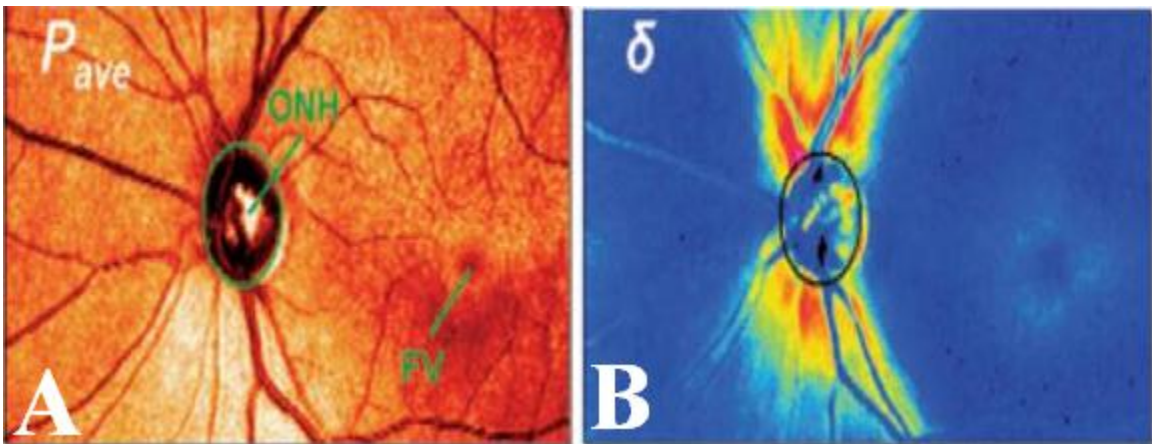


Figure 3: Illustration of GDx scanning laser polarimetry

A: The en-face reflectivity image of a retina. B: the accumulated double-pass retardance of the nerve fiber layer. The areas of yellow and red color indicate the position of retinal optic nerve fiber layer. The area of superior and inferior to the

optic nerve head have much thicker RNFL than that of nasal and temporal to the optic nerve head. Source: Dr. Zhou's paper.[16](Carl Zeiss Meditec, Vista, California).

Optical coherence tomography is a new powerful tools for glaucoma diagnostic in retina. Since its introduction in the early 1990's, optical coherence tomography (OCT) has emerged as a promising imaging modality for micrometer-scale non-invasive imaging in biological and biomedical applications. Its relatively low cost and real-time *in vivo* capabilities have fueled the investigation of this technique for applications in retinal and anterior segment imaging in ophthalmology, early cancer detection and staging in the skin, gastrointestinal, and genitourinary tracts, as well as for ultra-high resolution imaging of entire animals in embryology and developmental biology. The most successful clinical application of OCT to date by far is in noninvasive diagnosis of retinal pathologies, where the technology was first commercialized (by Humphrey Instruments, now Carl Zeiss Meditec, Inc.) and has reached significant ophthalmology market penetration in the U.S., Europe, and Japan. I have been actively involved in OCT technology development and its applications in ophthalmic imaging and biology since 2004 at Duke University.

The time-domain approach used in first-generation OCT was successful in supporting biological and medical applications, and all initial *in vivo* human clinical trials of OCT utilized this approach. Within the last several years, however, an alternate approach to data collection in OCT has been shown to have dramatic advantages in

increased system robustness, stability and signal-to-noise ratio (SNR). The “Fourier Domain” approach to OCT (FDOCT) involves acquiring as a function of optical wavenumber the interferometric signal generated by mixing sample light with reference light at a fixed group delay. Two distinct methods have been developed which employ this FDOCT approach. The first, termed Spectral-domain OCT (SDOCT)[1, 17], uses a broadband light source and achieves spectral discrimination with a dispersive spectrometer in the detector arm. The second, termed swept-source OCT (SSOCT) or Optical Frequency-Domain Imaging (OFDI)[11], time-encodes wavenumber by rapidly tuning a narrowband source through a broad optical bandwidth. Both of these techniques allow for a dramatic improvement in SNR of up to 15-20 dB over time-domain OCT because they capture the A-scan data in parallel[10, 12, 18]. This is in contrast to time-domain OCT, where destructive interference is employed to isolate the interferometric signal from only one depth at a time as the reference delay is scanned. The improved SNR of FDOCT systems may in principle be utilized to obtain higher quality images, to image deeper into samples (although the gain here is only logarithmic), or to image faster. To date, most investigations with FDOCT have taken advantage of the improved SNR for increasing the acquisition rate to perform and even exceed video-rate for high-quality cross-sectional (“B-scan”) imaging, and to perform densely sampled three-dimensional imaging in just a few seconds[19, 20]. The

dramatically improved image acquisition rate is particularly compelling for human retinal imaging applications, where established ocular exposure safety standards limited the previous generation of technology to image rates on the order of one per second. Within a short time after this discovery, the first video-rate SDOCT systems optimized for retinal imaging were implemented[19], and several companies now offer commercial SDOCT retinal imaging systems targeted for routine clinical applications.

OCT can obtain all the 3D structure of retina and thus directly measure the thickness of the RNFL with less confounding artifacts. Polarization sensitive OCT (PSOCT) can resolve the phase shift and orientation of the nerve fiber layer, which has a great advantage over GDx to detect the glaucoma based on the thickness variation of the RNFL. Doppler OCT has the potential to provide flow rate information to aid in the diagnosis or characterization of glaucoma and diseases affecting the retinal vasculature. Temporal observable changes, such as changes in thickness or flow rate, can also be used to characterize disease state. I have demonstrated the technology development of SDOCT, PSOCT and Doppler OCT for retinal imaging to help glaucoma discrimination. In the retinal imaging, cornea, aqueous, lens, vitreous and retina will mainly induce the material dispersions. I have addressed the dispersion compensation issue in complex conjugate case in my thesis. Novel synthetic wavelength for phase unwrapping and bulk motion removal based on phase techniques in Doppler imaging are also developed in

my research project.

1.3 Anterior Segment Imaging, LASIK and Clinical Significance

Laser refractive surgery (LRS) is a popular elective procedure to help individuals reduce dependence on corrective eyewear. In the United States alone, over 7 million people have already received some form of LRS (LASIK, PRK, and other variants) making LRS one of the most commonly performed of all outpatient surgeries. It is estimated that an additional 700,000 people per year in the US will continue to undergo the LASIK procedure to eliminate their need for glasses or contacts[19]. LRS has typically been performed on adult individuals 20 to 40 years old. These millions of individuals have enjoyed close to 20/20 uncorrected visual acuity on average after LRS[21, 22]. However, as all people age into late adulthood, vision invariably deteriorates from age related formation of cataracts, requiring cataract surgery for the restoration of functional vision. Based on a longitudinal study from 1995 to 2002, the estimated annual rate of cataract surgery for individuals older than 62 was 5.3% [21]. Thus, a projected 370,000 LRS patients will eventually require cataract surgery in at least one eye with a continuing need of about 37,000 per year after those initial patients.

Excimer laser refractive surgery ablates the anterior cornea to achieve a desired refractive correction for the patient. This alters the normal relationship between the anterior and posterior corneal curvatures critical to reflection based topography. Because

accurate measurements of corneal power contribute to the proper selection of intraocular lenses needed after cataract surgery, patients who have had laser refractive surgery and subsequently underwent cataract surgery have had unanticipated and undesirable refractive outcomes[21]. There continues to be no consensus method to overcome this limitation in accurately measuring corneal power after laser refractive surgery, and surgeons currently warn all these post-laser refractive surgery patients of potential “refractive surprises” after cataract surgery.

In cataract surgery, an artificial intraocular lens (IOL) is implanted to replace the refractive power lost from the removal of the natural lens (cataract). After modern cataract surgery, patients expect to be spectacle independent in part because of the accuracy in predicting the refractive power needed in the IOL. The predicted refractive power, however, depends critically on accurate measurements of the patient’s total corneal refractive power (P_t). Physically, this parameter depends upon the curvature of the anterior (epithelial) and posterior (endothelial) surfaces of the cornea, as well as the indices of refraction of the intervening media (which are well known). Currently, the most widely used instruments to measure P_t are based on corneal topography (multiple vendors), which estimate the refractive power of the cornea from measurements of the curvature of the front surface only. Assumptions are made regarding the refractive contribution of the posterior corneal surface[21, 23]. This approach provides satisfactory

outcomes for patients with normal corneas, which have a predictable relationship between their front and back curvature. However, this assumption has proven flawed for the first patients who had LRS, subsequently underwent cataract surgery, and had unsatisfactory outcomes[23].

Tomographic corneal imaging methods offer the ability to overcome the assumptions regarding the posterior curvature by directly measuring it. Three commercial clinical modalities are currently[23] available: a slit-scanner based method (Bausch & Lomb Orbscan®), a time-domain based OCT (Carl Zeiss Meditec Visante®), and a rotating Scheimpflug photography based method (Oculus Pentacam®). The slit-scanner calculates the posterior surface mathematically from the front surface[24], but there are questions regarding its ability to accurately represent the posterior surface[25]. The time-domain OCT instrument does not currently derive curvature information from its images. Because of these limitations and others, neither the slit-scanner nor time-domain OCT is used in clinical practice for quantitative evaluation of corneal curvature. The rotating Scheimpflug device takes 25 or 50 full diameter, radial pictures of the cornea and then reconstructs the anterior and posterior corneal surfaces from those photos. This device is used clinically for examining corneal curvature and deriving corneal power, though there is debate regarding the sufficiency of photographic resolution to accurately determine these parameters. None of these approaches appear

capable of meeting the rapidly oncoming demand of millions of LRS patients who chose an elective procedure to obtain 20/20 vision and will now expect the same after modern cataract surgery.

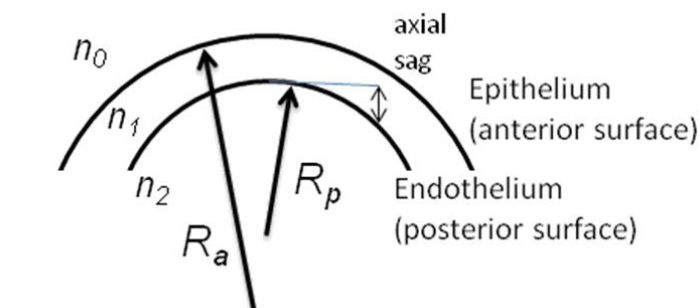
The goal of my research is to take advantage of the new generation of OCT technology to develop a new device enabling accurate characterization of both anterior and posterior corneal curvature. Along with device technology development, I have developed algorithms to extract quantitative parameters free of assumptions about the ratio of corneal curvatures including total corneal power, corneal refraction maps, anterior and posterior elevation maps, float maps and thickness maps of corneal layers. The ability to accurately measure these parameters will lead directly to a variety of clinical applications. For example, accurate determination of corneal power will allow for more reliable intraocular lens predictions and better functional results in cataract surgery after prior laser refractive surgery. With direct imaging of both surfaces of the cornea, I also calculate the wavefront aberration of the cornea. This information could allow for the theoretical creation of customized wavefront intraocular lenses for that particular cornea and eye. Accurate determination of the posterior surface of the cornea can also aid in the diagnosis of corneal ectasias. This would be especially important in attempting to discern preclinical ectatic states which would be adversely affected by ablative corneal surgeries[25]. Finally, coupled with a surgical device (excimer laser,

femtosecond laser, operating microscope), this SDOCT device could provide guidance for the surgeon's laser or blade in refractive procedures (such as for OCT guided refractive excimer ablation of irregular corneas) and in lamellar corneal surgeries (such as in deep anterior lamellar keratoplasty where the risk of intraoperative perforation and conversion to full thickness transplantation is high due to limitations of unaided depth perception). The ability to accurately quantify corneal shape and dimensions at micron level resolution offers the opportunity to vastly improve patient sight and patient outcomes for corneal based interventions.

Quantitative Keratometry

Keratometry is measurement of the refractive power of the cornea. The refractive power of an optical surface or combination of optical surfaces is measured in Diopters (D), defined as the inverse of the focal length of the surface or combination measured in meters. Under the assumption that the corneal epithelial and endothelial surfaces are spherical, formulas for calculating the total corneal refractive power are as provided in Figure 4. Accurately calculating the total refractive power requires knowledge of the radii of curvature of both the anterior and posterior surfaces. However before tomographic techniques became available, the dominant technology for Keratometry was corneal topography which could only measure the anterior surface curvature. If it is assumed that the ratio of the anterior to posterior curvature is invariant, one can obtain a

reasonably accurate approximation to the total corneal power (mean keratometric power) from the anterior surface alone by use of an empirically determined “keratometric refractive index,” n_k . Calculation of corneal refractive power by measurement of the anterior segment radius of curvature over its central 3mm and use of the keratometric index is the current clinical standard of care.



Refractive power of corneal surfaces:

$$P_a = \frac{n_1 - n_0}{R_a} \quad P_p = \frac{n_2 - n_1}{R_p} \quad P_t = P_a + P_p$$

Mean keratometric power (approximation):

$$K = \frac{n_k - n_0}{R_a}$$

Figure 4: Corneal power calculation

Definitions and equations for calculating refractive powers of the anterior surface (P_a), posterior surface (P_p), exact total corneal power (P_t), and keratometric approximation to the total corneal refractive power (K). R_a and R_p are the radii of the (assumed spherical) corneal anterior and posterior surfaces. The relevant refractive indices are $n_0=1.0$ (air), $n_1=1.376$ (corneal stroma), $n_2=1.336$ (aqueous humor), and $n_k=1.3375$ (keratometric index), Adapted from[26].

The keratometric index method of calculating corneal refractive index is invalid if the assumption of a constant ratio between anterior and posterior corneal curvatures is

altered, as occurs after laser refractive surgery. In this case, direct measurement of both corneal surfaces is necessary.

Current-generation SDOCT systems in routine use in our laboratory as well as commercial units feature $4.5\mu\text{m}$ axial resolution, which is theoretically sufficient to calculate corneal refractive power with approximately 0.25D accuracy independent of the assumptions upon which corneal topography depend. However, conventional OCT imaging faces the additional technical hurdle that cross-sectional images are built up sequentially rather than simultaneously; each sectional image is built up sequentially as the focused beam is scanned across the corneal surface. Despite utilization of a forehead rest in clinical SDOCT systems, it is difficult to immobilize the patient's head to better than $\sim 10\text{-}100\ \mu\text{m}$ during the 0.05 second required for acquisition of each standard SDOCT B-scan. Thus, as a sequential image is acquired, patient motion inevitably corrupts the true profile of the corneal surfaces sufficiently to degrade the corneal power calculation beyond an acceptable level. Indeed, the only OCT study published so far which quantified keratometric accuracy reported $\sim 0.75\text{D}$ accuracy using OCT alone[26]. The major focus of my research is to develop a 3D refraction correction algorithm and introduce a novel patient scanning interface to mitigate the inevitable patient motion and thus improve the accuracy of corneal SDOCT measurements down to that limited by the resolution of SDOCT rather than the motion of the patient.

I have demonstrated my research results on the advancement of anterior segment imaging, 3D refraction correction, corneal patchy map, corneal power, float image and wave front aberration of cornea in this thesis.

1.4 Optical Coherence Tomography Technology Development for Retinal Imaging, Doppler Imaging, Synthetic Wavelength Phase Unwrapping

I have constructed a fiber based high speed spectral domain optical coherence tomography (SDOCT) system for in-vivo retinal imaging[27-29]. The system employs a super luminescent diode (SLD) emitting at 840nm (Super SLD-371-HP) with an FWHM bandwidth of 50 nm. The theoretical axial resolution is 5.4 μm in retinal and 7.5 μm in air. The lateral resolution is around 25 μm (ZemaxTM simulation) which is depended on the corneal power and crystalline lens of the retina. The SDOCT provides detailed three dimensional (3D) structure of the human retina[30, 31]. This system is comparable in imaging speed to current generation, commercially available SDOCT systems such as the Cirrus HD-OCT (Carl Zeiss Meditec), RTVue-100 (Optovue), Spectral OCT SLO (OTI), and 3D OCT-1000 (Topcon). Doppler imaging is extended to measure the vessel flow and segment vessel in the retina. A phase algorithm is proposed to remove the bulk motion in Doppler imaging. Synthetic dual-wavelength algorithm is proposed to solve the phase wrapping issue in phase based OCT imaging[32, 33]. I have also predicted the dispersion compensation issue in the complex conjugated case[34]. Dispersion

significantly influence the image quality of OCT and the measurement accuracy of the fast axis orientation in the following polarization sensitive OCT.

1.5 Polarization Sensitive Optical Coherence Tomography for Retinal Imaging

Polarization sensitive OCT (PSOCT) was first proposed[35] in 1992 to quantify sample birefringence, and then further developed in several groups to measure the birefringence effects of skin, cornea, retina and other biological tissues[36]. Some groups use polarization effects to determine the epithelial cell nuclear sizes using angle-resolved low-coherence interferometry[37]. PSOCT provides additional contrast, such as retardance and fast axis orientation, for retinal imaging and has been shown to be sensitive to the orientation and density of the ganglion cell axons, microtubules and fibers in the RNFL and Henle's fiber layer[38-44]. In addition, PSOCT can be potentially used to aid in the diagnosis of age-related macular degeneration (AMD), which is characterized by the formation of lipoproteinaceous deposits (drusen) between the retinal pigment epithelium (RPE) and underlying structures[45]. For example, recently researchers proposed to segment the RPE using the retardance scrambling properties of RPE. Researchers mainly focus on two kinds of PSOCT which are time domain based and spectral domain based respectively[46]. The following table lists some common methods for PSOCT

Table 1: Typical approaches for PS-OCT

Time Domain		Fourier Domain	
Free space	Fiber based	Free space	Fiber based
Hee,et.al.,JOSA (B),9,903,1992	Saxer. et.al.,OL,25 1355,2000	Gotzinger.et.al.,OE, 13,10217,2005	Park. et.al.,OE 13,3931,2005
De Boer, et.al., OL 22,934,1997	Roth.et.al.,OL,26 1069,2001	Baumann,et.al.,OE 15,1054,2007	Cense.et.al.,OE 15,2421,2007
Hitzenberger.et.al. OE,780,2001			Yamari.et.al.,OE 14,6502,2006
Jiao.et.al.JBO,7,1350 1,2002			
Pircher. Et.al.,OE 12,5940,2004			

I have developed a single channel polarization sensitive SDOCT system[47] using a single spectrometer for high-speed characterization of total reflectivity, accumulative birefringence and fast axis orientation. A unique phase unwrapping algorithm was implemented to precisely detect the fast axis orientation with standard deviation less than 0.7° which is much more accurate than in contemporary PSOCT systems. A plausible approach for segmentation of the RPE relying on the combination of the standard deviation of the fast axis orientation and that of retardance is suggested, allowing for quantitative measure of the degree of depolarization of the RPE layer.

1.6 Extraction of Clinical Refractive Parameters and Ocular Wave Aberration Measurement Using SDOCT

Accurate quantitative imaging of the cornea is critical for predictable outcomes in corneal based surgical interventions. While long the standard, reflection based corneal topography to assess corneal curvature and refractive power is insufficient in an era when surgical manipulation of the corneal shape is routine and undermines the basis of reflection topography. Laser refractive surgery[26] is one particular corneal intervention that has revealed current inadequacies in measuring the cornea. Accurate measurement of corneal power is critical in applications such as the prediction of intraocular lens power needed after cataract surgery, an event which this group of patients will invariably encounter as they age into late adulthood. I have utilized images acquired using a commercially available clinical SD-OCT system (Biotigen; Research Triangle Park, NC) with a central wavelength of 840nm and a corneal adapter. Fixation was maintained by direct patient visualization of the OCT light source with the target eye. To minimize the effects of patient motion during scan acquisition, a scan protocol was developed consisting of rapid acquisition of 50 radial B-scans centered on the corneal apex, each 6mm in diameter and consisting of 1000 A-scans[48]. Total acquisition time for this sequence was 2.5s.

I have describe an algorithm[49] for quantitative image correction and clinical parameter computation which is generally applicable for any OCT sample containing

refracting interfaces and regions of different refractive indices. The algorithm is particularly suitable for quantitative correction of 3D OCT images of the cornea and anterior segment of the eye. Two specific implementations for two different scanning patterns are introduced for corneal imaging. Zernike 3D interpolation is proposed to represent the corneal surfaces (epithelium, uncorrected endothelium, and refraction corrected surfaces). This interpolation method makes it possible for the implementation of a recursive half searching algorithm (RHSA) to measure the corneal thicknesses and map them in an en face clinical view. 3D corneal volumetric refraction correction provides the foundation for generating further clinical parameters. These include known clinical ones such as wavefront analysis, asphericity, refractive curvature maps, and best fit sphere float maps as well as novel ones such as angle magnitude maps. 3D refraction correction and the accurate representation of ocular structures it creates provide an important tool in the visualization and management of ocular disease.

In summary, my thesis mainly includes three parts illustrated as following:

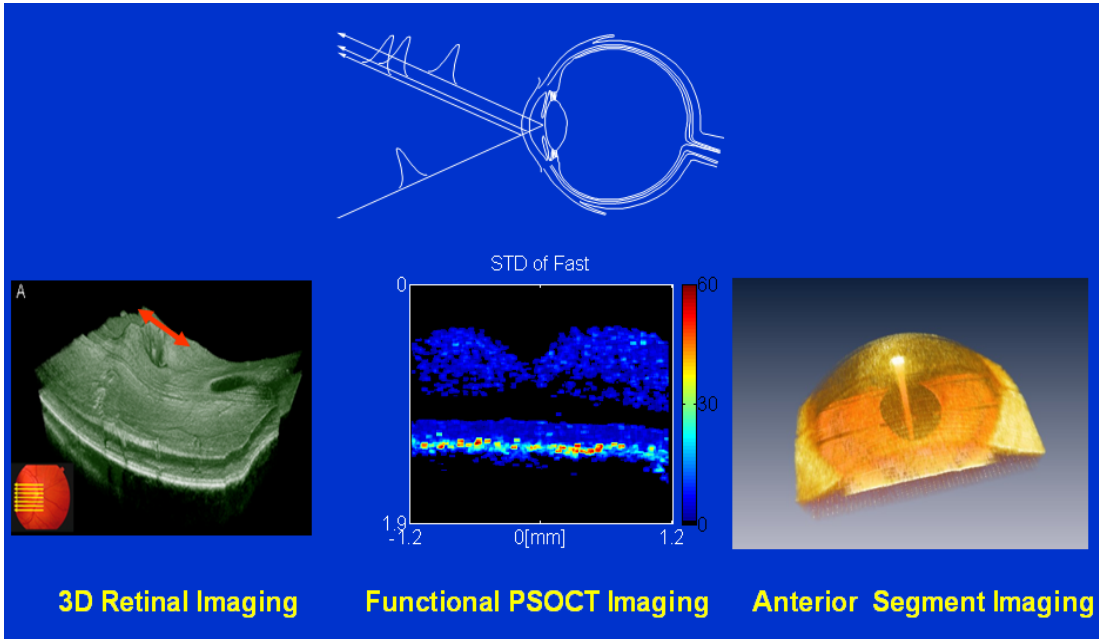


Figure 5: Summary of the three main research projects
The three main research topics are 3D retinal structure imaging, functional Doppler & polarization sensitive OCT and anterior segment imaging.

2 Optical Coherence Tomography Technology Development for Retinal Imaging and Phase Imaging

2.1 High Speed Fiber Based SDOCT for Retinal Imaging

2.1.1 Introduction

It has been more than ten years to employ OCT techniques for in vivo imaging of the human retina since the first generation of Time domain optical coherence tomography[17]. TDOCT has performed the imaging by mechanically scanning the reference arm with respect to different imaging depth. The reflectivity of biological tissues is extracted using Hilbert transform. The axial resolution is determined by the optical coherent gate of a broad band low coherence source, while the lateral resolution is limited by the Gaussian waist of the imaging beam. Recent advances around 2003 in the revolutionary development of optical coherence tomography techniques[1] based on spectral encoding by avoiding a scanning reference arm, has led to the development of Spectral Domain Optical Coherence Tomography (SDOCT). Using a Fourier transform on the scattering signals, the scattering potentials of dielectric materials can be constructed to map the inside 3D structure of imaging sample. Thus SDOCT is very suitable for high speed imaging of transparent tissue such as retina. Theoretical and experimental comparisons between SDOCT and TDOCT approaches[10, 12, 18] indicate that SDOCT systems exhibit up to 20dB higher SNR than TDOCT systems with similar illumination conditions. Besides simple structural imaging, SDOCT has also been

LS: low-cost SLD source (Superlum); OI: optical isolator; BS: 50/50 fiber beam splitter; L1, L2: aspheric collimating objectives; PP: BK-7 prism pair for dispersion compensation; ND: variable neutral density filter; SG: scanning galvanometers; L3: lens; L4 : Volk lens; L5 : air-spaced achromatic lens pair; TG: transmission grating; and LSC: line scan camera

The high-speed retinal system is shown in Figure 6, and closely matches previously published systems [7, 8]. The system is similar to a traditional fiber based Michelson interferometer and it consists of a double quantum well structure super luminescent diode (SLD, HP371) source with a center wavelength $\lambda_0 = 841\text{nm}$ and FWHM bandwidth $\Delta\lambda = 49\text{nm}$. The low coherence light propagates through an optical isolator and 50/50 fused fiber coupler. Polarization controllers are installed on both arms to adjust the polarization state of the light to maximum the interference signal. Water cell or two BK-7 prisms are placed in the reference arm to compensate the dispersion in the retina mainly caused by aqueous part. There is a neutral density filter in the reference arm to make sure that the OCT imaging system is shot noise limited. In the sample arm, light from an aspheric fiber collimator is directed on to two mirrors attached to scanning galvanometers mounted on a conventional slit-lamp optical head, to allow for simultaneous OCT and direct viewing of the fundus. Computer performed the scanning control of the lateral and vertical dimensions of the OCT beam. The light power with a maximum of $700 \mu\text{W}$ is projected on the retina via a 60Ø Volk lens and the imaging optics of the eye. Light scattering back from the reference and sample arms is

cross correlated in a 50/50 fiber coupler and passed through a custom-built spectrometer. Collimated light is diffracted by a 1200l/mm transmission grating with the incident angle close to Blaze angle, and focused on the focal place of a linear scan CCD target by an air-spaced achromatic lens pair. A high-speed, 2048 pixel line scan CCD camera (14 μm square pixels) serves as the detector. The theoretical axial resolution is 5.4 μm in retinal and 7.5 μm in air. The lateral resolution is around 25 μm (Zemax simulation) which is also depended on the corneal power and crystalline lens of the retina.

High speed real time acquiring and processing software is written from scratch using Microsoft Visual C++. Multi-thread programming is employed to boost the computing performance. Fastest Fourier transform is implemented using Intel Math Kernel library which is much faster than FPGA or DSP based implementation in 2004. One A-scan has 512 depth pixels (axial). A scanning galvanometer pair is used to form a raster scanning B-scan (512-*1000 lines).For volumetric reconstruction, 100 blocks of B-scan frames are acquired. OCT fundus image is generated from maximum intensity axial projection of the volumetric datasets.

2.1.3 Dispersion Issue in Retina

SDOCT employs a broad band light sources to create coherence gating based

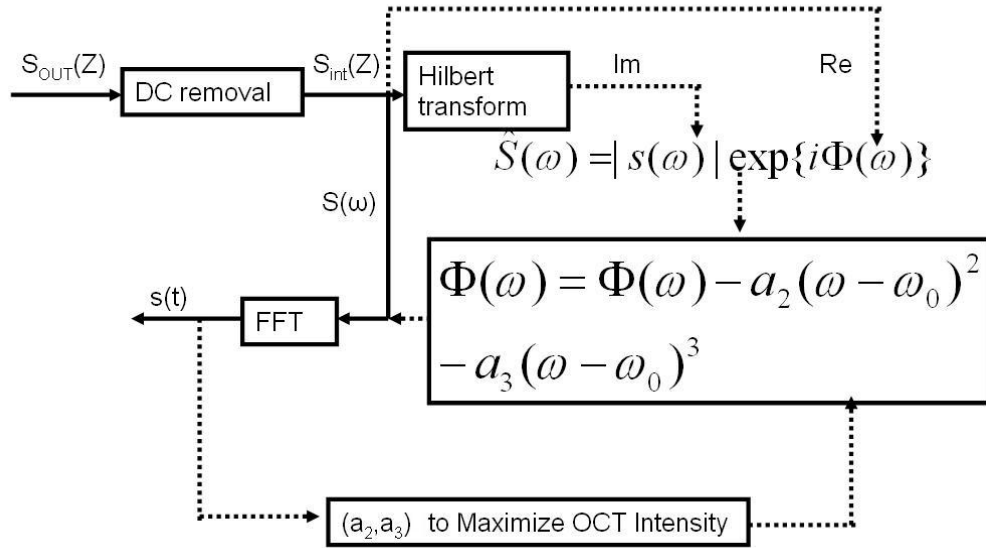


Figure 7: The procedure for dispersion compensation

The dispersion compensation procedure was first proposed by MIT group. The interferogram of SDOCT signal is converted into analytical form using Hilbert transform. Then the phase component is modified by adding two dispersion terms. The highest image contrast is obtained by iteratively changing the dispersion coefficients.

tomography imaging. However, different wavelengths have different propagating speed in tissue such as retina. If we assume all the scattering reflection ratios are unit and ignore the polarization induced dispersion, the detector received signals can be described as

$$D(\omega) = S(\omega) \left| \sum_{J=1}^n E_S \exp(i\beta(\omega)Z_J^S + \varphi_J(\omega)) + E_R \exp(i\beta(\omega)Z^R) \right|^2 \quad (1)$$

Where $S(\omega)$ is the spectrum shape; E_S is the electric field intensity incident on the sample; $\beta(\omega)$ is the propagating constant; Z_J^S is the Jth sample scattering depth

position; $\varphi_j(\omega)$ is the induced fractional phase in the J th layer; E_R is electric field intensity of the reference arm and Z^R is the fixed reference arm position which is also named DC position. By dropping the DC and autocorrelation items, the pure interferometric components useful for OCT imaging are

$$I(\omega) = 2S(\omega) \operatorname{Re}\left\{\sum_{J=1}^n E_S E_R \exp(i\beta(\omega)(Z_J^S - Z^R) + \varphi_J(\omega))\right\} \quad (2a)$$

$$I(\omega) = 2S(\omega) \sum_{J=1}^n E_S E_R \cos(\beta(\omega)\Delta Z_J + \varphi_J(\omega)) \quad (2b)$$

Since the central frequency ω_0 is much larger than the spectral width $\Delta\omega$ of the SLD source, the propagating constant $\beta(\omega)$ can be expanded in a Taylor series[8] around the central frequency ω_0

$$\beta(\omega) = \beta(\omega_0) + (\omega - \omega_0) \left. \frac{\partial\beta}{\partial\omega} \right|_{\omega_0} + \frac{1}{2} (\omega - \omega_0)^2 \left. \frac{\partial^2\beta}{\partial\omega^2} \right|_{\omega_0} + \frac{1}{6} (\omega - \omega_0)^3 \left. \frac{\partial^3\beta}{\partial\omega^3} \right|_{\omega_0} + K \quad (3)$$

The first term introduces a constant phase shift over all frequencies[8, 54] and can be ignored. The second term which is the inverse group velocity indicates the linear phase shift with frequency, leading to no internal change to the light pulse. The third term is the generally dominant dispersion term which broadens the OCT signal. The fourth term will produce asymmetric point spread function in OCT imaging. The last two terms play key roles in the dispersion compensation. In our retinal imaging, we mainly deal with those two terms. MIT group proposed a software based dispersion

compensation methods which is illustrated as in figure 6. As an extension, I have first derived the dispersion coefficients characteristics in the complex conjugated case.

2.1.4 Dispersion Issue in Complex Conjugate Case in Retina

In the retinal imaging, cornea, aqueous, lens, vitreous and retina will mainly induce the material dispersions. The dominant dispersion part comes from vitreous. So if we put the DC position behind vitreous, the material dispersion will be approximated to be independent of the axial position $Z_J^S - Z^R$. According to MIT group, the dispersion compensation can be done by adding a frequency dependent phase term to the OCT signal $\bar{\psi}(\omega)$,

$$I'(\omega) = 2S(\omega) \operatorname{Re}\left\{\sum_{J=1}^n E_S E_R \exp(i\beta(\omega)[(Z_J^S - Z^R) + \varphi_J(\omega) + \bar{\psi}(\omega)]}\right\} \quad (4a)$$

$$\bar{\psi}(\omega) = a_1(\omega - \omega_0)^2 + a_2(\omega - \omega_0)^3 + a_3(\omega - \omega_0)^4 + \Lambda \quad (4b)$$

Where a_1, a_2, a_3 are called the dispersion coefficients. For the complex conjugate case where the imaging retina flips the side around DC, people generally used the same dispersion coefficients for both sides. As a result, the image is clear on one side of the DC but worse on the opposite side of the DC. There is no research result to give a clear explanation for this phenomenon. Currently, researchers have to recalculate the above dispersion coefficients a'_1, a'_2, a'_3 again.

$$I'(\omega)_{Conjugated} = 2S(\omega) \text{Re}\left\{\sum_{J=1}^n E_S E_R \exp(i\beta(\omega)[(Z_J^S - Z^R) + \varphi_J(\omega) + \overline{\psi'}(\omega)]\right\} \quad (5a)$$

$$\overline{\psi'}(\omega) = a_1'(\omega - \omega_0)^2 + a_2'(\omega - \omega_0)^3 + a_3'(\omega - \omega_0)^4 + \Lambda \quad (5b)$$

However the relationship between a_1, a_2, a_3 and a_1', a_2', a_3' is unclear. There is no publication which has derived a useful result regarding the above relationship. This relationship is very useful in OCT imaging to extend the imaging depth and improve image quality.

I have first derived the relationship of dispersion compensation coefficients in the complex conjugated case in 2006. The principle to predict the relationship between a_1, a_2, a_3 and a_1', a_2', a_3' , is based on the property of Fourier transform,

$$FT\{f(z)\} = F(\omega) = |F(\omega)| \exp(\angle F(\omega)) \quad FT\{\} \Rightarrow \text{Fourier Transform} \quad (6a)$$

$$FT\{f(-z)\} = F(-\omega) = F(\omega)^* = |F(\omega)| \exp(-\angle F(\omega)) \quad (6b)$$

Again * means complex conjugate and $\angle F(\omega)$ is the phase of $F(\omega)$. In the complex conjugated case, the sign of the phase is reversed. So the phase term in above equation will become,

$$phase = -\beta(\omega)[(Z_J^S - Z^R) + \varphi_J(\omega) + \overline{\psi'}(\omega)] \quad \text{Clearly} \Rightarrow -\overline{\psi'}(\omega) = \overline{\psi'}(\omega) \quad (7)$$

Accordingly

$$a_1 = -a_1' \quad a_2 = -a_2' \quad a_3 = -a_3' \quad \Lambda \quad a_j = -a_j' \quad (8)$$

The results indicate that the dispersion coefficients have different values when crossing the DC. However, those values are just different in signs and their absolute values are exactly same. Above relationship clearly shows that we cannot use the same dispersion compensation coefficients on the complex conjugated case. Otherwise it is correct for one side; however it is double worse for the conjugated side, which is showed in the below equation:

$$\overline{\psi}(\omega) - \overline{\psi'}(\omega) = 2a_1(\omega - \omega_0)^2 + 2a_2(\omega - \omega_0)^3 + 2a_3(\omega - \omega_0)^4 + \Lambda \quad (9)$$

To evaluate the actual dispersion degree, the a_1 dispersion will introduce the time-spreading, $\Delta\tau$, of a the OCT pulse through

$$\Delta\tau = \frac{2\pi c * 2a_1}{\lambda^2} L\Delta\lambda \quad (10)$$

The result uses the definition of group velocity dispersion $D = -\frac{2\pi c}{\lambda^2} \frac{\partial^2 \beta}{\partial \omega^2}$.

Where c is the speed of light, λ is the central wavelength and L is the thickness of vitreous. Kenny Tao has used this dispersion result for his complex conjugated research to boost his image quality in the complex conjugate case. The following image demonstrates the improved image quality using above dispersion compensation methods in the complex conjugated case[34].

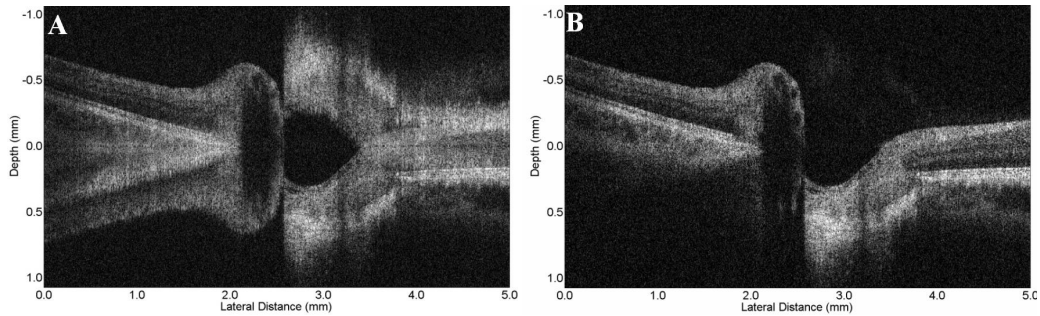


Figure 8: Complex conjugation

A: Conjugated and corrupted ONH. B: Resolved ONH. *in vivo* optic nerve head images with 1024 pixels and 3000 lines/frame resolved using four integrating bucket steps 4.3 images/s. In the complex conjugate resolved images, note that the maximal image brightness occurs at the axial center of the image (i.e., at DC), the doubled image depth, and the additional image depth required for nerve head imaging.

2.1.5 Results

In 2004, the first prototype of SDOCT was built for *in-vivo* imaging of the 3D structure of human retina. This system is the fastest *in vivo* real-time SDOCT in the world at that time. The system can real time process and display 16-kHz a-scan per second which make it successful to clinical ocular imaging. The kernel code and algorithm of this system were transferred to University of California, Davis, and Case Western Reserve University and Indiana University. Prototypes are used by Medical Center of University of South California and Duke Eye Center for clinical diagnostic applications. Figur8 shows the system's sensitivity[27].

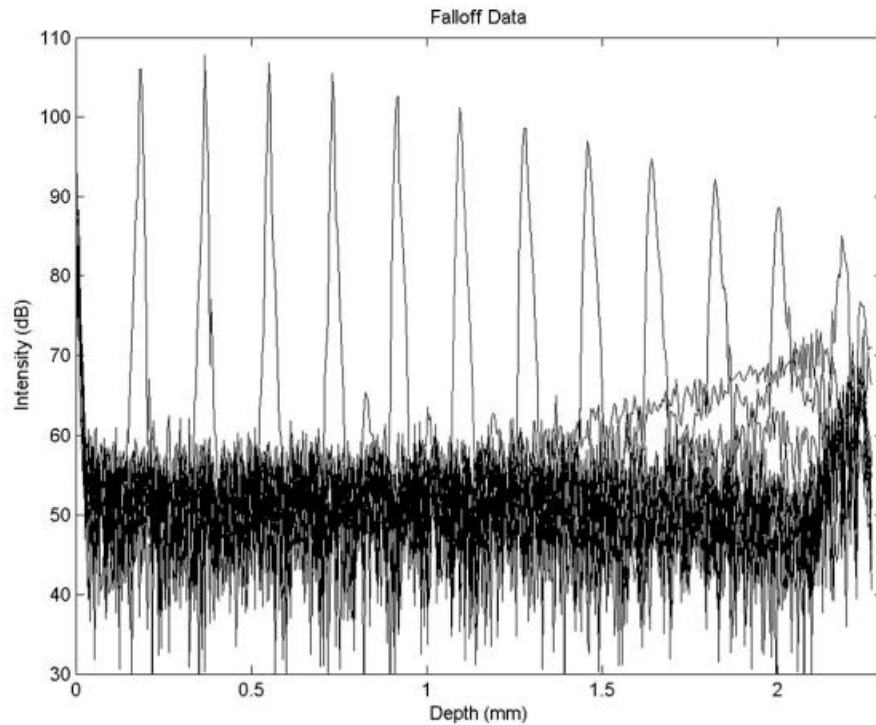


Figure 9: Measured SDOCT system sensitivity as a function of depth

The theoretical system sensitivity at zero path length difference is 110 dB for an integration time of 100 μ s. Depth-dependent sensitivity falloff is dependent on detector pixel size and is complicated by dispersion mismatch between the reference and sample arms. Spectral rescaling was used to correct for dispersion mismatch, yielding a depth-dependent sensitivity falloff of about 15 dB over the entire imaging depth. The 3-dB falloff point is theoretically 1.3 mm and was experimentally measured to occur at 1.0 mm.

The following figures show some of the *in vivo* imaging results obtained by the prototype in 2004. The subject was nondilated with no external immobilization.

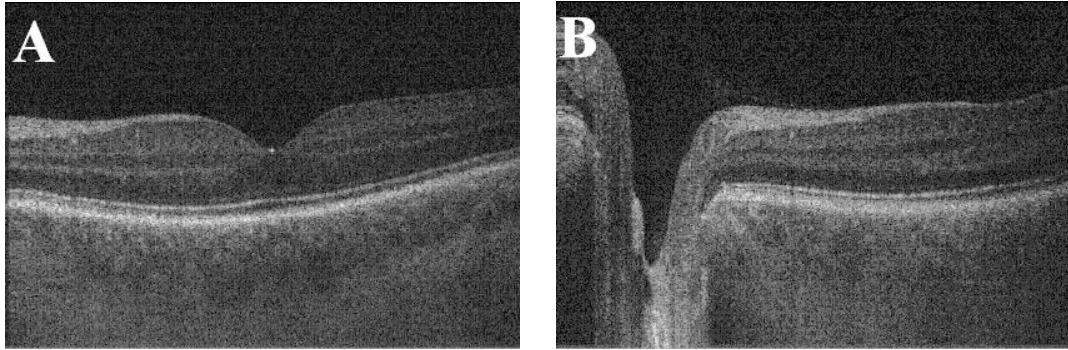


Figure 10: Typical retinal SDOCT imaging results

Image consisting of 512x1000 pixels (axial x lateral) acquired in 62.5ms/image at the following locations. A: Transecting fovea central area. Note clear delineation in all images of the photoreceptor inner/outer segment junction, and the presence of blood vessels (including choroidal vessels). B: Along papillomacular axis.

In summary, I have demonstrated a low-cost, high resolution, real-time Spectral Domain Optical Coherence Tomography (SDOCT) system prototype optimized for rapid 3D imaging of the human retina in vivo. A source with an 841nm center wavelength and a FWHM bandwidth of 49nm are employed for the spectrometer based OCT imaging system, which can acquire images with an integration time of 50 μ s/line, and allows for real time processing and displaying at a frame rate of 16 frames/sec. Three-dimensional data sets comprising up to 4.0mm x 1.2mm x 2.45mm retinal volumes were streamed to hard disk during this brief ocular fixation interval and post-processed to create 3D volumetric images of the optic nerve head and fovea.

2.2 Extension of OCT Using Phase Sensitive Methods

Generally OCT is used to reconstruct the internal reflectivity of sample using the scattering intensity which is only related to the electric field amplitude. There is another item called phase of the electric field which is also very useful. The phase encodes the sample refractive index, tissue or liquid flow dynamics and even the polarization states. Here after we will address the phase sensitive technology in the functional Doppler imaging and a novel widely applicable phase unwrapping method.

2.2.1 Retinal Doppler Imaging

The OCT signal is rewritten as followings to address the phase term $\varphi_J(\omega)$

$$I(\omega) = 2S(\omega) \sum_{J=1}^n E_S E_R \cos(\beta(\omega)\Delta Z_J + \varphi_J(\omega)) \quad (11)$$

If we compare the phase differences of sequential A-scans at the same point $\Delta\varphi_J(\omega)$, the sample flow velocity can be retrieved by $\Delta\varphi_J(\omega)/\tau$. τ is the A-scan integration time.

University of California at Irvine (UCI) group invented an algorithm to calculate the flow velocity, $v(z)$, based on phase changing[55, 56].

$$v(z) = \frac{\lambda}{4\pi\tau \cos(\alpha)} \text{Tan}^{-1} \left[\frac{\text{Im} \left[\sum_{j=1}^n \overline{I_j(\omega)} I_{j+1}(\omega)^* \right]}{\text{Re} \left[\sum_{j=1}^n \overline{I_j(\omega)} I_{j+1}(\omega)^* \right]} \right] \quad (12)$$

Where $\overline{I_j(\omega)}$ is the Hilbert Transform of $I(\omega)$, * means complex conjugate, α is the angle between the flow direction and incident light. I have employed above algorithm

for retinal Doppler imaging. The following figure shows the Doppler flow in the blood vessel in the retina.

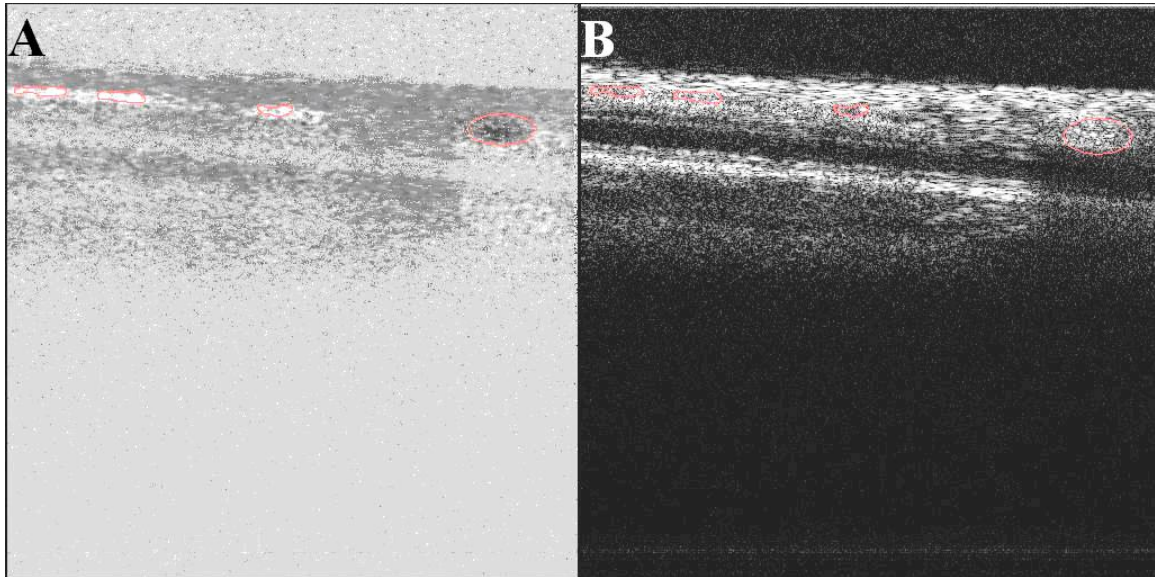


Figure 11: Doppler imaging results

Doppler imaging SDOCT with B-scan comprising 512 (axial) \times 2000 (lateral, A-scan) pixels. Scan location is nasal and superior to optic disk. *In vivo* 512 \times 2000 Doppler frequency images of 2.2 mm (axial) \times 2 mm (lateral) were acquired and processed at video rate 7 frames per sec with single pass. Since the scanning density is very high within a very limited area, the Doppler image is obtained by 4 lines acquired at approximately adjacent lateral position. A: Doppler image. There is a very long vessel cross section (artery) in the left part and a short vessel cross section (vein) on the right part. Those two vessels have different flow direction. B: The intensity image. The vessel positions are overlaid with the intensity image. The red circles indicate the vessel locations.

Particularly I have proposed and implemented a phase algorithm to remove the retinal bulk motion and automatically vessel segmentation.

2.2.2 Methods and Results to Remove Doppler Bulk Motion

One common problem for Doppler imaging is bulk motion. The integration time of Doppler imaging is typically 50 micro second during which patient will have a slight

bulk motion. This will influence the measurement accuracy of the blood velocity. To remove the bulk motion, the phase shifting on the top layer of the sample tissue are calculated; then each phase of the whole A-scan line is compensated by this value. Real time Doppler processing software is developed from scratch using Visual C++. The software can process and real time display 4-kHz A-scans, which is 8-frames B-scan (512 lines) per second.

The detected OCT intensity combining the phase changing between adjacent A-scans is expressed as following,

$$\tilde{I}(\pm 2n\Delta z) = (\rho/2e)S\tau\sqrt{R_R R_S} E(2n\Delta z + 2n\delta z') \exp[i\Delta\Phi_{Flow} + i\Delta\Phi_{Bulk_Motion}] \quad (13a)$$

$$OCT_Intensity = (\rho/2e)S\tau\sqrt{R_R R_S} E(2n\Delta z + 2n\delta z') \quad (13b)$$

$$\Delta\Phi_{Flow} = 2k_0 n \delta z_{Flow} \quad (13c)$$

$$\Delta\Phi_{Bulk_Motion} = 2k_0 n \delta z_{Bulk_Motion} \quad (13d)$$

Where ρ is the detector responsibility; e is the electric charge, R_R and R_S are the reference and scattering tissue reflectivities; S is the total source power, $E(2n\Delta z + 2n\delta z')$ is the unity-amplitude coherence envelope function; the phase change induced by the vessel flow is $\Delta\Phi_{Flow}$ and it is $\Delta\Phi_{Bulk_Motion}$ caused by the bulk motion. Then the Doppler velocity equation will be modified as

$$v(z) = \frac{\lambda}{4\pi\tau \cos(\alpha)} \tan^{-1} \left[\frac{\text{Im} \left[\sum_{j=1}^n \overline{I_j(\omega)} I_{j+1}(\omega)^* \right]}{\text{Re} \left[\sum_{j=1}^n \overline{I_j(\omega)} I_{j+1}(\omega)^* \right] - \tan[\Delta\Phi_{Bulk_Motion}]} \right] \quad (14a)$$

$$\text{Im}\left[\sum_{j=1}^n \overline{I_j(\omega)I_{j+1}(\omega)^*}\right] / \text{Re}\left[\sum_{j=1}^n \overline{I_j(\omega)I_{j+1}(\omega)^*}\right] = \text{Tan}[\Delta\Phi_{Flow} + \Delta\Phi_{Bulk_Motion}] \quad (14b)$$

We calculate the first layer Doppler phase shift which is $\Delta\Phi_{Bulk_Motion}$; then we can subtract $\Delta\Phi_{Bulk_Motion}$ from the each phase of all the depth pixels. Finally all the bulk motions are removed from the reference top layer. After removing the phase contribution induced by the bulk motion, we have to do the phase unwrapping to obtain correct flow velocity. For example, if the bulk motion direction is opposite of the vessel flow direction, phase wrapping could happen after bulk motion removal. To avoid the phase wrapping, the maximum theoretical retina blood flow including bulk motion is 4.245 mm/s. The result is based on below parameters,

$$v(z) = \frac{\lambda}{4\pi\tau \cos(\alpha)} \Delta\Phi_{\max}, \Delta\Phi_{\max} = \pi, \tau = 50\mu s, \cos(\alpha) = 1, \lambda = 849\text{nm}. \quad (15)$$

The following figure shows the Doppler bulk motion results. The left side is Doppler image and right side is OCT intensity image. The vessel is automatically segmented and highlighted by a red circle. The Doppler image shows a black background which is introduced by bulk motion.

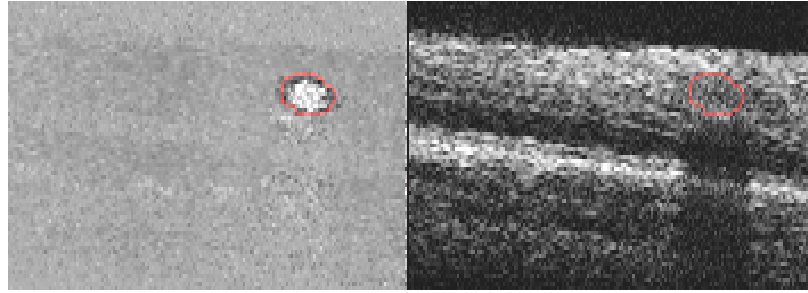


Figure 12: Doppler bulk motion removal
The left part is the Doppler image with bulk motion and the right is the OCT image

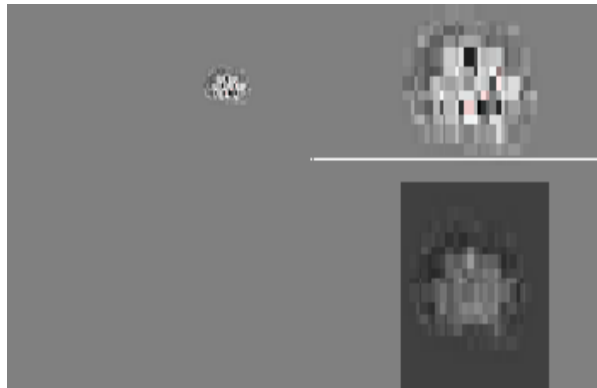


Figure 13: Doppler image after bulk motion removal
The top right is the zoom in of the left image which is phase wrapped; and bottom right is the phase unwrapping result.

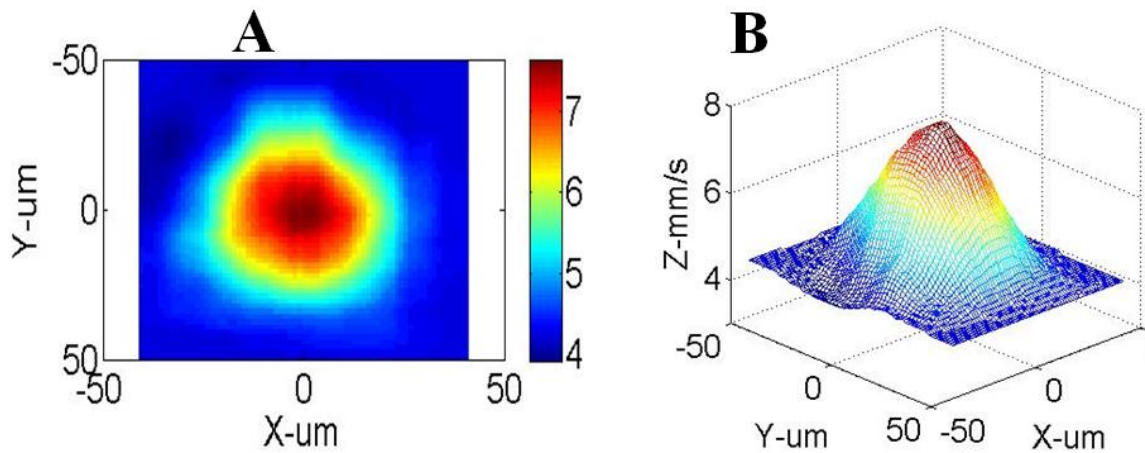


Figure 14: Doppler flow image

A: Phase unwrapping Doppler flow display in 2D after denoising. B: 3D display of Doppler unwrapping. The peak velocity is clearly higher than the phase wrapping limit (4.25mm/s).The unit is mm/s

All the bulk motion removal and vessel segmentation are implemented automatically using Visual C++. Its processing procedure is describe as below,

- Obtain the Doppler and OCT image from spectrometer raw data
- Use Sobel operator to sharpen the Doppler image
- Employ median filtering to remove small block noise
- Apply image dilation and image erosion to remove fake vessel
- Perform image edge detection to get the vessel area
- Utilize the top layer to retrieve phase of bulk motion and remove this additional phase from each A-scan of Doppler image
- Do phase unwrapping and overlay the vessel boundary with OCT image

We have also theoretically explored the Doppler sensitivity assuming the SNR is shot noise limited.

$$A(\pm 2n\Delta z) = ((\rho/e)S\tau R_R)^{1/2} \exp(-i\Phi_{noise}) \quad (16)$$

$A(\pm 2n\Delta z)$ is the component caused by shot noise; and Φ_{noise} is the rand phase of the shot noise. So shot noise introduces a Doppler fluctuation,

$$\Delta\Phi_{Doppler} = \tan^{-1}(\Phi_2 - \Phi_1) = \tan^{-1}(\overline{\Phi}_2 + \Phi_{2_noise} - \overline{\Phi}_1 - \Phi_{1_noise}) \quad (17a)$$

$$\Delta\Phi_{Doppler} \approx \overline{\Phi}_2 + \Phi_{2_noise} - \overline{\Phi}_1 - \Phi_{1_noise} \quad (17b)$$

Where Φ_i is the measured phase; $\overline{\Phi}_i$ is the original sample phase without noise; Φ_{i_noise} is the phase generated by shot noise. If we only use two adjacent A-scans to compute the Doppler, then

$$\sigma^2(\Delta\Phi_{Doppler}) = \sum_{i=1}^2 \sigma_{i_noise}^2 = 2\sigma_{Doppler_Phase_Sensitivity}^2 \quad (18)$$

Since

$$\sigma_{Doppler_Phase_Sensitivity} = \tan^{-1}\left[\left|\frac{A(\pm 2n\Delta x)}{I_i(\pm 2n\Delta x)}\right|\right] = \left(\frac{2e}{\rho S \tau R_s}\right)^{1/2} \quad (19a)$$

$$\sigma_{Doppler_Phase_Sensitivity} \approx \left(\frac{2e}{\rho S \tau R_s}\right)^{1/2} = \left[\frac{1}{SNR(S, \tau, R_s)}\right]^{1/2} \quad (19b)$$

We obtain

$$\sigma(\Delta\Phi_{Doppler}) = \sqrt{2}\sigma_{Doppler_Phase_Sensitivity} \quad (20a)$$

$$f_{Doppler_Deviation} = \frac{\sigma(\Delta\Phi_{Doppler})}{2\pi\tau} = \frac{1}{\sqrt{2 \cdot SNR} \pi\tau} \quad (20b)$$

2.2.3 Methods and Results of Phase Unwrapping Using Synthetic Wavelength

OCT phase imaging can be used for measuring the object height, optical coherence elastography or cell vibration with accuracy in the order of angstroms. However there is a phase wrapping issue if the target motion is faster than half wavelength within the A-scan integration time. In this session, one synthetic partial coherent wavelength is obtained via changing the coherent length of a partial coherence source. I have first publicly presented this idea[32, 57] in April 2006 under the instruction of Dr. David J. Brady, who is the founding director of Fitzpatrick Institute for Photonics, and Dr. Joseph A. Izatt. A synthetic wavelength 17.32um, which is much longer than original central wavelength 840nm, can be obtained to solve the phase wrapping problem. Synthetic wavelength phase unwrapping can be used in Doppler imaging, 3D profile measurement and optical coherence elastography. Phase based optical coherence elastography which I have developed in 2005 is illustrated as follow,

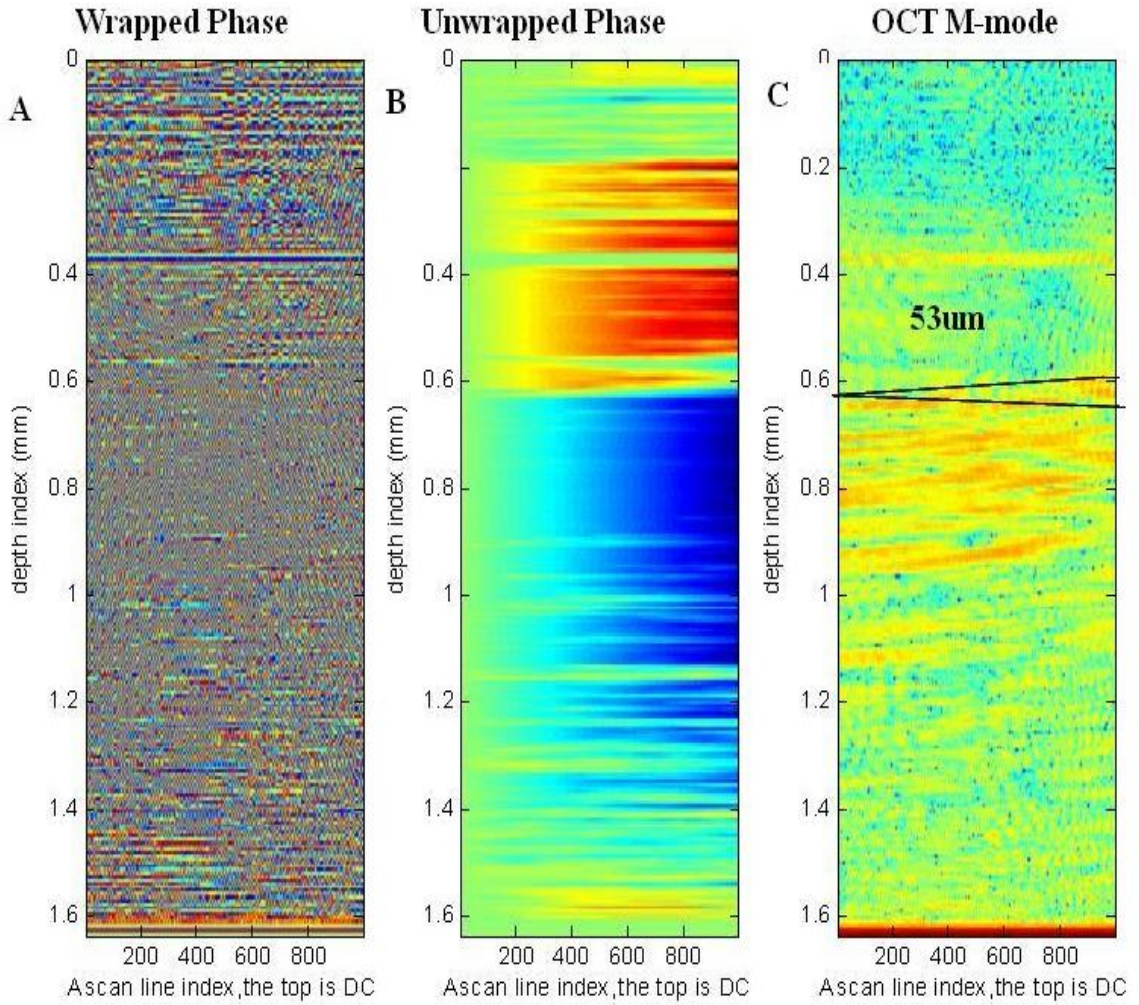


Figure 15: OCT elastography

A: Wrapped phase map image of pressed sample. B: Phase unwrapping of the overall phase of 1000 lines, which indicates the gradually increase phases. The overall spatial shift is 53.79 μm based on phase calculation. C: OCT image correlation shows the sample movement is around 53 μm which agree very well with the unwrapped phase image.

To solve phase unwrapping, we traditionally just change the phase based on prior knowledge, which is illustrated in the following equation and figure.

$$\Phi_{NEW} = \Phi \pm 2\pi \quad (21)$$

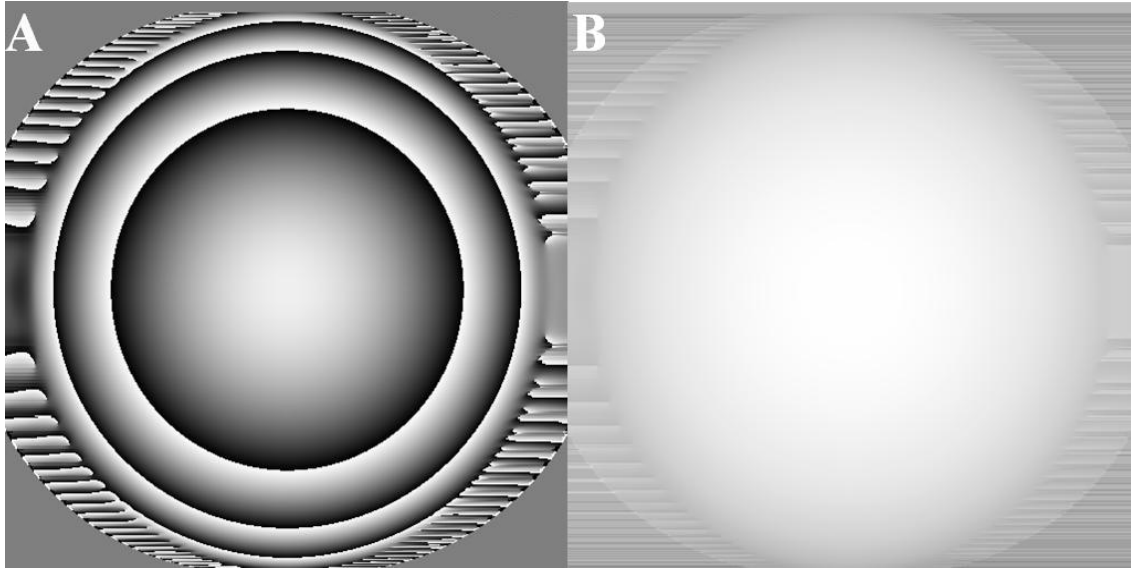


Figure 16: Traditional phase unwrapping

A: Wrapped phase. B: Unwrapped phase.

In OCT elastography, Doppler flow velocity analysis and cell imaging, there is no prior information available. The phase wrapping can happen in any position and the wrapping amount can be even more than 10π . I have proposed a relative general solution in OCT community to resolve the wrapped phase using a synthetic wavelength. Its principle is based on the following equation.

$$\tilde{I}(\pm 2n\Delta z) = (\rho / 2e) S \tau \sqrt{R_R R_S} E(2n\Delta z) \exp(\pm j 2k_0 n \delta z) \quad (22)$$

As the above equation indicates, the measurement range is only within half wavelength, otherwise phase wrapping happens which causes the ambiguity of the measurement. However, if the wavelength is very long, there will be no phase wrapping issue. Here two-synthesized-partial-coherent-wavelength method is proposed to create a

long wavelength. This idea is triggered by the research of two-wavelength phase shifting interferometry[58]. Yeou-Yen at Dr.Wyant's group employed 4 separate laser wavelengths to solve the phase wrapping problem. They used 2 different laser sources to generate a beating longer wavelength to extend the phase measurement range. However, there are disadvantages for above two-source solution.

- Two sources have to pass same optical path to focus on the same areas, which is relatively hard to alignment. Also the costs are higher.
- Different sources have different noise spectrums, which introduce big measurement errors.

To get rid of multiple laser sources, a new implementation is provided and it is very straightforward and independent of boundary condition. The principle is that two different central wavelengths are obtained via changing the coherent length of a 40nm bandwidth partial coherent source. To change the coherent length, a spectral shaping technique is used to obtain the two different central wavelengths. The idea is to use two Gaussian shapes at different central wave number to create two pseudo different partial coherent sources. The bandwidths of those two partial coherent sources are chosen to ensure they have exactly same coherence length, but they are in different central wavelengths. Using the synthetic technique, an equivalent wavelength 17um is achieved. The synthesized wavelength can be calculated using equation,

$$\lambda_{eq} = \frac{\lambda_a \lambda_b}{\lambda_a - \lambda_b} \quad (23)$$

Advantages of synthetic wavelength method are:

- Two pseudo sources exactly share the same optical path to focus on the same areas, which are the common OCT alignment procedure. It is cheap and common path which reduces the optical path vibration errors to get better measurement accuracy.
- Two pseudo sources are created from a single source which has the exactly same noise spectrum for both of them. The common source noise will reduce the phase errors. The coherence length l_c

$$l_c = \frac{2 \ln(2) \lambda_0^2}{\pi \Delta \lambda} \quad (24)$$

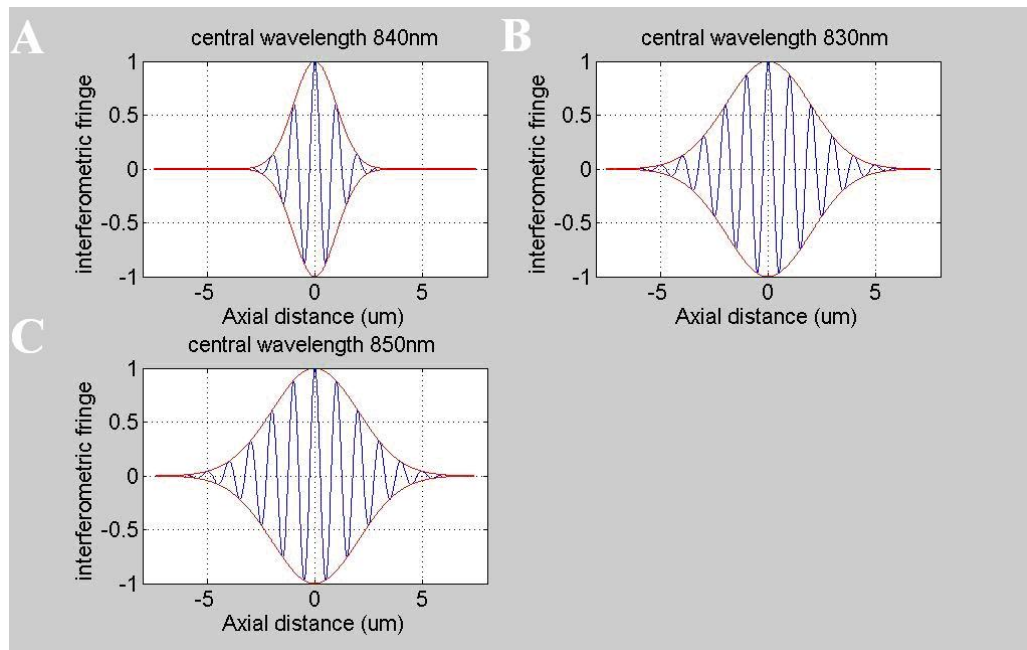


Figure 17: Optical coherent signal at different central wavelengths
A: the interferogram of light source at 840nm with 40nm band width (BW). **B:** the interferogram of light source at 830nm and BW is 20nm. **C:** the interferogram of light source at 850nm and BW is 20nm[57].

Two Gaussian shaping central wavelengths of 830 nm and 850 nm are chosen respectively. The bandwidth is around 20nm for both wavelengths to ensure the same coherent lengths for each shaping spectrum. The original central wavelengths of the source are around 840nm with a bandwidth 40nm. Computer simulated OCT signals are illustrated as following,

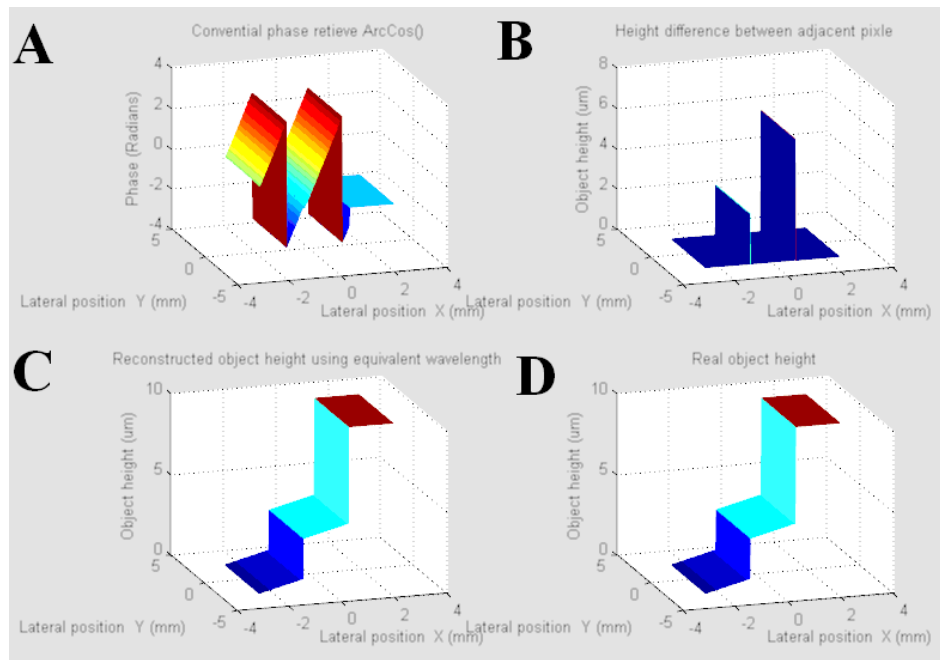


Figure 18: Simulation results of synthetic wavelength for phase unwrapping.
A: The object height (radians) retrieved using conventional ArcCos() method. It is clearly phase-wrapped. The jump step cannot be resolved at lateral location -0.84mm ($2\mu\text{m}$ jump) and 0.84mm ($5\mu\text{m}$ jump) respectively. **B:** The results of synthetic wavelength and dispersion phase differences between two wavelengths (830nm and 850nm), which indicates the step jumps at the sheer edges. **C:** The object height is retrieved using the synthetic wavelength based phase unwrapping. **D:** The real object height. The sheer jumps are successfully obtained[57].

The simulated OCT signal is the cross correlation of the sample field and reference field. Hansford C. Hendargo[33] has successfully used this method for cell microscopy imaging in 2009 in our lab. The results are summarized as following.

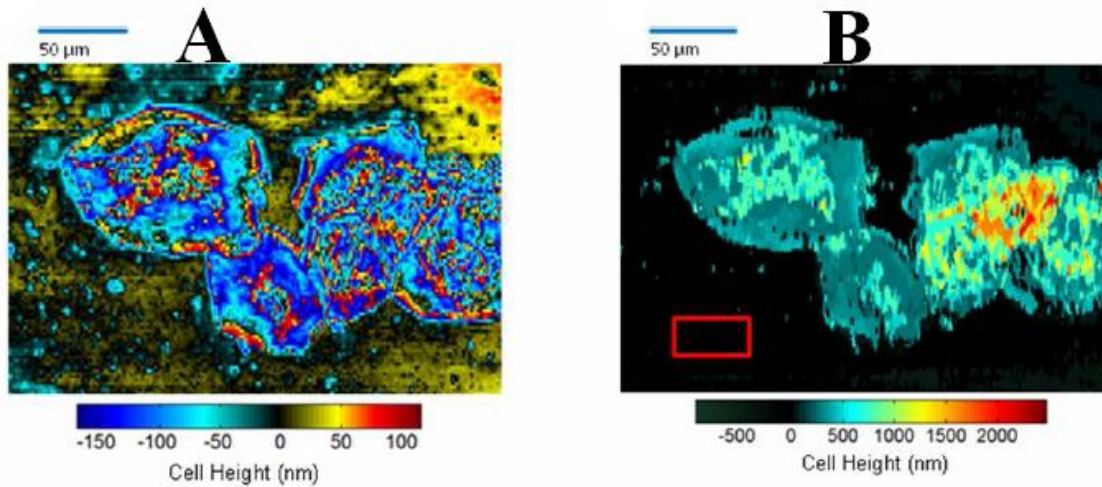


Figure 19: Phase images of human epithelial cheek cells
A: Wrapped phase image. B: Filtered single wavelength phase map corrected using synthetic wavelength unwrapping. Note the difference in the color bar scales for A and B. Region in the red box indicates area used as the reference[33].

We have presented a synthetic wavelength processing method to correct phase unwrapping in cell imaging. Using two Gaussian spectral windows on the detected broadband spectrum to create a longer beating wavelength, it helps us to improve the measurement dynamic range. The phase map obtained from each individual window allows us to find the wrapping points and correct them. Though not developed here, the two window method may potentially be extrapolated for the phase unwrapping in optical coherence elastography, 3D profile measurement and Doppler flow imaging.

2.3 Summary

I have demonstrated real-time 16 kHz line rate imaging of the human retina *in vivo*. This allows for rapid (6.67s) acquisition of 3D volumes which can be reconstructed

offline. Functional imaging, such as Doppler, is extended in retinal imaging. Bulk motion removal method is developed to accurately estimate the flow velocity in the retinal vessel. A theoretical prediction on dispersion compensation in complex conjugate case is provided and it agrees very well with experimental results. Eventually a synthetic wavelength method, which changes the coherence length of scattering spectrum, is invented to solve the phase wrapping issue in OCT phase imaging.

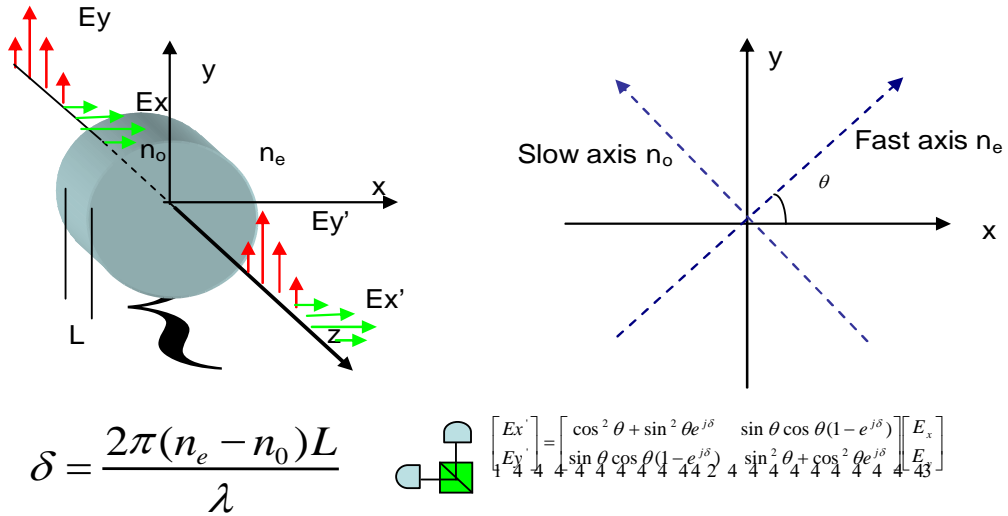
3 Functional Imaging with Polarization Sensitive SDOCT

3.1 Introduction

Spectral domain optical coherence tomography (SDOCT) has recently emerged as a powerful new tool for noninvasive human retinal imaging. SDOCT permits much faster image acquisition rates (up to 30,000 A-scans/sec in commercially available systems) than the conventional time-domain approach. Polarization sensitive OCT (PSOCT) was first proposed in 1992[35] to quantify sample birefringence, then further developed in several groups to measure the birefringence effects of skin[59-62] , cornea, retina and other biological tissues[38-41, 43, 63]. PSOCT provides additional contrast, such as retardance and fast axis orientation, for retinal imaging and has been shown to be sensitive to the orientation and density of the ganglion cell axons, microtubules and fibers in the RNFL and Henle's fiber layer. In addition, PSOCT can be potentially used to aid in the diagnosis of age-related macular degeneration (AMD), which is characterized by the formation of lipoproteinaceous deposits (drusen) between the retinal pigment epithelium (RPE) and underlying structures[45]. For example, recently researchers proposed to segment the RPE using the retardance scrambling properties of RPE[46]. A few preliminary spectral domain PSOCT systems have recently been reported; however they have included multiple expensive spectrometers or difficult alignment using a Wollaston prism inside a single spectrometer. In this paper, we report on a compact,

high-speed polarization sensitive SDOCT (PS-SDOCT) system for retinal imaging which is a simple modification of a state-of-the-art SDOCT system and operates at 17,000 A-scans/sec (50 us integration time). This PS-SDOCT system is able to perform imaging of the birefringent properties of human retina without significant motion artifact. In addition, we introduce the combination of the standard deviation of the fast axis orientation and retardance to extract the RPE layer from retina.

In this project, I mainly employed Jones matrix to model the polarization states in retinal imaging. There are three special Jones matrices[64], which are rotator, retardation plate and partial polarizer. A complicated optical component can be expressed as the product of those fundamental Jones matrices. The following figure shows the principle of polarization sensitive OCT.



Jones Matrix

Figure 20: Illustration of the birefringence effects

The phase differences of two orthogonal electric fields are called the retardance; the orientation angle where the electric field propagates faster is called the fast axis orientation.

3.2 Simulation and Polarization State Selection

The contrast of OCT comes from the scattering field of a medium. According to E.Wolf[65], for a monochromatic wave, the scattering field can expressed as following equation

$$\nabla^2 E(r, \omega) + k^2 E(r, \omega) = -4\pi F(r, \omega) E(r, \omega) \quad (1)$$

Where the symbol

$$F(r, \omega) = \frac{1}{4\pi} k^2 [n^2(r, \omega) - 1] \quad (2)$$

Represent the scattering potential of the scattering medium. Apparently the refractive index $n(r, \omega)$ will determine the amplitude and phase of the scattering field.

Considering the polarization case, $n(r, \omega)$ will become a vector in two dimension case. The scattering potential will vary with the incidental polarization states. Bases on these features, the choice of incident polarization states are very important to get better incited polarization sensitive contrast image.

Considering a collagen fiber with a diameter of 120nm[15, 66] which is the typical value in retina, if a linear polarization state such as TM^z mode is used, its scattering properties can be illustrated in the following figure.

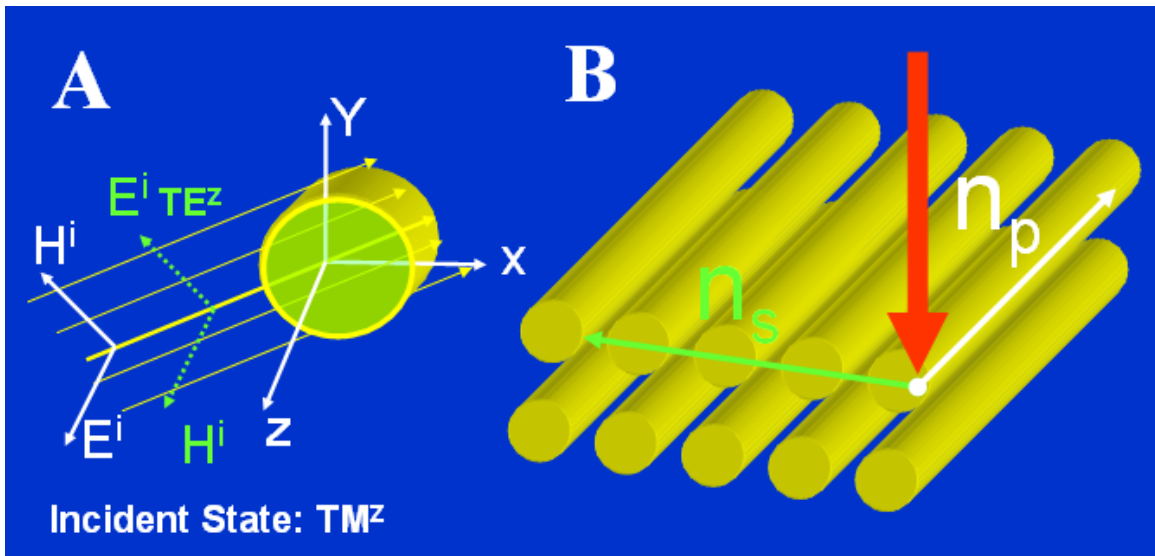


Figure 21: Collagen fiber model and input polarization state scattering simulation
A: The polarization state of white color is TM^z and green one is TE^z mode. **B:** n_s is the refractive index which is perpendicular to the fiber and n_p is the refractive index which is parallel to the fiber.

For the TM^z case, the scattering field when the incident angle is 0, can be represented as following.

Incident field:

$$E^i = \hat{z}E_0 \sum_{n=-\infty}^{+\infty} j^{-n} J_n(\beta_0 \rho) e^{jn\phi} \quad (3)$$

Scattering field out side collagen fiber:

$$E^s = \hat{z}E_0 \sum_{n=-\infty}^{+\infty} a_n H_n^{(2)}(\beta_0 \rho) e^{jn\phi} \quad (4)$$

Scattering field inside collagen fiber

$$E^d = \hat{z}E_0 \sum_{n=-\infty}^{+\infty} (b_n J_n(\beta_1 \rho) + c_n Y_n(\beta_1 \rho)) e^{jn\phi} \quad (5)$$

Using exact radiation boundary condition, we can get

$$a_n = j^{-n} \frac{J_n'(\beta_0 a) J_n(\beta_1 a) - \sqrt{\varepsilon_r / \mu_r} J_n(\beta_0 a) J_n'(\beta_1 a)}{\sqrt{\varepsilon_r / \mu_r} J_n'(\beta_1 a) H_n^{(2)}(\beta_0 a) - J_n(\beta_1 a) H_n^{(2)'}(\beta_0 a)} \quad (6)$$

$$b_n = j^{-n} \frac{J_n(\beta_0 a) H_n^{(2)'}(\beta_0 a) - J_n'(\beta_0 a) H_n^{(2)}(\beta_0 a)}{J_n(\beta_1 a) H_n^{(2)'}(\beta_0 a) - \sqrt{\varepsilon_r / \mu_r} J_n'(\beta_1 a) H_n^{(2)}(\beta_0 a)} \quad (7)$$

$$c_n = 0 \quad (8)$$

The scattering absolute value of electric field and the corresponding phase images are demonstrated by customized program in Matlab™ as followings.

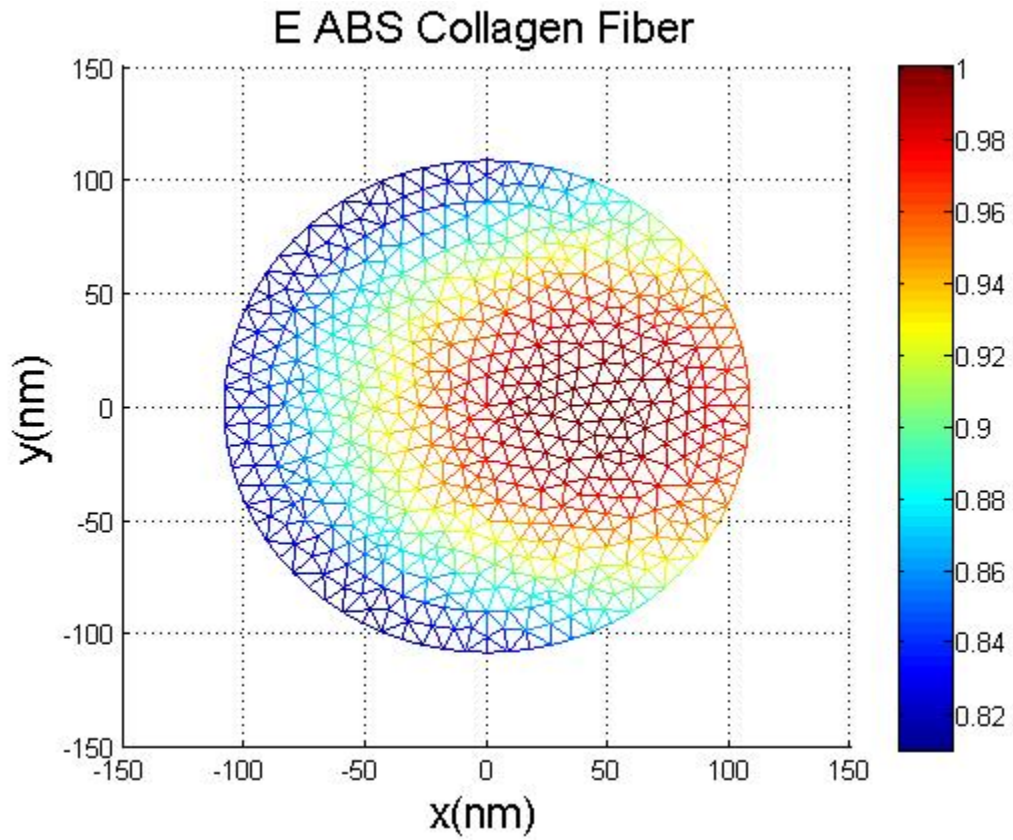


Figure 22: The absolute value of scattering electric field (customized in Matlab)

It indicates that majority of light will continuously propagate and only a frictional part is scattered back. This result agrees very well with customized finite element method simulation.

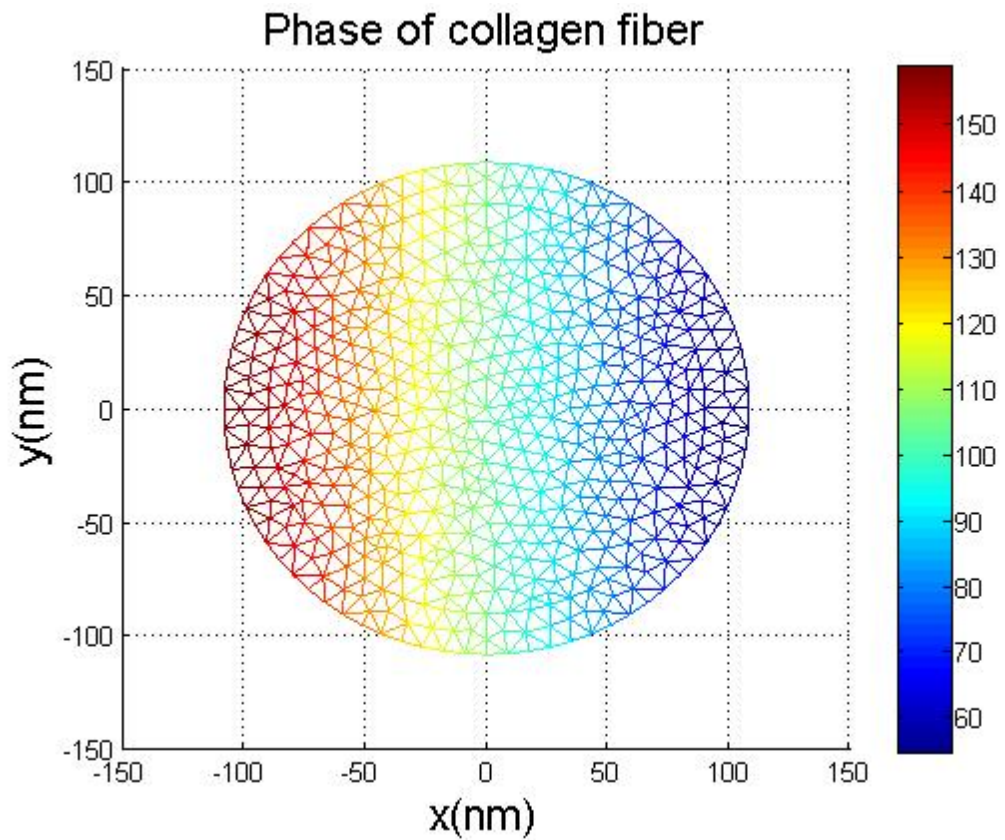


Figure 23: The wavefront of light scattering in a collagen fiber (customized in Matlab)

The phase is close constant in the plane, which is perpendicular to propagating direction. It means our PSOCT system must be sensitive to detect those slightly phase change in the birefringence medium.

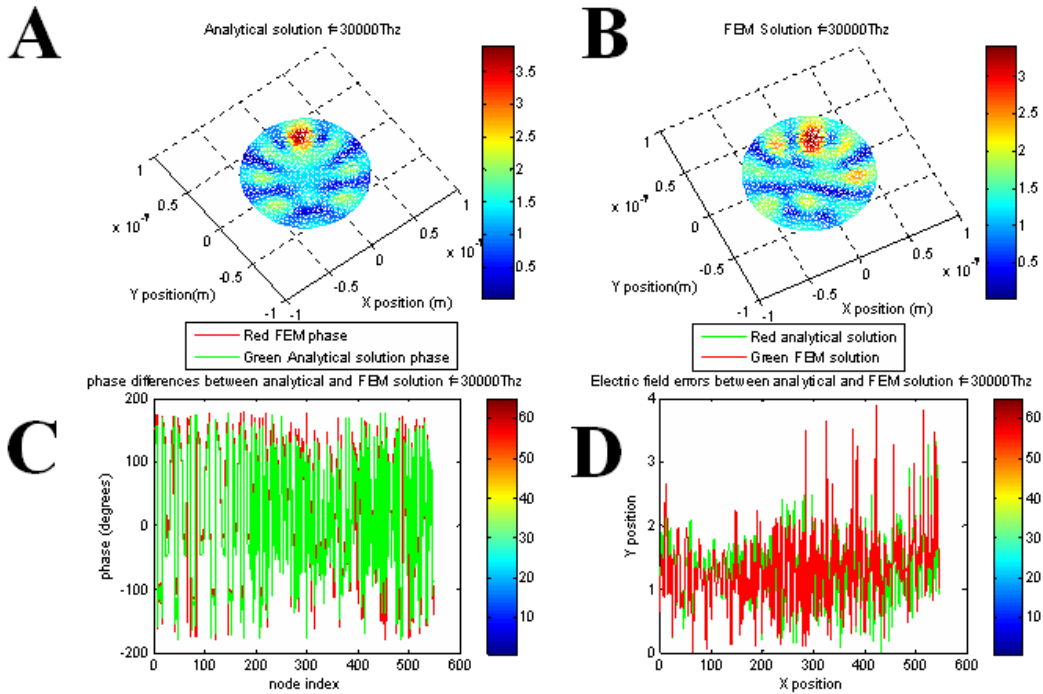


Figure 24: Customized FEM simulation

Customized Finite Element Method (FEM) simulation in Matlab confirms the analytical solution. A: analytical solution. B: FEM simulation (c) phase comparison plot for analytical and FEM simulation (d) amplitude comparison plot for analytical and FEM simulation. Above results shows the analytical solution agrees very well with numerical solution

Above simulation indicates that linear polarization state such as TM^Z case only incite the scattering potential which is parallel to the collagen fiber direction. To effectively detect the birefringence effects, we have to choose a proper polarization state to incite scattering potentials which are both parallel and perpendicular to the collagen fiber. To solve this problem, I have only employed elliptical polarization states as the input polarization states.

3.3 Materials and Methods of Free Space Based PSOCT

Our high-speed retinal PS-SDOCT system is shown in following figure[47].

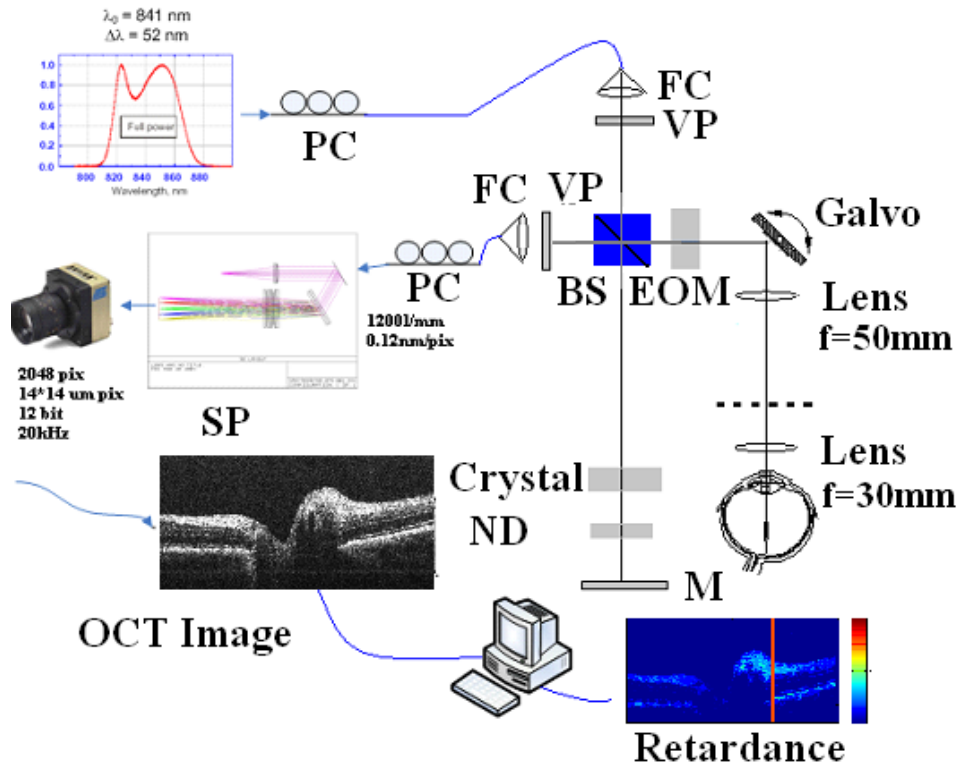


Figure 25: Schematic of the PSOCT system

SP, spectrometer; PC, polarization controller; FC, fiber collimator; VP, vertical polarizer; M, mirror; BS, non-polarization beam splitter.

The system employs a super luminescent diode (SLD) emitting at 840nm (Super SLD-371-HP). The fast axis of an electro-optic modulator (EOM) placed in the sample arm is oriented at 45° from the horizontal. Modified commercial software (Bioptigen, Inc.) was used to collect repeated A-scans from a 2048-pixel line scan camera at a

readout rate of up to 17 kHz. Jones matrices are used to model the tissue birefringent characteristics. The optical power detected from the sample arm is given by[61]

$$P(r) = P_s \left\{ \frac{1}{2} + \frac{1}{2} \cos^2(r) [\cos^2(2\theta) + \sin^2(2\theta) \cos(\delta)] - \cos(r) \sin(r) \sin(2\theta) \sin(\delta) - \frac{1}{2} \sin^2(r) \cos(\delta) \right\} \quad (9)$$

Where P_s is the power incident on the sample arm, r is the retardance of the EOM, δ is the accumulated net sample retardance and θ is the accumulated net sample fast axis orientation. This equation indicates that the signal noise ratio (SNR) for each polarization state is dependent on the tissue birefringence effects. The following figure shows the relationship among normalized OCT intensity, retardance and fast axis orientation.

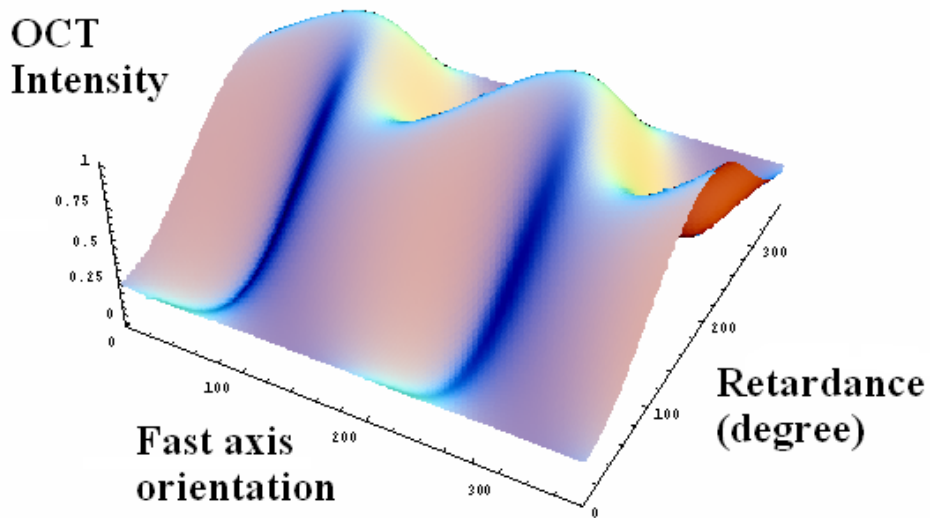


Figure 26: The relationship between normalized OCT intensity and birefringence parameters

Apparently the OCT signal is modulated by the medium retardance and fast axis orientation.

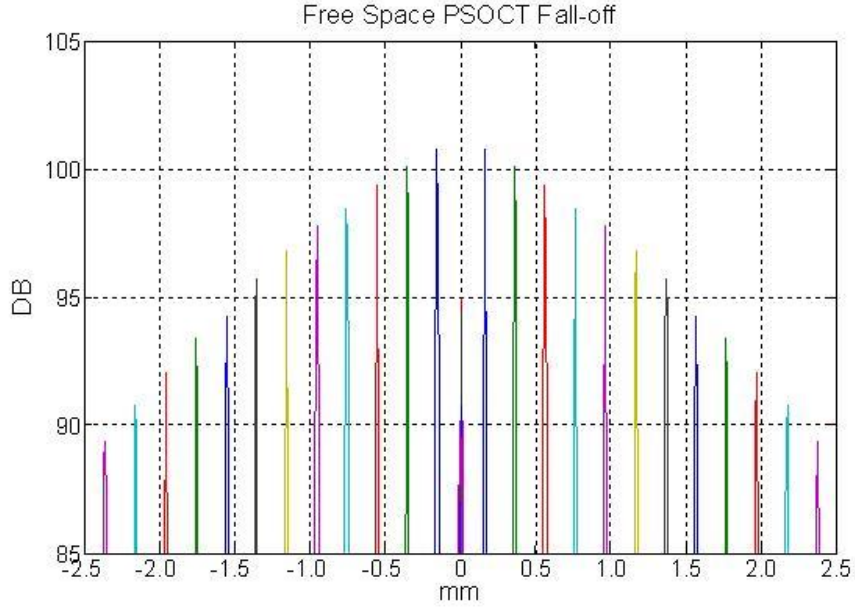


Figure 27: Fall off of the free space based polarization sensitive OCT
A-scan rate: 20 kHz, sensitivity = 102dB, Ps = 0.62mw, Z_{3db} = 1mm, coherent length = 6.3um in air.

The E_y component of the Jones vector of the sample scattering electric field is:

$$E_y = \sin(\delta) \exp(i(\pi - \delta - 2\theta)), \varphi_{y1} = \pi - \delta - 2\theta \quad (10)$$

Here, φ_{y1} is the phase of the E_y component. The fast axis orientation and retardance of the tissue can be retrieved using three input polarization states. Since $P(r) \propto E_y^2$ introduces phase wrapping in equation (2) which limits the encoded fast axis orientation range to 90° , to extend the unambiguous range of optic axis determination from 90° to 180° , one more polarization state of $r = -90^\circ$, is utilized and a unique phase

algorithm is proposed to retrieve the fast axis orientation. The E_y of the sample scattering field when $r = -90^\circ$ is

$$E_y = \sin(\delta) \exp(i(-\delta + 2\theta)), \varphi_{y2} = -\delta + 2\theta \quad (11)$$

where φ_{y2} is the phase of E_y when the setting of EOM $r = -90^\circ$. If ignoring sample motion, the resulting expressions for retardance, fast axis orientation and reflectivity are then:

$$A_{is}^2 = \frac{1}{2}(A_{45}^2 + A_{-45}^2) + \frac{1}{2}[(A_{45}^2 + A_{-45}^2 - 2A_{+90}^2)^2 + (A_{45}^2 - A_{-45}^2)^2]^{1/2} \quad (12)$$

$$\delta = \cos^{-1}(1 - 2A_{+90}^2 / A_{is}^2) \quad (13)$$

$$\theta = \begin{cases} \frac{\pi - (\varphi_{y1} - \varphi_{y2})}{4} & \text{if } A_{-45}^2 > A_{45}^2 \\ \frac{\pi - (\varphi_{y1} - \varphi_{y2})}{4} + \frac{\pi}{2} & \text{if } A_{-45}^2 < A_{45}^2 \end{cases} \quad (14)$$

In the above expressions, A_{is}^2 represents the total reflectivity and $A_{is}^2 = 4\rho^2 P_r P_s$ where ρ is the detector responsivity and P_r is the reference arm power. A_r represents the amplitude of envelope of the interferogram at a given depth measured with EOM retardance of r .

A quarter waveplate was employed to calibrate the performance of the PS-SDOCT system. The new unambiguous range of optic axis orientation is from -90° to 90° , which is twice as large as that described in $(-45^\circ$ to $45^\circ)$ as illustrated in Figure 29(b). The

standard deviation of the retardance measurement (2.3°) is comparable to recently reported PS-SDOCT systems, however the measured standard deviation of the fast axis orientation (0.7°) is much more accurate than for other reported PS-SDOCT systems since the single channel configuration will reduce common mode noises. We further tested the system's depth resolving capability of retardance detection by cascading a Berek variable waveplate with a quarter waveplate.

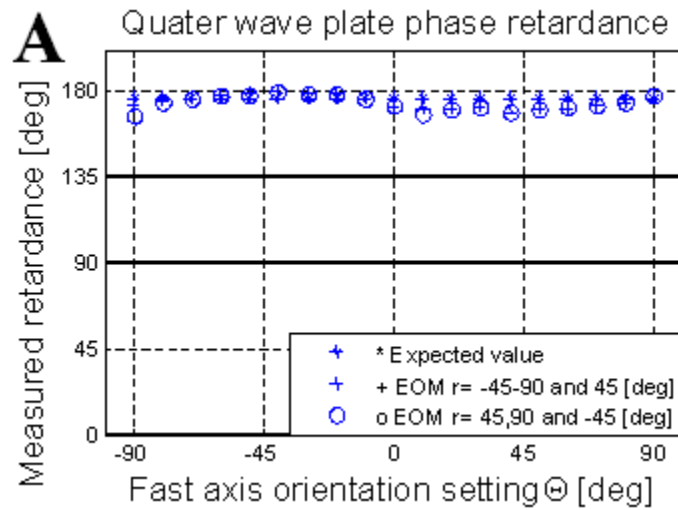


Figure 28: Quarter wave plate calibration

Double pass phase retardance calibration. The mean absolute error was 3.2° and the standard deviation was 2.3°

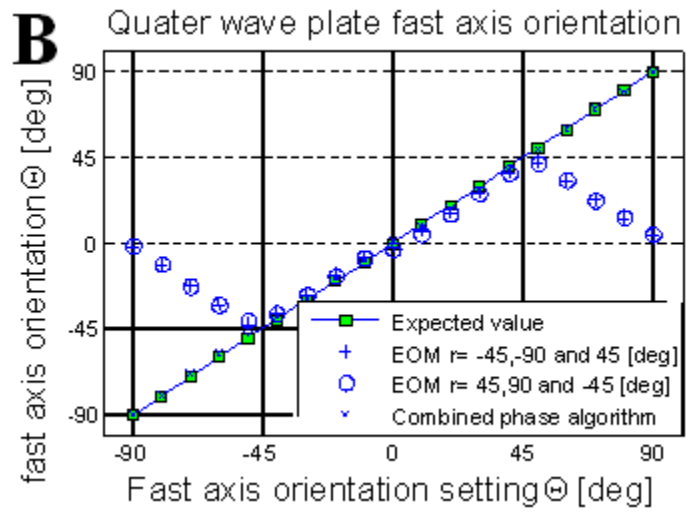


Figure 29: Fast axis orientation calibration of a quarter waveplate
 The mean absolute error was 1.2° and the standard deviation was 0.7° .

The combined retardation measurements were taken when the variable Berek settings were 0° , -24.2° and -57.8° separately.

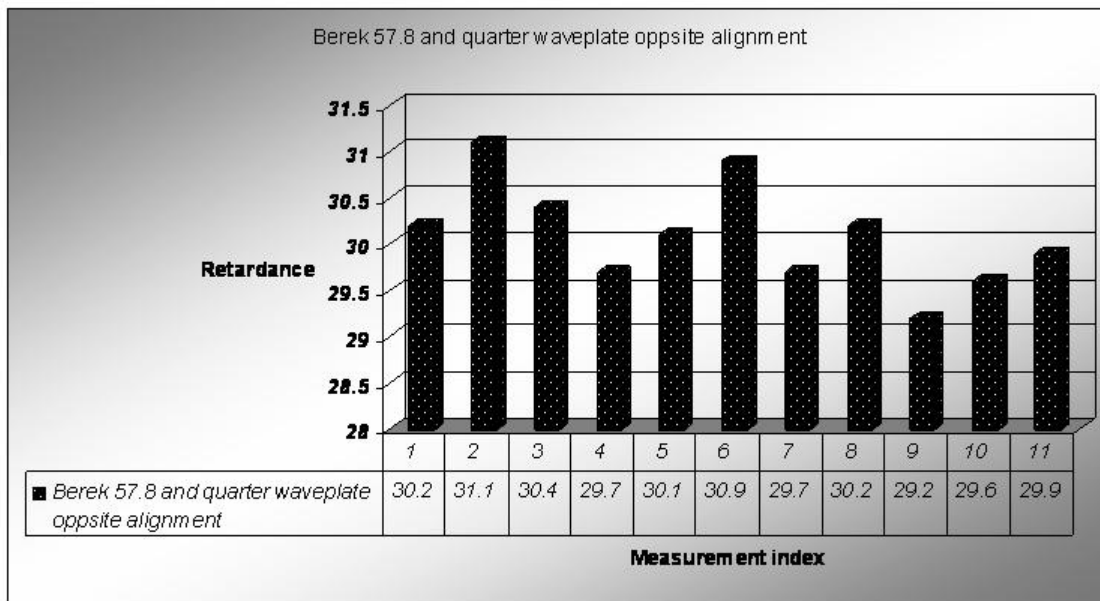


Figure 30: Calibration of Berek compensator

The measurement results of the Berek variable compensator cascaded with a quarter waveplate. The measurement error is 1.4° and the standard deviation is 0.6° when the setting of Berek is 57.8° .

The average retardation measurement error was 2.6° and the standard deviation was 2.1° which agree very well with the purely quarter waveplate calibration results.

A healthy volunteer's retina was imaged using this system under Investigational Review Board approval. Figure 3 illustrates the reflectivity (Figure 3(a)), retardance (Figure 3(b)) and fast axis orientation images (Figure. 3(c)) in the foveal area. The retardance of the top layer of retina was 24.6° , which we attribute to birefringence of the cornea. According to recent research, the appearance of drusen between the choroid and RPE is an indicator of early AMD. Hence the RPE layer plays a critical role in diagnosing the integrity and function of the surrounding photoreceptors and Bruch's membrane.

Both the retardance and the fast axis orientation images show the polarization scrambling properties at the RPE layer which is viewed as a blue, light blue, green and red interleaving band.

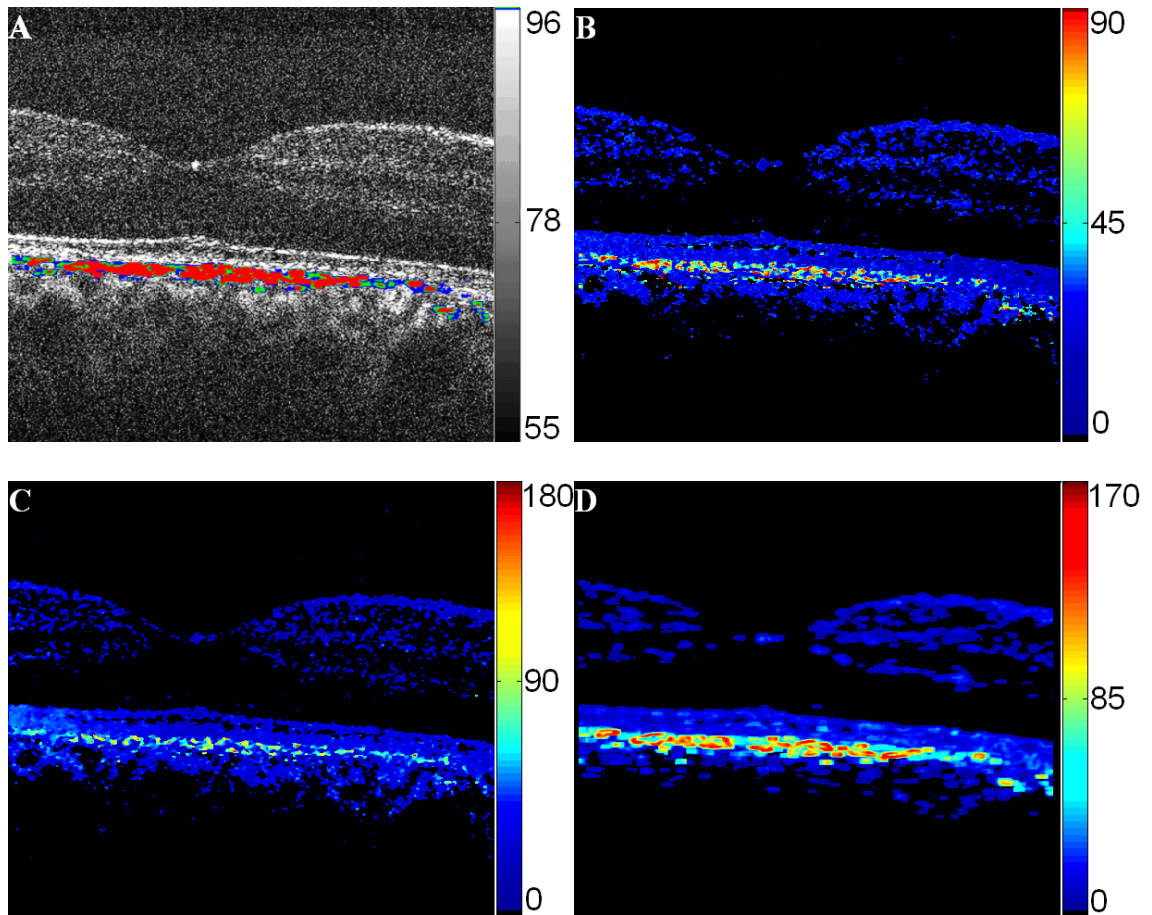


Figure --- (Continued)

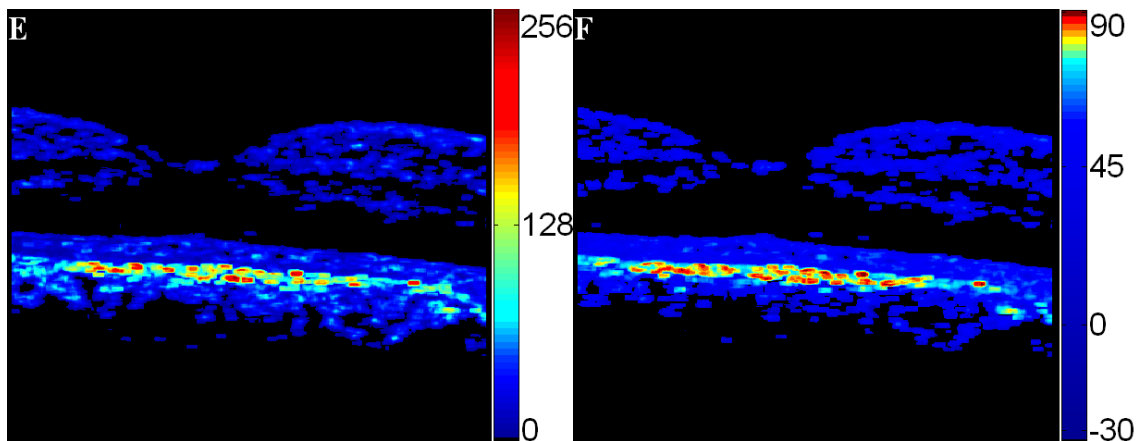


Figure 31: In vivo human retinal imaging results

A: Reflectivity image; image size: $\sim 2.5\text{mm}(x) \times 2.5\text{mm}(y)$, 500-line. The unit of gray color bar is db. Blue: light depolarization (65-70db); Green: middle depolarization (70-75db); Red: strong depolarization ($>75\text{db}$); B: Single pass retardance; the depolarization scrambling RPE layer is viewed as a blue, green and red interleaving band. C: Fast axis orientation; D: The normalized standard deviation of retardance; E: The normalized standard deviation of the fast axis orientation; F: The multiplication image of the standard deviation of retardance and the fast axis orientation. The color bar is in unit of db.

To further quantify the depolarization property of the RPE layer, the normalized standard deviation images of both retardance and fast axis orientation were computed to quantitatively describe the degree of depolarization. A previous report employed a histogram method to segment RPE from the retardance image using a $20(H) \times 8(V)$ size floating window. A floating square window ($5(V) \times 9(H) = 45\text{pixels}$) was adopted to sweep over the entire retardance and fast axis orientation images. A smaller floating window will give a better spatial resolution. The standard deviation calculation was limited to window positions where the average intensity was higher than a threshold set at 68db.

Then the standard deviation was normalized by a factor of effective-pixels/45. The normalized standard deviation images are illustrated in Figure 3(d) and Figure 3(e) respectively. Clearly, the higher standard deviation areas are only centered on the RPE. To further detect the most depolarized locations, the standard deviation of the retardance and the fast axis orientation were multiplied together and the resulting image is showed in Figure 3(f) in the $20\log_{10}$ scale in db units. A fixed threshold 65 db was chosen to extract the RPE layer and the segmented RPE was overlaid with reflectivity image of Figure 3(a). Blue stands for light depolarization (65-70db), green for middle depolarization (70-75db) and red for strong depolarization (>75db) respectively. Despite these encouraging observations, it is important to note that our use of the Jones matrix approach intrinsically assumes polarization maintaining media which does not need Stokes matrix, any post-processing algorithms such as the standard deviation analysis are purely heuristic.

In conclusion, a single channel polarization sensitive SDOCT system using a single spectrometer has been developed for high-speed characterization of total reflectivity, accumulative birefringence and fast axis orientation. This is a novel, simple and relatively easy alignment single camera spectral domain PSOCT system. A unique phase-sensitive algorithm was implemented to precisely detect the fast axis orientation with standard deviation less than 0.7° which is much more accurate than in

contemporary PSOCT systems. A plausible approach for segmentation of the RPE relying on the combination of the standard deviation of the fast axis orientation and that of retardance is suggested, allowing for quantitative measure of the degree of depolarization of the RPE layer.

The work was supported by NIH R01 EY013516. We gratefully acknowledge discussions with Yimin Wang and David Huang from University of Southern California. We thank Kenny Tao for laboratory assistance.

3.4 Materials and Methods of Fiber Based PSOCT

I have also tried a fiber-based polarization sensitive SDOCT. The system layout is illustrated in the below[28]:

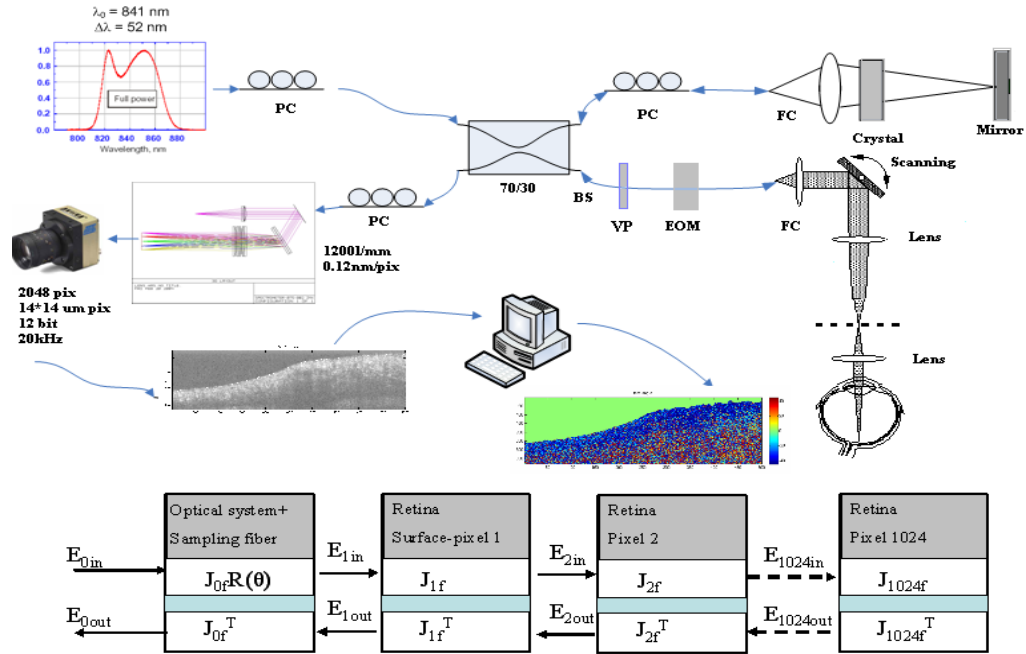


Figure 32: Illustration of fiber based polarization sensitive OCT system

In the above PSOCT system, the light passes through the vertical polarizer, EOM, two galvos, two relay lens, one focusing lens and a mirror. So it can be represented by an unitary Jones matrix J_{in} :

$$J_{in} = J(vp)J(eom)J(galvo)J(relay\ lens)J(focus\ lens)J(mirror) \quad (15)$$

The order of each Jones matrix is not permutable. Then the light reflected back from the mirror goes in the focusing lens, two relay lens, two galvos, EOM, vertical polarizer, optical fiber and the spectrometer optical system. This unitary Jones matrix is called J_{out} :

$$J_{out} = J(mirror) J(focus\ lens) J(relay\ lens) J(galvo) J(eom) J(vp)J(fiber)J(spectrometer) \quad (16)$$

Clearly J_{in} is not equal to J_{out} because of the fiber and the spectrometer system. Generally each optical Jones matrix in the J_{in} and J_{out} can be expressed by the product of $R(\alpha)$, J_{RP} and J_p . It means there will have 5 unknown variables, $\alpha, r, \theta, \sigma_1, \sigma_2$. So there are 30 unknown variables for J_{in} and 40 unknown variables for J_{out} . It will be impractical to model the optical system in this way. According to polarization theory, any physically realizable Jones matrix can be represented as the product of two rotators, two retardation linear plates and one partial polarizer.

$$J_{equivalent} = R(\alpha_1)J_{RP}(\alpha_2, \beta_1)J_p(\sigma_1, \sigma_2)J_{RP}(-\alpha_3, \beta_2)R(-\alpha_4) = J_{in}J_{out} \quad (17)$$

The overall unknown variables are reduced to 8 unknown variables. Hence the polarization states of our optical system can be retrieved in 8 input polarization states. In addition, if the optical system is treated for non-absorbing instruments. 8 unknown variables can be further reduced to 3 unknown variables according to group theory:

$$J_{equivalent} = R(\alpha_2)J_{RP}(\alpha_1, \beta_1) = R(\alpha_2)R(\alpha_1)L(\beta_1)R(-\alpha_1) = J_{in}J_{out} \quad (18)$$

The model is simplified as

$$J_{equivalent} = J_{RP}(\alpha_1, \beta_1) = R(\alpha_1)L(\beta_1)R(-\alpha_1) = J_{in}J_{out} \quad (19)$$

The retardance and fast axis orientation are retrieved from OCT intensity using least square fitting method.

3.5 Results of Fiber Based PSOCT

A quarter waveplate is used to test the system performance. The following figure shows the experimental results[28].

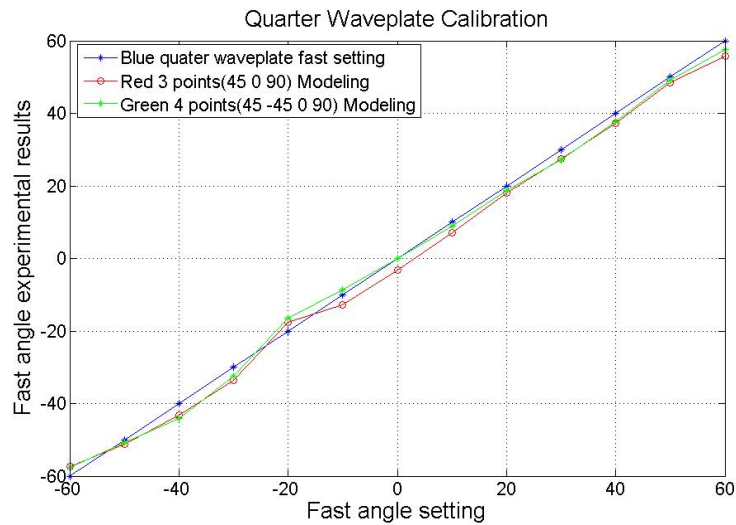


Figure 33: Calibration results of the fast axis orientation

The mean error is 1.9° and the standard deviation is: 2.1° using three polarization states fitting algorithm. The mean error is 0.83° and the standard deviation is 2.1° for four polarization states fitting algorithm.

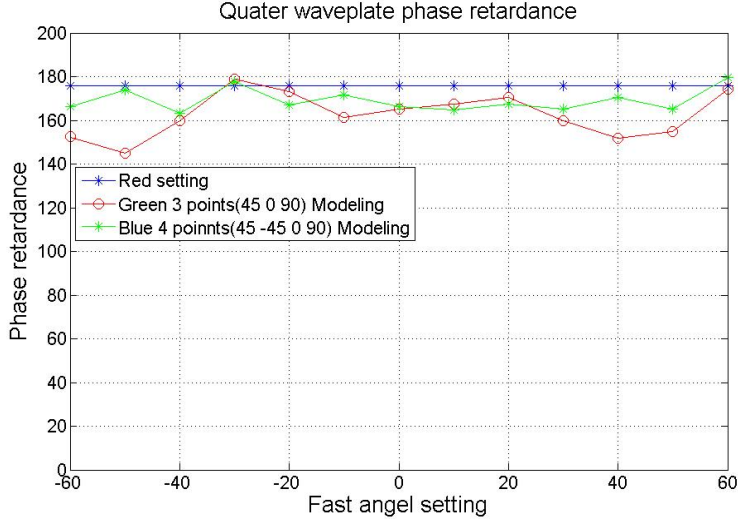


Figure 34: Retardance calibration results

The mean error is 13.2° and the standard deviation is: 10.0° using three polarization states fitting algorithm. The mean error is 6.7° and the standard deviation is 5.2° for four polarization states fitting algorithm.

Discussion for Retinal Imaging:

When we use this method for retinal imaging, the Jones matrix for each A-scan is modeled as:

$$J_{retinal} = J_1^T J_2^T J_3^T J_4^T \dots J_{1024}^T J_{1024} \dots J_4 J_3 J_2 J_1 \quad (20)$$

Where the subscript of J_i means ith layer; T means matrix transpose.

$J_i = R(\theta_i)L(\delta_i)R(-\theta_i)$. θ_i is the fast axis angle. δ_i is the phase retardance of each layer respectively. If the birefringence effect of optical system is combined, then

$$\begin{cases} J_{retinal_A-scan} = R(offset)R(\alpha)L(\beta/2)R(-\alpha)J_1^T J_2^T J_3^T J_4^T \dots J_{1024}^T J_{1024} \dots \\ J_4 J_3 J_2 J_1 R(\alpha)L(\beta/2)R(-\alpha) \\ J_{equivalent} = R(offset)J_{RP}(\alpha, \beta) = R(offset)R(\alpha)L(\beta)R(-\alpha) = J_{in} J_{out} \end{cases} \quad (21)$$

The retinal structures are very complicated. In practical computing, the above model needs a long time to converge. And sometime the least square fitting does not converge very well. A better fitting algorithm could solve this problem. The positive side in this method is that it might be used for other applications, such as thin film thickness measurement. Thin film has a relatively simple structure which will make this algorithm to converge very well.

3.6 Summary

A single-camera, high-speed, polarization-sensitive, spectral-domain optical-coherence-tomography system was developed to measure the polarization properties of the *in vivo* human retina. A novel phase unwrapping method in birefringent media is described to extract the total reflectivity, accumulative retardance, and fast-axis orientation from a specially designed sequence of polarization states incident on the sample. A quarter-wave plate was employed to test the performance of the system. The average error and standard deviation of retardance measurements were 3.2° and 2.3° , respectively, and of the fast-axis orientation 1.2° and 0.7° over the range of 0° – 180° . The depolarization properties of the retinal pigment epithelium were clearly observed in both retardance and fast-axis orientation image. A normalized standard deviation of the retardance and of the fast-axis orientation is introduced to segment the polarization scrambling layer of the retinal pigment epithelium. In addition, a fiber-

based polarization sensitive SDOCT system using a single spectrometer has been developed for high-speed characterization of birefringence and fast axis orientation at a composite rate of 6,000 A-Scans/second, which will enable densely imaging (1000 A-scans/B-scan) at 6 B-scans/sec.

4 Anterior Segment Imaging and Extraction of Clinical Refractive Parameters

4.1 Introduction

Multiple modalities[67-69] currently exist to image the ocular anterior segment. These imaging devices aid in the clinical diagnosis and care of ocular disease. Optical coherence tomography (OCT) is one such technique used to image *in vivo* the ocular anterior segment in a non-invasive fashion. Specific implementations include time-domain OCT systems (e.g. Visante®, Carl Zeiss Meditec) and Fourier-domain OCT systems, including both swept-source and spectrometer-based spectral-domain (SDOCT) implementations. Many previously disclosed anterior segment OCT systems have utilized illumination light in the 1310 nm region[26]. Recently there have appeared several SD-OCT systems utilizing an 840nm light source[70] which are designed for imaging the retina, but which can also be modified with an adapter or a separate patient interface to image the ocular anterior segment. These SD-OCT systems offer the advantage of higher axial resolutions and faster scanning over prior systems.

All OCT imaging systems are subject to the effects of refraction at surfaces corresponding to interfaces between regions of differing refractive index within a sample, including between the air and the surface of the sample as well as internal sample interface surfaces[70, 71]. For a sample such as the anterior segment of the eye, important refractive index interfaces include the outer (epithelial) and inner

(endothelial) surfaces of the cornea, as well as the outer and inner surfaces of the crystalline lens. Additionally, for samples containing regions of different refractive index, it is important for images acquired of the sample to reflect the true physical dimensions of the sample rather than to be distorted by the varying speed of light in different sample regions. Both of these potential pitfalls are particularly important in applications such as corneal biometry where accurate measurements of various clinically significant parameters must be computed from the image data. Such computations are very sensitive to even small image errors due to refraction or distortion. Most current OCT systems do not correct the raw image data for refraction at sample interfaces or for the effects of different sample regions having differing refractive indices. Most current OCT systems instead assume that the light incident on the sample continues in a straight line through the sample and thus plot the raw image A-scan data corresponding to a depth-resolved reflectivity map of the sample on this assumed undeviated path. These systems also do not correct for the effects of different refractive indices in different regions of the sample; at best, they may divide the observed A-scan data by some assumed average index of refraction of the entire sample. As such, raw OCT data in current generation OCT systems does not accurately represent the true position of internal sample structures, and are thus not able to support calculation of clinically significant parameters which depend on accurate image data. In particular, to produce

accurate quantitative measurements of structures of the ocular anterior segment, accounting for the effects of refraction of the sample arm light and for the effects of differing indices of refraction in different sample regions is required.

Prior methods to correct for refraction in OCT images have been described[72]. They do not, however, account accurately or completely for correction of volumetric, three-dimensional (3D) OCT datasets. The first method is limited to 2D processing[26], which assumes that refraction occurs only within the plane of individual acquired B-scans (defined as sets of A-scans acquired along a straight line comprising a cross-sectional image of the sample). For a curved 3D structure such as the cornea, 2D refraction correction is correct only if the sample is rotationally conically symmetric about some axis passing through the apex of the sample, and if the acquired B-scan data passed exactly through the apex point. The first condition is rarely true for realistic samples such as the human cornea, especially if they have been modified surgically. The second condition is true only for idealized radial scan patterns, which may not be optimal because they oversample the central region and undersample the outer region and in any case are difficult to obtain correctly due to unavoidable patient motion or operator misalignment of the OCT system. The other published report does not provide a description of the method[73] used for refraction correction and only shows correction of structures within the optical axis.

One method is to merely use 2D refraction correction via the well known Snell's law. However, this requires one to assume that the corneal surface is rotationally conically symmetric which can be mathematically expressed as[74]:

$$z_{EPI} = z_{Offset} + \frac{1/R \times ((x - x_{offset})^2 + (y - y_{offset})^2)}{1 + \sqrt{1 + K((x - x_{offset})^2 + (y - y_{offset})^2)/R^2}} \quad (1)$$

In the above expression, R is the apex radius of curvature of the surface; K is the conic parameter which represents the asphericity of a surface. $K = 1$ for a sphere and $K = 0$ for a parabolic surface. If this equation were true for the corneal surface, the cornea would be exactly rotationally symmetric, and 2D refraction correction would be sufficient by carefully scanning each B-scan exactly through the axis of rotation (apex). Unfortunately for clinical application, the cornea is not *exactly* rotationally symmetric, and we cannot use the above assumption. This is especially the case in pathologic corneas with gross asymmetry and in surgically altered corneas (LASIK, corneal transplantation), and these corneas are the ones that would benefit most from quantitative imaging.

4.2 Methods of Anterior Segment Imaging

We describe here an algorithm for three-dimensional correction of refraction and index variations within arbitrary samples. The method will be particularly useful for correction of human ocular anterior segment images obtained *in vivo* using SDOCT

systems including extraction of quantitative clinical parameters from 3D OCT datasets acquired in the cornea. A mathematical model and analytical equations for correction of refraction and index variations are provided. We use the commercialized SDOCT at Duke Eye Center from Bioptigen Inc.(Research Triangle Park, NC). The system layout is demonstrated as following:

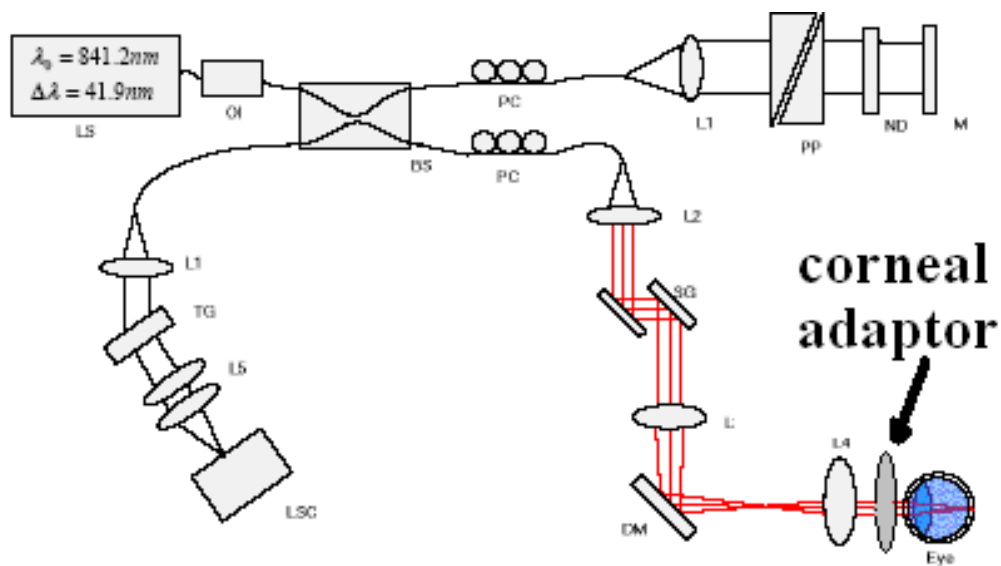


Figure 35: Corneal imaging system

The system design is similar to the original prototype for retinal imaging OCT. The main difference is that an additional corneal adaptor is used to focus the light on the cornea instead of retina. As to the details, please refer to figure 6.

4.2.1 Nontelecentric Correction

To correct non-telecentric effects[71], the pivot scanning distance D of the source was obtained by first acquiring 50 radial B-scans of a square calibration target. The following figure by Volker Westphal illustrates the scanning distance D [71].

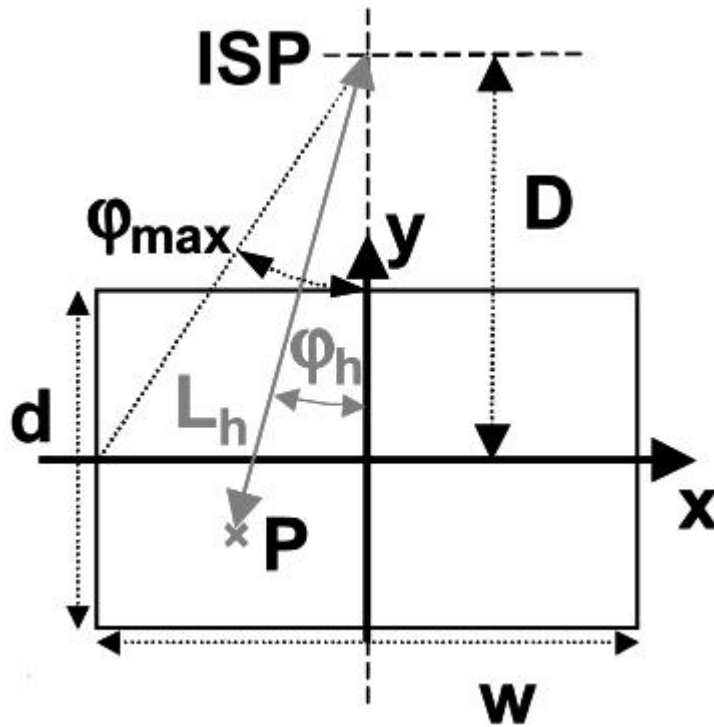


Figure 36: Illustration of the scanning distance D
ISP: image of scanning pivot; d : image depth; φ_h : scanning angle; φ_{\max} : maximum scanning angle; P: corresponding point in the source image.

The deformed non-telecentric scanning field curvature was obtained using automatic image processing. The algorithm is described in equation (1) and illustrated in the following figure.

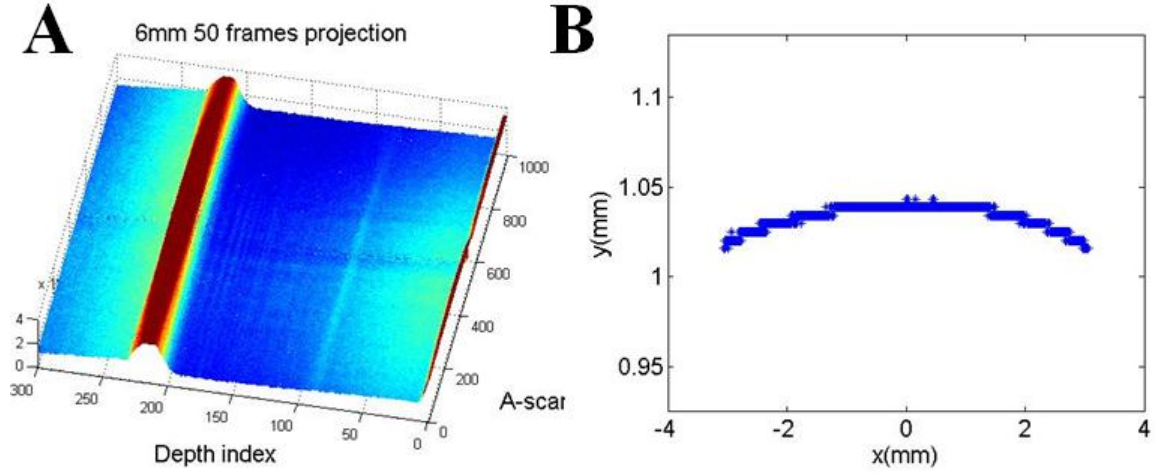


Figure 37: Field curvature caused by the nontelecentric imaging optics
A: Sum projection of 50 radial B-scans of a planar calibration target. The slight curve of the surface (red) results from non-telecentricity. **B:** Ridge of the field curvature.

$$R'(x, y) = \text{Arc tan}\left(\frac{R(x, y)}{D}\right) * D; R = \sqrt{x^2 + y^2} \quad (2)$$

4.2.2 3D Refraction Correction

As illustrated in the following figure, the unit normal vector on the epithelium at point C can be expressed as:

$$\vec{n} = \nabla(z - z_{EPI}) / |\nabla(z - z_{EPI})| = \left(-\frac{\partial z_{EPI}}{\partial x}, -\frac{\partial z_{EPI}}{\partial y}, 1\right) / \left[\left(\frac{\partial z_{EPI}}{\partial x}\right)^2 + \left(\frac{\partial z_{EPI}}{\partial y}\right)^2 + 1\right]^{1/2} \quad (3)$$

The incident light \vec{MC} has directional unit vector (a, b, c) , and the unit vector of the refracted ray:

$$\vec{CC'} = (x - x_0, y - y_0, z - z_0) / [(x - x_0)^2 + (y - y_0)^2 + (z - z_0)^2]^{1/2} \quad (4)$$

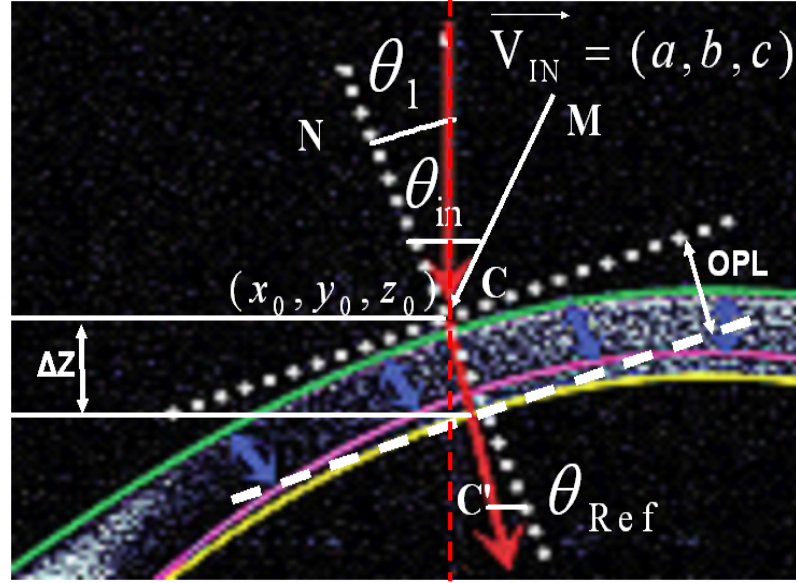


Figure 38: Demonstration of refraction correction

θ_1 : Angle between surface normal of epithelium and z-axis; θ_{in} : incidence angle; θ_{Ref} : refraction angle; OPL: optical path length. Δz : Projection of OPL on z-axis. Where $\vec{V}_{IN} = (a, b, c)$ is the incidence unit vector; (x_0, y_0, z_0) is the coordinate of the epithelium; (x, y, z) is the coordinate of the refraction corrected endothelium; above equation has accounted for the nontelecentric scanning issue. If the incident light is telecentrically scanned, then incident light vector, \vec{MC} , (a, b, c) , becomes $(0, 0, -1)$.

In any realistic biological or industrial sample, the magnetic current densities \vec{M} are zero. According to Maxwell's equations, the electric magnetic field boundary condition can be represented[49]:

$$\vec{h} \times (\vec{E}_{in} - \vec{E}_{ref}) = \vec{M} = 0 \quad (5)$$

$$\vec{MC} \times (-\vec{h}) \cdot n_{air} = \vec{CC}' \times (-\vec{h}) \cdot n_c \quad (6)$$

Here \vec{E}_{in} and \vec{E}_{ref} are the incident and refracted electric fields individually. The first part is the condition for second part of equation (3). After straightforward vector

manipulation, our derivation of Snell's law for use in three-dimensional applications can be represented in the following equations:

$$L = \text{OPL} / n_c \quad (7a)$$

$$z = z_0 + L * \cos(\theta_1 - \theta_{\text{Ref}}) \quad (7b)$$

$$x = x_0 + \frac{a \bullet L}{n_c} - \frac{\partial z_{EPI}}{\partial x} \left[\frac{c \bullet L}{n_c} + (z - z_0) \right] \quad (7c)$$

$$y = y_0 + \frac{b \bullet L}{n_c} - \frac{\partial z_{EPI}}{\partial y} \left[\frac{c \bullet L}{n_c} + (z - z_0) \right] \quad (7d)$$

For the telecentric case, above equations will become,

$$x = x_0 + -\frac{\partial z_{EPI}}{\partial x} \left[\frac{L}{n_c} + (z - z_0) \right] \quad (7e)$$

$$y = y_0 + -\frac{\partial z_{EPI}}{\partial y} \left[\frac{L}{n_c} + (z - z_0) \right] \quad (7f)$$

There are two common scanning patterns employed in ophthalmic imaging. One is raster scanning (stack of sequential B-scans to form a box of images) and the other is radial scanning (each B-scan is centered around a rotational axis). The advantage of the raster scanning is that it provides complete and evenly sampled x , y , and z data throughout the volume (each B-scan exists in the x -axis, the stacking of B-scans creates the y -axis, and the individual points in an A-scan define the z axis). This is ideal for Cartesian implementation of the 3D refraction correction. While the radial scanning

pattern has the advantage of high SNR for all B-scan frames, the data is asymmetrically sampled with denser sampling centrally and less peripherally. For a Cartesian implementation, this requires that the data first be interpolated and then resampled evenly. Alternatively, a polar implementation of equation (7) could be created. The radial scanning pattern is used in this paper.

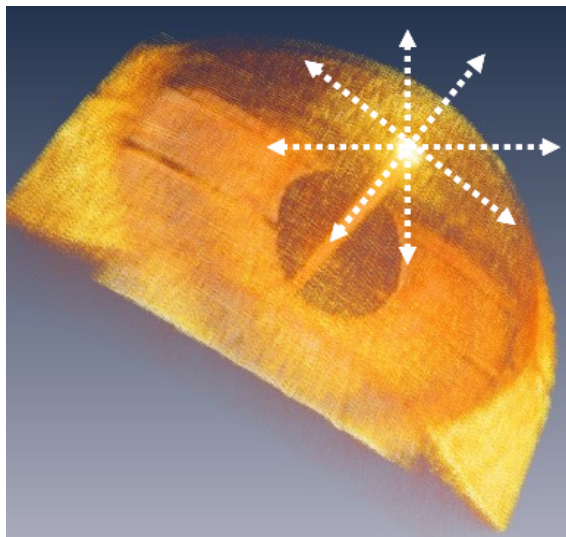


Figure 39: Radial scanning pattern. The scanning B-scan is designed to sweep through the apex

4.2.3 Zernike 3D Interpolations for Radial Scan Patterns

One issue with the newly generated, 3D refraction corrected volumetric data is that the pixels are no longer evenly sampled. As such, we have to devise a means to evenly resample such data for further analysis and visualization. For example, the complete endothelial surface must be reconstructed if we wish to obtain a corneal thickness map (each epithelial normal may no longer intersect a physical endothelial

pixel) or to generate wave front aberration analyses of the endothelium. To reconstruct the even-sampled epithelium and the endothelium surfaces, we employ Zernike polynomial 3D interpolation to obtain the even-grid epithelial, uncorrected endothelial and refraction corrected endothelial surfaces. One direct advantage of using Zernike interpolation to reconstruct the surfaces is to avoid image re-segmentation from the newly generated refraction corrected volumetric dataset.

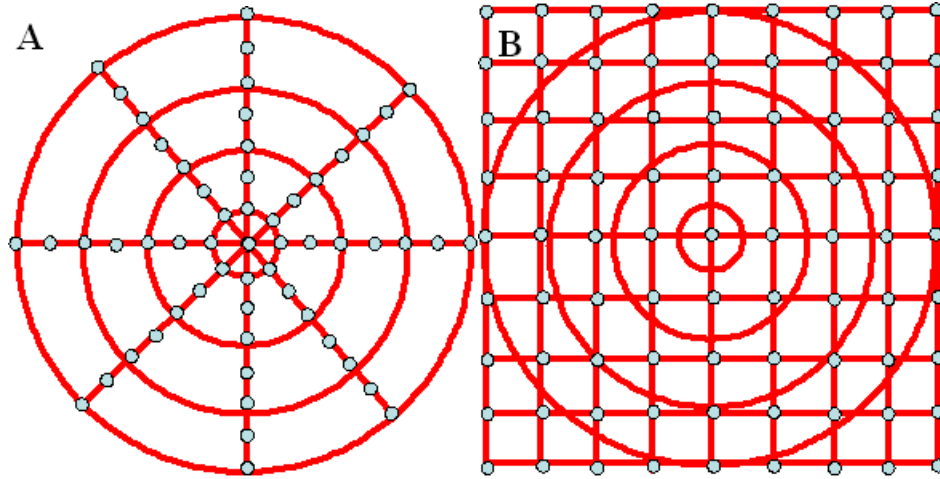


Figure 40: Demonstration of the re-sampling issue in the radial scanning pattern
A: Radial scanning pattern. The sampling points are much sparser in the outer circles than in the inner circles. B: Zernike polynomial even-grid interpolation for both the epithelium and endothelium surfaces based on the noneven-grid radial sampling points.

Zernike polynomials are a set of complete orthogonal polynomials defined on a unit circle. These polynomials are represented in polar coordinates by[75]:

$$Z_i(r, \theta) = R_n^{|m|}(r)\Theta^m(\theta) \quad (8)$$

$$R_n^{|m|}(r) = \sum_{s=0}^{(n-|m|)/2} \frac{(-1)^s \sqrt{n+1} (n-s)! r^{n-2s}}{s! [(n+m)/2-s]! [(n-m)/2-s]!} \quad (9)$$

$$\Theta^m(\theta) = \begin{cases} \sqrt{2} \cos |m| \theta & (m > 0) \\ 1 & (m = 0) \\ \sqrt{2} \sin |m| \theta & (m < 0) \end{cases} \quad (10)$$

$$A(Rr, \theta) = \sum_{i=0}^{\infty} c_i Z_i(r, \theta) \quad (11)$$

$$c_i = \frac{1}{\pi} \int_0^1 \int_0^{2\pi} A(Rr, \theta) Z_i(r, \theta) r dr d\theta \quad (12)$$

The indices n and m are the radial degree and the azimuthal frequency respectively; i is a mode-ordering number; R is used to normalize the measurement data to a unit circle and c_i is Zernike elevation interpolation coefficients. Above figure shows the procedure for Zernike 3D interpolation.

Zernike 3D interpolation is necessary for all surfaces in non-raster scan patterns (such as radial scan patterns). In a radial scan pattern, the central area of the scan is sampled more densely than that in the periphery. Figure 38 illustrates the sampling density in the radial scanning case. This applies to all scan patterns which sample unevenly (with respect to x and y).

The interpolation procedure for this case is summarized as following:

(1) Segment both the epithelium and endothelium surface.

- (2)Employ an 8th-order Zernike polynomial fitting to interpolate both surfaces into an even-grid sampling space.
- (3)Calculate the surface partial differential equations of the epithelial surface.
- (4)Use equation (10) to obtain the refraction corrected endothelium surface.
- (5)Utilize the Zernike 3D interpolation again to reconstruct the refraction corrected endothelial surface.

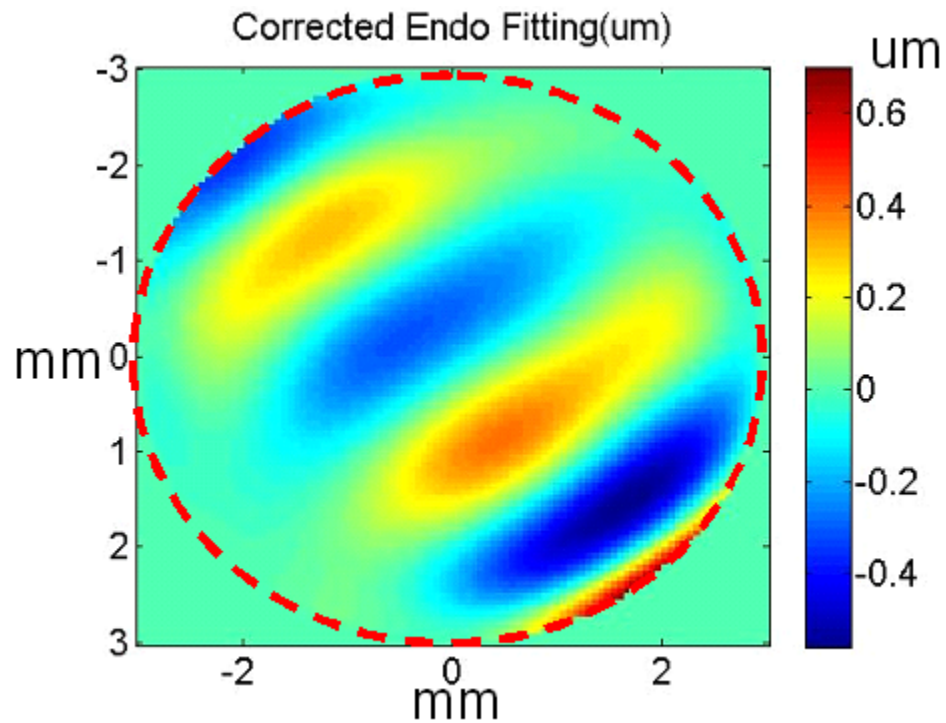


Figure 41: Zernike fitting

Illustration of the 8th order Zernike fitting residue errors of the refraction corrected inner surface of a phantom rigid contact lens. The maximum fitting error is less than 0.7 micrometers.

4.3 Extraction of Clinical Refractive Parameters and Wave Aberration

4.3.1 Corneal Thickness Mapping

The corneal thickness is measured along the epithelial surface normal vector. The surface normal equation of the epithelium is obtained by:

$$\frac{(x-x_0)}{\partial F(x,y,z)/\partial x} = \frac{(y-z_0)}{\partial F(x,y,z)/\partial y} = \frac{(z-z_0)}{-1} \quad (13)$$

(x_0, y_0, z_0) stands for the coordinate of point C; (x, y, z) stands for the coordinate of an arbitrary point on the normal equation (line). It is difficult to derive an analytical solution between equation (17) and (18). A numerical solution called the recursive half searching algorithm (RHSA) is disclosed here to solve this problem. The principle is illustrated in the following figure. The idea is to search for the intersection between the epithelial surface normal equation and the endothelium.

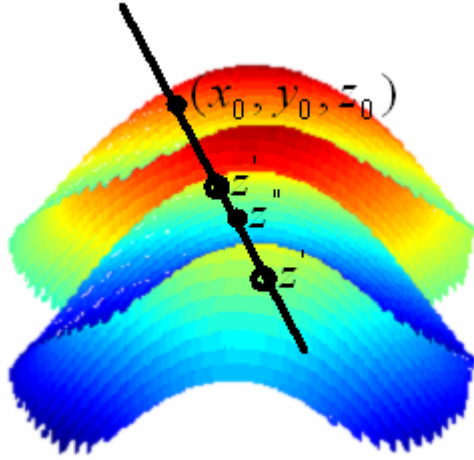


Figure 42: Principle of searching intersection points between the surface normal equation of epithelial and refraction-corrected endothelial surface
The top surface is epithelium and the second is endothelium. z' : Obtained using equation (13) after half distance recursion; z'' : retrieved using Zernike coefficients in equation (11).

The starting guess point is the refraction uncorrected endothelium (x, y, z) . The new coordinates of (x, y, z) of the first step can be estimated by manipulating equation

(14)

$$\text{Step 1: } \begin{cases} z' = z(\text{uncorrected endothelium position}) \\ x' = x_0 - \partial F(x, y, z) / \partial x_{(x_0, y_0, z_0)} (z' - z_0) \\ y' = y_0 - \partial F(x, y, z) / \partial y_{(x_0, y_0, z_0)} (z' - z_0) \end{cases} \quad (14)$$

$\partial F(x, y, z) / \partial x_{(x_0, y_0, z_0)}$ and $\partial F(x, y, z) / \partial y_{(x_0, y_0, z_0)}$ are the constant partial derivatives of the epithelial surface at point C, and we do not need to calculate them

again. In step 2, we will determine if the new point (x', y', z') is located at the Zernike interpolated endothelial surface.

$$\text{Step2: } \begin{cases} z'' = \sum_{i=0}^{\infty} c_i Z_i(r(x', y', z'), \theta(x', y', z')) \\ \text{if } |z' - z''| \leq \varepsilon, \text{ then stop and } (x', y', z') \text{ will be the target point} \end{cases} \quad (15)$$

ε is the stop condition which we have defined as 1 micrometer in our case. Step 3 will be followed if it does not reach the convergent accuracy.

$$\text{Step 3: } \begin{cases} \text{if } |z' - z''| > \varepsilon \text{ then} \\ z' = z' + |z' - z''| / 2 \quad \text{if } z' < z'' \text{ search point is below endothelium} \\ z' = z' - |z' - z''| / 2 \quad \text{if } z' > z'' \text{ search point is above endothelium} \\ \text{Repeat Step 1 and Step 2} \end{cases} \quad (16)$$

The above search method will recursively halve the difference of the search distance. Hence it converges very fast and only needs 6 steps to define the intersection point.

Another method is to use ray tracing and Newton's algorithm to find the intersection point along the Newton search direction.

$$\text{Newton Search Direction} = \left[\frac{\partial G(x, y, z)}{\partial x} l, \frac{\partial G(x, y, z)}{\partial y} m, \frac{\partial G(x, y, z)}{\partial z} n \right] \quad (17)$$

$G(x, y, z) = 0$ is the implicit form of the endothelium and the direction cosines of the epithelial surface normal equation are represented in (l, m, n) which is related to the epithelial surface derivatives. This method requires iterative calculation of all the partial

derivatives, $\left[\frac{\partial G(x, y, z)}{\partial x}, \frac{\partial G(x, y, z)}{\partial y}, \frac{\partial G(x, y, z)}{\partial z}\right]$ of the intermediate approximation

points on the endothelium. So it is computationally more intensive. In addition, the intermediate partial derivatives of the endothelial surface are much more sensitive to the noise which influences the convergence.

4.3.2 Corneal Wavefront Aberration Analysis

After 3D refraction correction, we can estimate the individual wavefront aberration of the epithelium and endothelium layers. Similar to the method employed in professional optical design software Zemax™, the optical path differences, also called wavefront aberrations, W_a , between the off-axis and on-axis for the all meridians are calculated within 7-millimeters. The following figure shows the Zernike patterns.

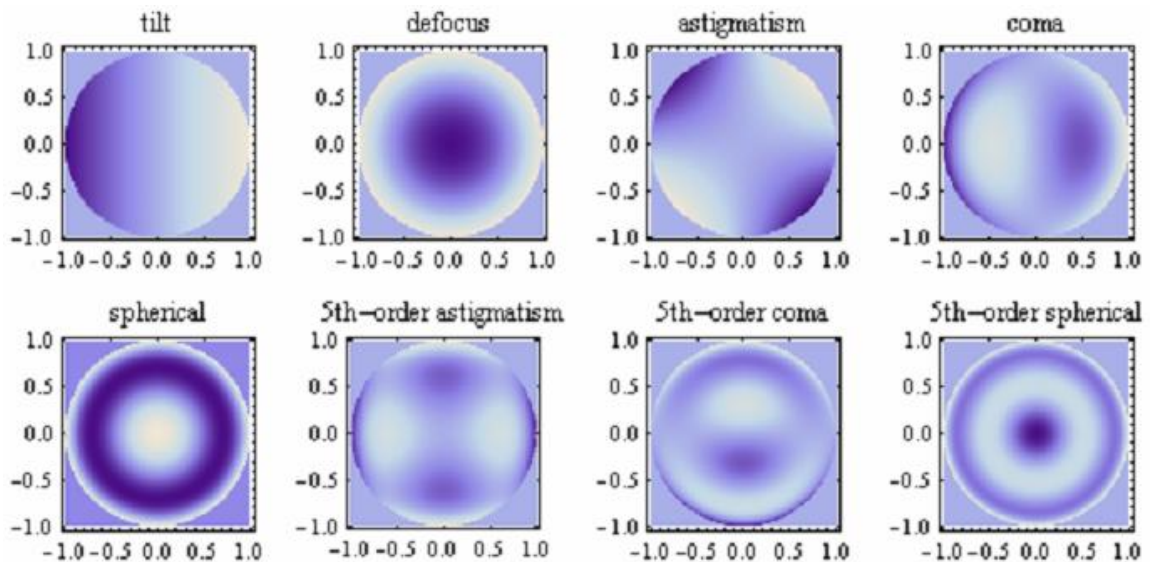


Figure 43: Illustration of different Zernike wave aberration errors

Equation (18) gives the computing method[74].

$$W_a = n_{\text{Cornea}} \bullet f - n_{\text{Air}} \bullet Z_a - n_{\text{Cornea}} \bullet d \quad (18)$$

$$C_i = \frac{1}{\pi} \int_0^{2\pi} \int_0^1 W_a(Rr, \theta) Z_i(r, \theta) r dr d\theta \quad (19)$$

C_i describes the wavefront aberration coefficients. For example, C_{13} (with mode index=1) is called spherical aberration error. The Zernike spectrum is illustrated in the following figure. The spherical aberration error of the epithelium is around 1.1 micrometers and -0.6 micromeres for the endothelium.

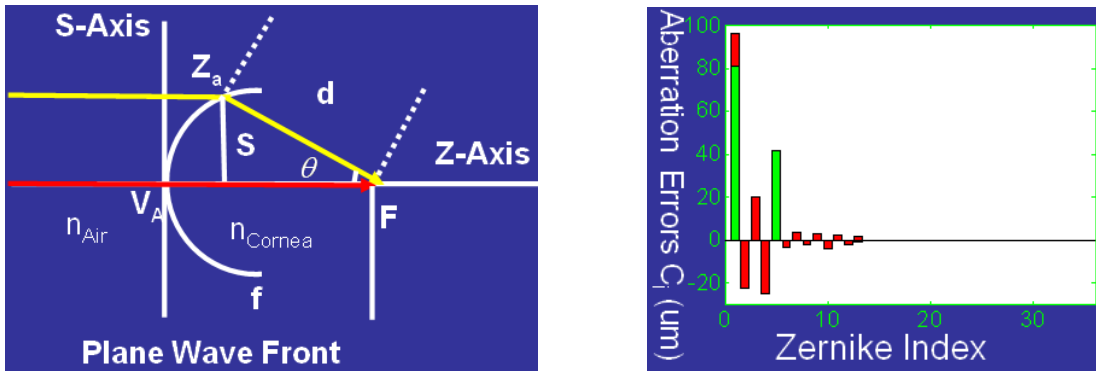


Figure 44: Illustration of wavefront aberration analysis using Zernike spectrum analysis and ray tracing

A: The anterior surface corneal height is labeled Z_a , f is the distance of the focus point (F) to the apex of the surface V_A , and d is the distance of this focus point to an arbitrary point on the surface. B: Zernike aberration analysis of the cornea. Red is for anterior surface and green is for posterior surface. Overall the anterior surface contributes much more aberration errors than that of posterior surface.

4.3.3 Refractive Curvature, and Best Fit Sphere Analysis

Best sphere fitting are used to estimate the asphericity, surface curvature, and to create float maps. Asphericity (K) and the radius of curvature for a surface (R) are

obtained using 3D fitting with Eq. (1). Using a phantom contact lens, the measurement error of the base curvature from that reported for the phantom was less than 2.9%. The radius of curvature is used to describe the refractive power of the cornea either over an optical region (for instance, refractive power within the central 3mm optical zone) or locally over the entire cornea to produce a local refractive curvature map.

Best sphere fitting is retrieved using 3D fitting by simply letting $K=1$ in equation (1). The results are demonstrated in the following figure. The residuals demonstrate the amount of deviation of the corneal surface from that of the best fit sphere. This is a clinically important indicator of ectatic corneal conditions.

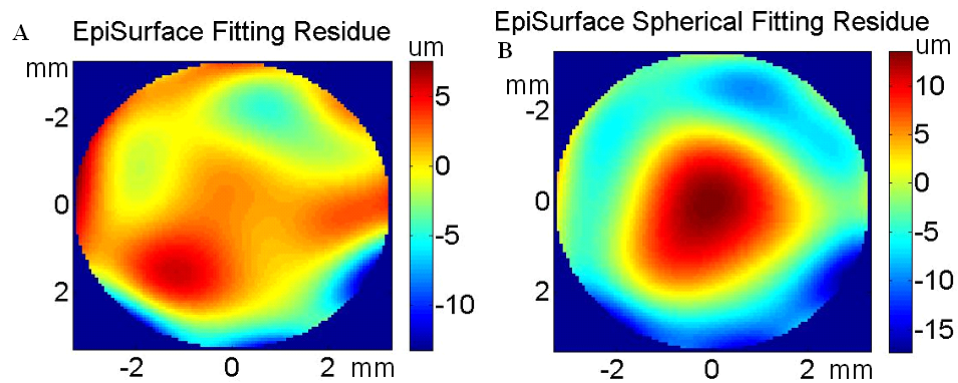


Figure --- (Continued)

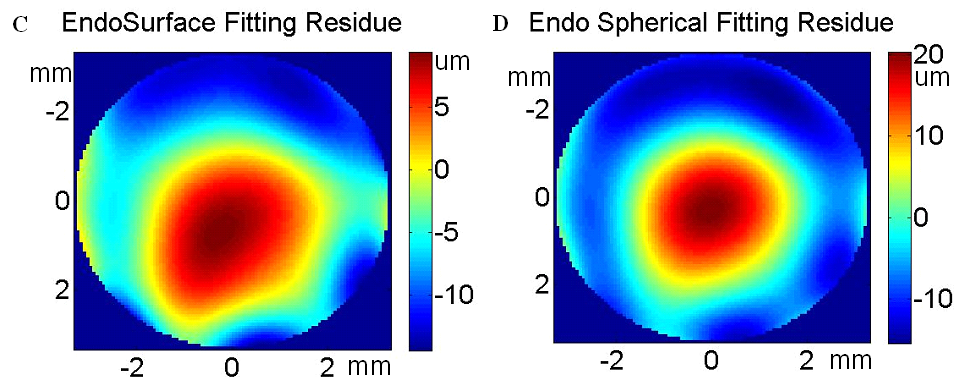


Figure 45: Float images of different 3D fitting of a phantom contact lens.

A: Float image of the anterior surface of a contact lens with asphericity fitting. Asphericity is 0.8 and radius is 10.03 mm. **B:** Flow image of the posterior surface of a contact lens with best sphere fitting. **C:** Float image of the posterior surface of a contact lens with asphericity fitting. Asphericity is 0.59 and radius is 9.32 mm (d) Float image of the posterior surface of a contact lens with best sphere fitting.

4.3.4 Measurement Refractive Index of Human Cornea

To accurately estimate the curvature of the endothelium surface of the cornea, we need to know the exact value of the group refractive index of the cornea. There is no publication result available for our central wavelength. There are only two groups which have reported the refractive index measurement at different wavelengths in time domain OCT[69, 76]. However there is no cornea image in their reports. They only show the OCT scattering signal in single A-scan. We use a human cornea from a donor to measure it group refractive index. In addition, we have captured clear controlled cornea

B-scan image. The group refractive index can be found using the following dispersion equation:

$$\beta(\omega) = \beta(\omega_0) + (\omega - \omega_0) \frac{\partial \beta}{\partial \omega} \Big|_{\omega_0} + \frac{1}{2} (\omega - \omega_0)^2 \frac{\partial^2 \beta}{\partial \omega^2} \Big|_{\omega_0} + \frac{1}{6} (\omega - \omega_0)^3 \frac{\partial^3 \beta}{\partial \omega^3} \Big|_{\omega_0} + K \quad (20)$$

The first term introduces a constant phase shift over all frequencies[8, 54] and can be ignored. The second term which is the inverse group velocity indicates the linear phase shift with frequency, leading to no internal change to the light pulse. The group velocity is

$$V_g = \frac{\partial \omega}{\partial \beta} \quad (21)$$

As to OCT, we care about the group propagating speed of the envelope of the broadband light. Hence we need to use group refractive index to estimate the optical path length in the cornea. The group refractive index is defined as following,

$$n_g = \frac{c}{V_g} \quad (22)$$

c is the speed of light in the vacuum. It is related to the phase refractive index, n_p , as following,

$$n_g = n_p [1 + (\lambda / n_p) (dn_p / d\lambda)] \quad (23)$$

To measure the group refractive index of the cornea, the cornea is hold in a 1mm cuvette. The cuvette is then filled with optisol GS to prevent drying the cornea. To

maintain the experimental temperature, the cornea was put to sit in optisol at 21°C for 2 hours before the experiment. The optical path length with and without cornea is measured. From the difference of the optical path length, we can measure the group refractive index of the cornea.

However this is a strong reflection of OCT signal if the incident light is perpendicular to the cuvette. As a result, the OCT image is completely saturated. The following figure shows the saturated OCT image. It is hard to discriminate the corneal signal from the background noise.

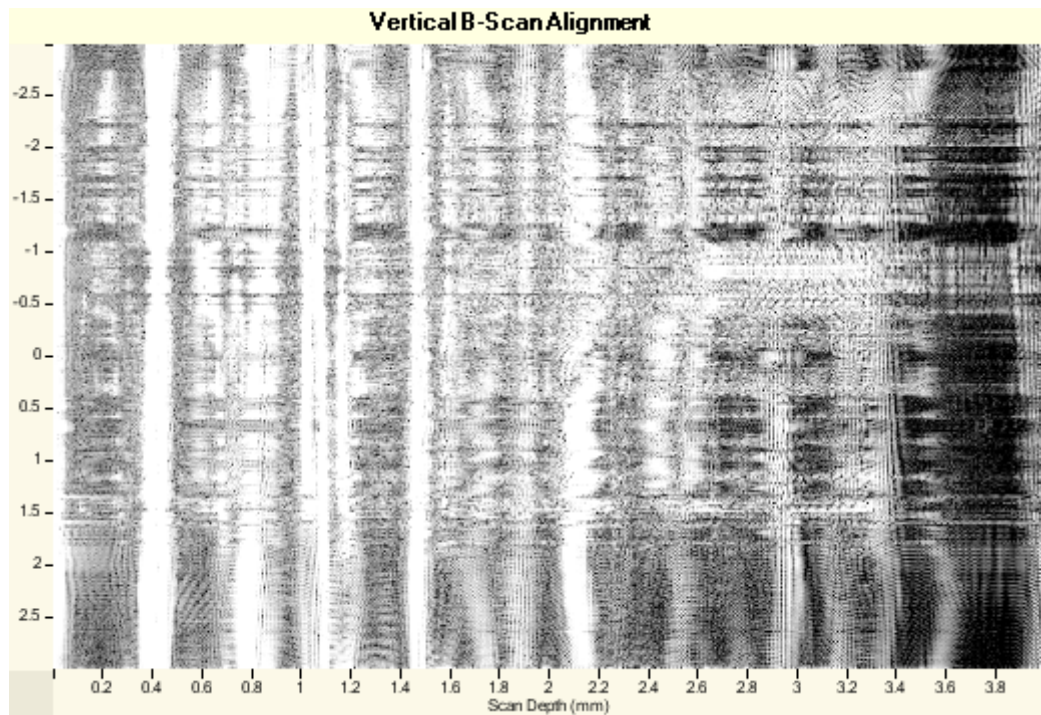


Figure 46: Saturated corneal image at perpendicular incidence case

To solve the saturation problem, we tilt the incident beam on purpose. Since both the cornea and optisol tilt at the same angle, so it does not influence the measurement results.

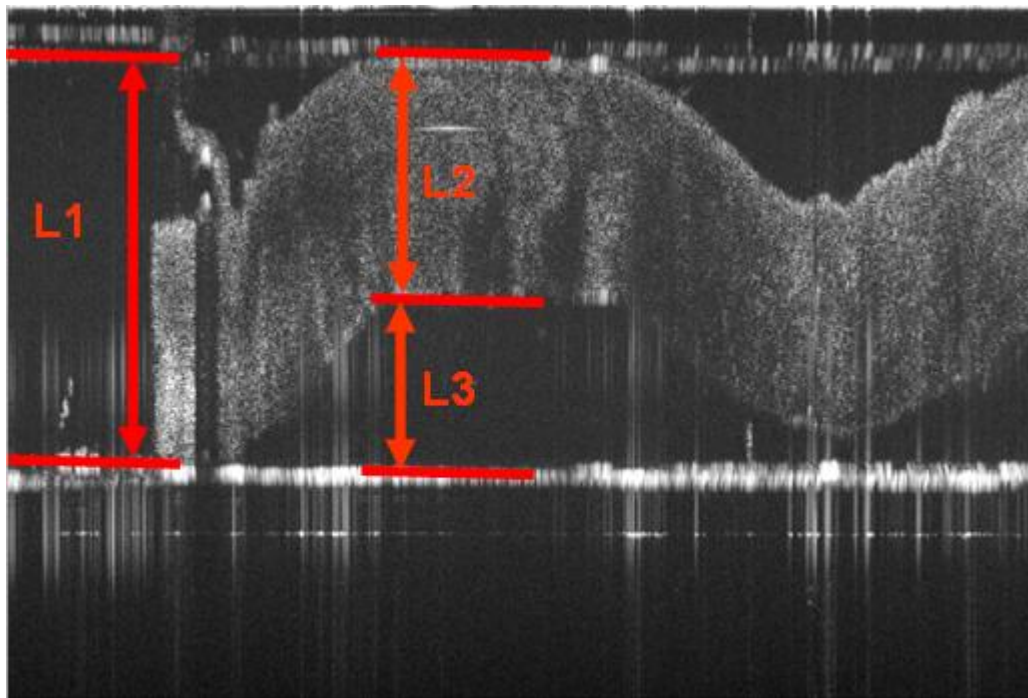


Figure 47: Corneal image captured at a tilting incidence angle
The cuvette is filled with optisol. L1 is the optical path length of the cuvette; L2 is the optical path length of the cornea; L3 is the optical path length of optisol below the cornea area.

To measure the group refractive index of the human cornea, we first measure the group refractive index of optisol[69]. This is very straightforward. It can be explained by the following equation

$$n_{\text{Optisol}} = \frac{\text{optical path length of cuvette with filled optisol}}{\text{optical path length of empty cuvette}} \quad (24)$$

40 averaged images at five individual points are used to obtain the group refractive index and the average result is

$n_{\text{Optisol}} = 1.350 \pm 0.003$. According to above figure, the group refractive index of cornea can be retrieved by solving the following equation:

$$\frac{L1}{n_{\text{optisol}} \cos(\alpha)} = \frac{L2}{n_{\text{cornea}} \cos(\alpha)} + \frac{L3}{n_{\text{optisol}} \cos(\alpha)} \quad (25)$$

Where α is the tilting angle, which will be canceled out on the both sides. The measured group refractive index of cornea is 1.387 ± 0.008 using 40 images at five individual measurement points, which is slightly bigger than the literature value(central wavelength at 855nm) 1.3817 ± 0.0021 [76]. However there is a approximation in the measurement method in this literature[76].

4.4 Statistical Experimental Design for Clinical Application

4.4.1 Statistical concepts

In designing an experiment, a hypothesis is typically formed to explain observed phenomena. This hypothesis is then tested by the experiment to assess its validity. In clinical studies, the hypothesis usually takes the form of a null hypothesis (and related alternate hypothesis). For instance, a null hypothesis may state that the efficacy of drug A is no different than drug B for some disease condition. The related alternate hypothesis would be that the efficacy of drug A is different from drug B. Statistical

decision making is then used to accept or reject the null hypothesis and conversely reject or accept the alternate hypothesis.

In this type of decision making, errors can occur. For instance, we can reject the null hypothesis when in fact we should have accepted it. As a concrete example, consider a pregnancy test. The null hypothesis would be that the individual is not pregnant. If our pregnancy test is positive, we would reject this null hypothesis. However, if the individual truly was not pregnant (for instance, if we tested a male individual), then we would have erroneously rejected the null hypothesis that the person was not pregnant. This type of error is termed a Type I error – that is, we rejected the null hypothesis when it was in fact true. This type of error is also termed α error or a false positive.

The related Type II error occurs when we erroneously accept the null hypothesis when it was in fact false. Using our example, consider the situation when our pregnancy test was negative when the woman was in fact 9 months along. The test result caused us to falsely state that the woman was not pregnant. This type of error is termed β error or a false negative.

A useful related term is power. This is defined as $1-\beta$. Conceptually, $1-\beta$ gives us the probability of true negatives. Again, using our example, it is the number of times our

pregnancy test is negative when the tested individual truly is not pregnant (Total negative tests – False negative tests).

There are conventions in clinical studies regarding the amount of tolerable errors. Typically, we are willing to accept an α of 0.05 and a β of 0.20. That is, we are willing to accept at maximum a 5% chance that we will have inadvertently rejected the null hypothesis when it was in fact true (a 5% chance of making a false positive claim). The maximum β of 0.20 results in a minimum power of 0.80. That is, we desire at minimum an 80% chance of correctly accepting the null hypothesis when it is truly correct (at minimum, an 80% chance of making a true negative claim). With these acceptable constraints, we can then proceed to design, carry out, and interpret our clinical study.

This instrument study seeks to determine if there are differences between corneal parameters measured by SDOCT versus that measured by topography or Scheimpflug photography. Because we will be measuring the same individual with multiple instruments, each data value is not independent – measurements from the same person are related. To correctly pair the data from the same individual, we will examine differences between measurements. For example, for subject n , we will record the differences between corneal powers measured by SDOCT and topography ($\text{SDOCT}_{\text{subj } n} -$

topography_{subj n}). Assuming the two distributions with same variance, we can calculate a test statistic for our data based on a t distribution[77].

$$t = \frac{\bar{x}_1 - \bar{x}_2}{s \sqrt{\frac{1}{n_1} + \frac{1}{n_2}}} \quad (26)$$

Where \bar{x}_1 and \bar{x}_2 are the average measurement values of SDOCT and topography, n_1 and n_2 are sample size for SDOCT and topography. $s = \sqrt{[(n_1 - 1)s_1^2 + (n_2 - 1)s_2^2] / (n_1 + n_2 - 2)}$, s_1 and s_2 are their standard deviation respectively.

From this test statistic, we can determine the corresponding p-value. The p-value can be thought of as the probability of obtaining a test statistic at least as extreme as the one described by our data if the null hypothesis were indeed true. That is, what is the likelihood of obtaining our observed data if there was no difference between the instruments. This p-value can be compared to our predetermined α value to allow us to make a statistical decision regarding our null hypothesis. If the p-value is less than our defined significance ($\alpha = 0.05$), then we can reject the null hypothesis that our tested instruments are not different.

However, in this case, our actual desire is to show that the SDOCT is comparable to existing instruments. Our expectation is to keep the null hypothesis, and we desire to design an experiment that will demonstrate no difference if there truly is no difference

between the instruments. To design this type of experiment, we need to be cognizant of our accepted statistical constraints. To reiterate, we want an 80% probability (power) of correctly accepting the null hypothesis when there truly is no difference. Power is affected by effect size, standard deviation, and sample size. The effect size is the decided difference which is clinically significant; in the case of corneal power, this would be 0.25D – the resolution of current conventional treatments for refractive errors. The standard deviation of the difference between SDOCT and topography power measurements based on time domain systems and prior literature is roughly estimated to be 0.50D[26]. As our instrument is new, we will use this estimate as we have no pre-existing data from our own instrument. We can now calculate the minimum sample size required to be using following paired t-test equation[77]:

$$n = \frac{\sigma^2(t_{1-\beta} + t_{1-\alpha})^2}{(\bar{x}_1 - \bar{x}_2)^2} \quad (27)$$

Where σ is the variance of $\bar{x}_1 - \bar{x}_2$.

We can also perform pairwise intraclass correlations to determine the correlation or agreement between our instruments. This value will range from 0 (no correlation) to 1 (complete agreement) to give us a quantitative measure of how well the measurements from the instruments are agreeing. A 95% confidence interval of this correlation measurement can be calculated as well.

A qualitative and graphical way to represent agreement is via a Bland-Altman plot [78]. In this type of plot, the reference value is taken as the average of the measurements made by the two instruments. This is plotted on the abscissa. The difference between the measures is plotted on the ordinate axis. In this type of plot, complete agreement would result in a straight line mean difference of zero. Lines representing the 95% confidence interval of this mean are also plotted.

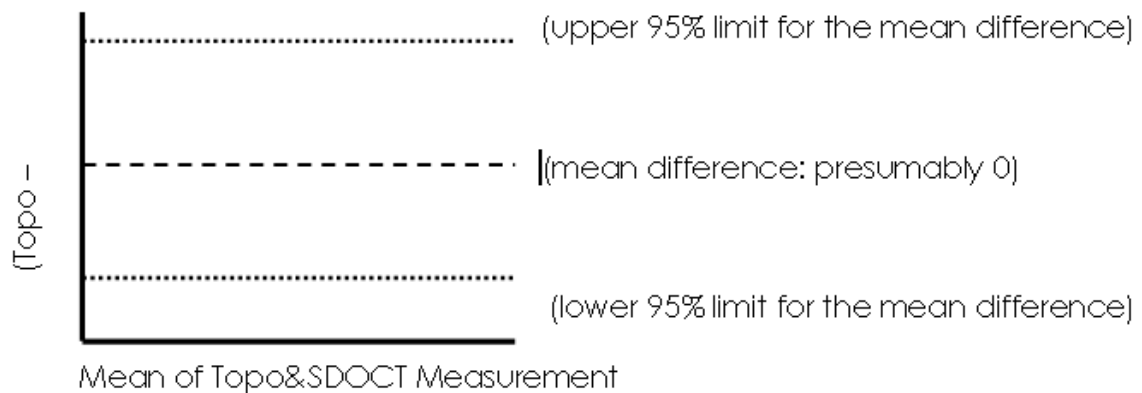


Figure 48: Graphic representation of Bland-Altman plot

This type of plot allows us to graphically examine the difference and possible trends in the data.

Other statistical terms which are commonly used in clinical trials are sensitivity and specificity of clinical tests. These are used in instances where there are binary states such as the presence or absence of a condition (pregnancy, a particular disease, etc.) as defined by a “gold standard”. Sensitivity refers to the ability of a test to identify true positives (probability that the test will identify an individual who truly has the

condition). Specificity refers to the ability of a test to identify true negatives (probability that the test will identify or clear an individual who truly does not have the condition). The terms are related and increasing one will decrease the other. For instance, a test would have high sensitivity if it automatically declared everyone positive – all individuals with the condition will have a positive test result. However, all individuals without the condition would also have a positive test result in this scenario, and thus, the specificity would be very low. Receiver operator curves are graphical representations of this trade off and can be used to determine appropriate cut-off points for binary tests. In our study, however, we are examining continuous data measurements rather than binary states, so these concepts are not directly applicable to our current study.

To summarize, we will use several methods to assess the agreement between SDOCT, topography, and Scheimpflug photography in measuring corneal refractive parameters. 1) Initially, we will compute overall and pair-wise intra-class correlations with their 95% confidence intervals. These will be used as the true measures of agreement. . 2) Then, we will carry out paired t-tests to determine whether the mean difference between measurements is significantly different from zero. 3) In addition, to provide additional information regarding the nature of any differences between measurement techniques, we will provide Bland-Altman plots.

4.4.2 Preliminary Pilot Clinical Study Results

A pilot study was initiated to provide preliminary information regarding the performance of SDOCT in measuring corneal power compared to other pre-existing instruments (topography and Scheimpflug photography/Pentacam). The study would also provide valuable information regarding the performance of SDOCT in regards to standard deviation of measurements in the preparation and design of future clinical studies.

Before the study, a power analysis calculation was performed to determine the minimum sample size needed to achieve a empiric power of 0.80 and to detect an standard clinical acceptable effect size of 0.25D given an estimated standard deviation of 0.44 D[79] between the difference of OCT and topography measures of corneal power. This estimation was derived from a previously published study that compared OCT against an instrument the uses Placido ring technology (same concept as topography). We use this estimation as there is no prior experience with our SDOCT in quantitative corneal measurements, and the exact difference between other OCT systems and topography has not been published. The minimum sample size was found to be 27 eyes using commercial statistical software JMP™ (Cary, North Carolina). In this calculation, the input parameters are listed as following: defined significance $\alpha = 0.05$; the estimated standard deviation is 0.44 D, the difference to detect is 0.25D and power is 0.8. Above

input setting are standard parameters except that 0.44D is from David Huang's paper [79].

4.5 System Calibration and Phantom Results

4.5.1 Lateral Scanning Range Calibration

To calibrate the lateral range of the system, both raster scanning and radial scanning patterns are employed to measure the physical scanning range of the SDOCT system. The scanning range is calibrated using three targets from Edmund Optics Company. The calibrated scanning range is 6.125 ± 0.009 mm which is obtained from 13 measurement points. In the radial scanning pattern of Bioptigen retinal imaging system, I have found that the bottom part image deviates $49 \mu\text{m}$ from the vertical central line. Above number is obtained using a dual axis linear scale stage micrometer. This is a built-in issue in this system.

I have corrected this problem in the post processing using software.

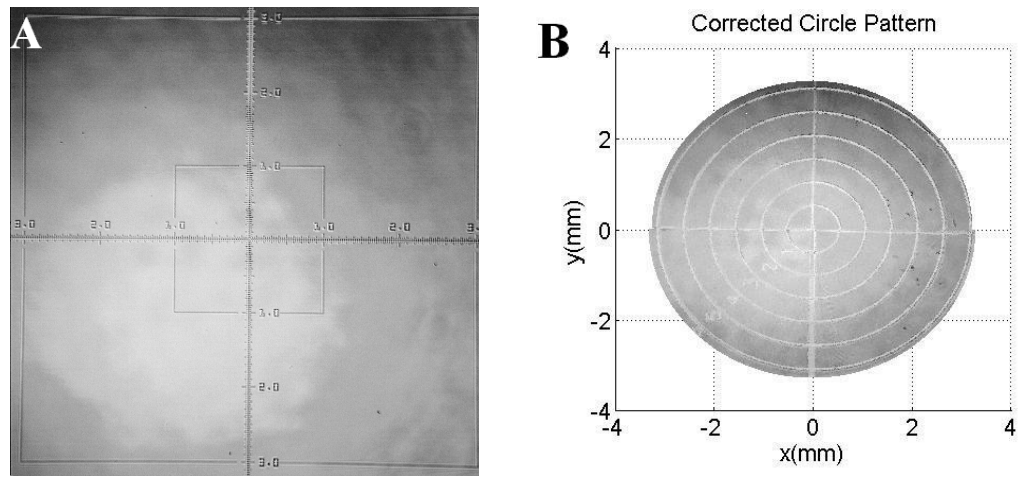


Figure 49: Lateral resolution calibration of SDOCT

A: Raster scanning of a phantom optical target ruler (dual axis linear scale stage micrometer, a metric scale featuring 25 μm , Edmund optics). **B:** Radial scanning of circular optical target (opal glass concentric circles reticle target, Edmund optics). The unit of the mark is mm. Both images are obtained using surface volume projection from 3D OCT volumetric dataset. Least square fitting at marked points (-3,-2,-1, 0, 1, 2, 3) is used to get the lateral scanning range using (opal glass concentric circles reticle target).

4.5.2 Axial Scanning Calibration

The axial scanning range is the maximum imaging depth of OCT, which is described in the following equation and related to equation (6) in chapter 1:

$$Z_{\max} = \frac{\pi}{n\delta k} \quad (28)$$

The theoretical calculation result is 4.35mm. In the actual application, we found that the value is not exactly correct. Hence I try to calibrate the maximum imaging depth using two methods. The first method is to use a glass cover slip with known thickness and refractive index. The top surface of the cover slip functions as the reference arm, the

second surface is treated as sample arm. Actually this is a common mode OCT system; we even do not need the physical reference arm in the SDOCT system. This common mode method significantly reduces the effects of image blur caused by the dispersion compensation. The refractive index of BK7 at 840nm is 1.51, which is obtained from <http://refractiveindex.info>. The physical thickness of the glass cover slip is measured by a tool of micrometer. The measurement result is 4.690 ± 0.020 mm . The following figure shows the calibration principle.

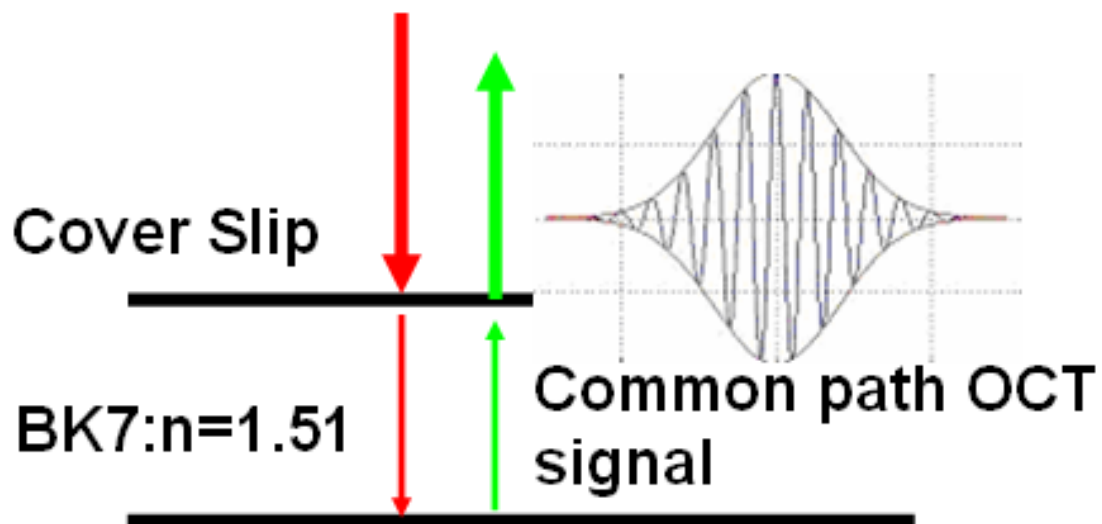


Figure 50: Maximum imaging depth calibration using glass cover slip

As to the second method, we put a mirror on a z translation stage. Two image were captured when the mirror in different position. The physical distance between two mirrors is 1mm. The calibrated result is 4.700 ± 0.016 mm . The calibration result is very

accurate, which is confirmed by the phantom test. Those two calibration results are pretty close. The difference is only around $10\mu\text{m}$.

To test the all the 3D refractive correction algorithm and the accuracy of the system calibration, one rigid contact lens is measured as the phantom calibration. The results are illustrated as following. R_p is the curvature of the episurface of the contact lens; R_a is the endosurface of the contact lens and P_t is the total optical power of the contact lens. The relative measurement error of the top surface is 0.5% and 0.4% of the 3D refraction corrected endosurface. The error of the total optical power is 0.18D and it is within quarter Diopters.

Table 2: Measurement results of a phantom rigid contact lens

	R_p (mm)	R_a (mm)	P_t (D)
Contact lens Nominal values	7.6	7.99	-3.00
SDOCT Result-1	7.63	8.05	-3.21
SDOCT Result-2	7.64	8.06	-3.15
SDOCT Result-3	7.61	8.01	-3.08
Mean	7.63 ± 0.02	8.04 ± 0.03	-3.18 ± 0.04

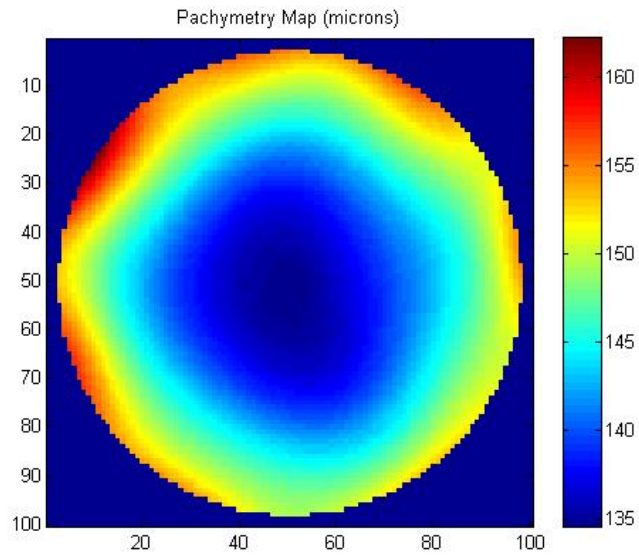


Figure 51: Thickness map of RGP contact lens phantom

Central value is given in above table. The thickness mapping is obtained along the epithelial surface normal vector. The measurement result of the central thickness and base curvature are very close to the nominal value which is from vendor. The vendor only provides a point measurement at the apex which is $130 \pm 20 \mu\text{m}$. There is no reference for whole thickness map from the product vendor. The central thickness obtained by SDOCT is $136.2 \pm 1.6 \mu\text{m}$.

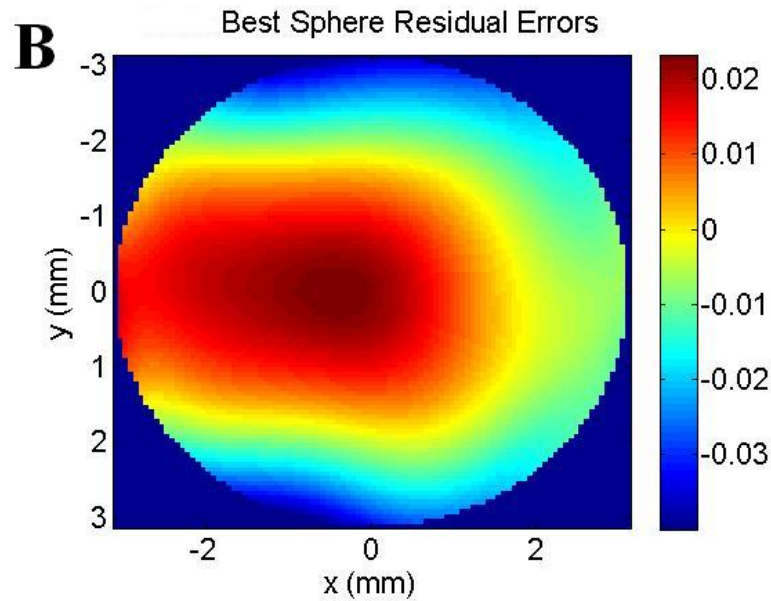


Figure 52: Best spherical fitting residual errors after 3D refraction correction
Residual errors of the endosurface are very limited. This surface is the base surface of the phantom contact lens. The color bar unit is in mm.

4.6 *In vivo* Results

4.6.1 Radial Scanning Mode

Why do we choose radial scanning mode? Comparing with raster scanning mode, radial scanning pattern does not have image quality degradation issue. It means we can get clear corneal image with good brightness and contrast. The following image illustrates corneal imaging captured by radial scanning. The corneal 3D volume is obtained using 50 B-scan (1000A-scan/B-scan) with radial scanning mode in 2.5 seconds. The following figure shows an *in vivo* corneal image. The imaging protocol ensures that the OCT image is saturated around the apex position. There is a circular red fixation

target in the SDOCT system. The imaging position complies with the configurations which are marked for the target calibration position.

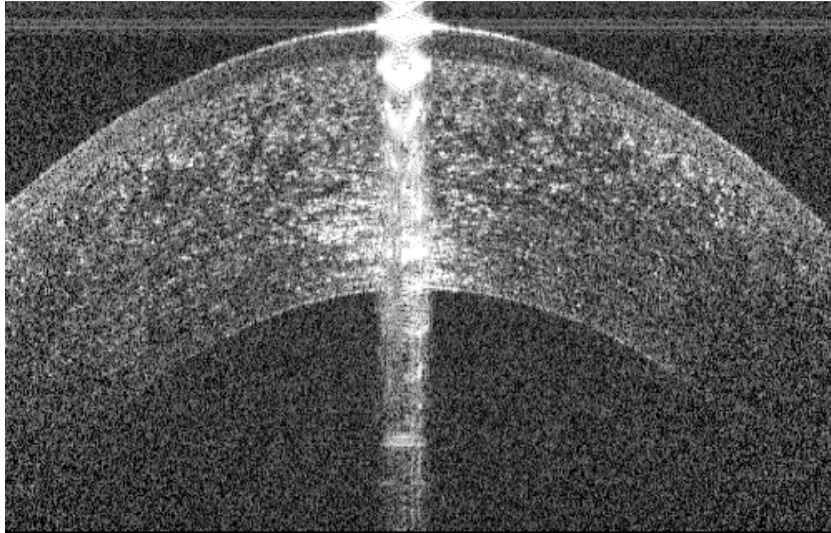


**Figure 53: *In vivo* corneal image with radial scanning range of 6mm
The B-scan images captured for each radial scanning must be saturated at apex**

The thickness map of an in vivo anterior segment imaging is illustrated as following:

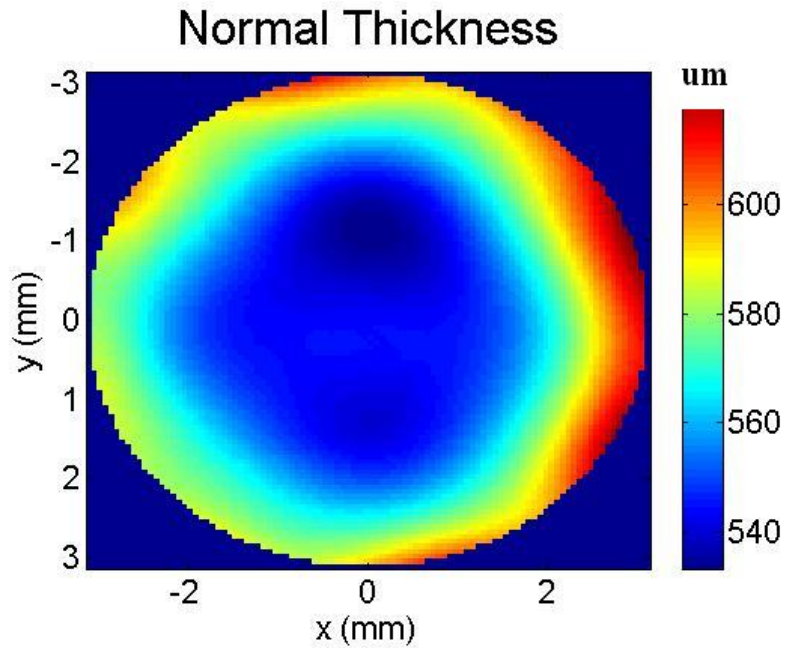


Figure 54: Pachymetry mapping of an *in vivo* cornea
 The two blue areas reflect that there is astigmatism aberration error in the cornea, which is confirmed by the Pentacam device.

To date, there have been 11 people enrolled for a total of 22 eyes. From this population, a subset of 20 eyes from 11 subjects has been completely analyzed. The patient data are as following:

Table 3: Patient study---Curvature of epithelial surface (*units in mm*)

Subject	OCT	Topography	Pentacam
1	7.84	8.12	8.06
2	7.65	7.87	7.92
3	7.53	7.54	7.56

Table--- (Continued)

4	7.33	7.56	7.58
5	7.41	7.43	7.54
6	7.86	8.35	8.35
7	8.02	8.28	8.32
8	8.10	8.29	8.28
9	7.85	8.29	8.32
10	7.20	7.94	7.94
11	7.69	7.87	7.98
12	7.64	7.78	7.81
13	7.59	7.74	7.79
14	7.28	7.74	7.72
15	8.00	7.89	7.75
16	7.42	7.57	7.69
17	7.53	7.57	7.63
18	7.49	7.78	7.76
19	7.56	7.67	7.71
20	8.36	8.32	8.40

Table 4: Patient study---Curvature of endothelial surface (*units in mm*)

Subject	OCT	Topography	Pentacam
1	6.24	NA	6.72
2	6.20	NA	6.54
3	6.20	NA	6.21
4	5.95	NA	6.31
5	6.12	NA	6.22
6	6.57	NA	6.9
7	6.65	NA	6.88
8	6.56	NA	6.91
9	6.55	NA	6.96
10	5.91	NA	6.43
11	6.18	NA	6.52
12	6.20	NA	6.42
13	6.27	NA	6.41
14	6.01	NA	6.4
15	6.64	NA	6.39
16	6.05	NA	6.31

Table--- (Continued)

17	6.11	NA	6.18
18	6.08	NA	6.45
19	6.21	NA	6.36
20	7.5	NA	6.98

Table 5: Patient study---Overall corneal power (*units in Diopters*)

Subject	OCT	Topography	Pentacam
1	41.2	42	42.0
2	42.4	43	42.2
3	43.2	44.6	44.4
4	44.2	44.7	44.8
5	43.9	45.2	44.9
6	41.5	40.5	40.5
7	40.6	40.7	40.5
8	40.0	40.7	40.6
9	41.5	40.6	40.5
10	44.9	42.6	42.3
11	42.1	42.7	42.2

Table--- (Continued)

12	42.5	43.5	43.3
13	42.9	43.4	43.2
14	44.6	43.6	43.3
15	40.7	43.0	42.8
16	43.8	44.7	43.6
17	43.1	45.2	43.9
18	43.3	43.7	43.23
19	43.0	43.9	43.97
20	39.5	40.6	40.17

Since it utilizes Placido ring project, Topography can only measure top surface and can not measure the endosurface of the cornea. It assumes that the posterior cornea has a fixed relationship with that of the front surface. And it always uses an equivalent refractive index 1.3375 to infer the whole corneal power. It inevitably introduces some systematic errors.

The mean difference between OCT and topography for 20 eyes to date was 0.52 D \pm 1.10 D. The data is represented in the Bland-Altman plot below:

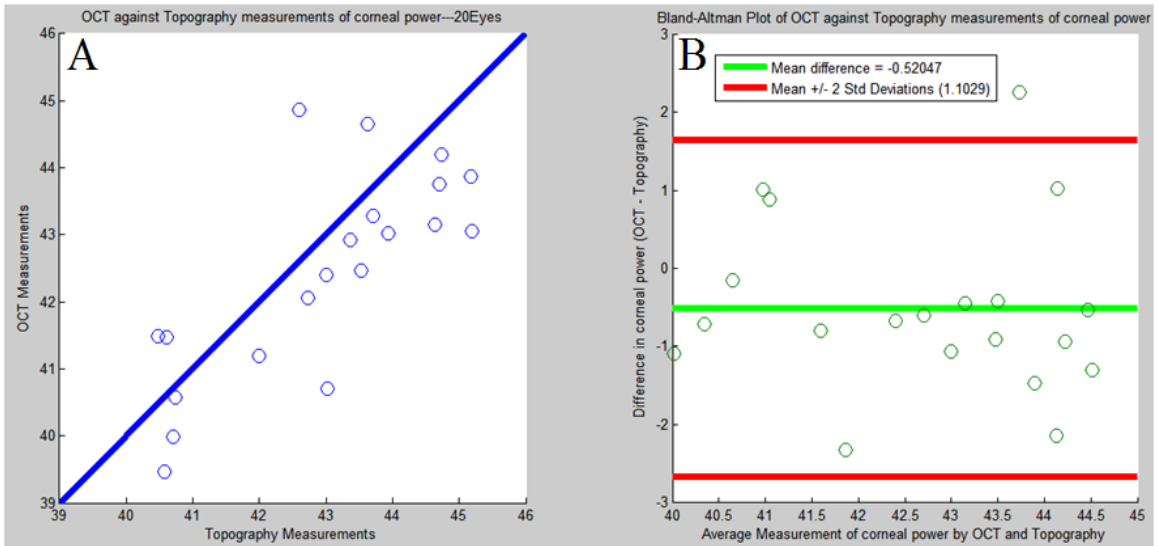


Figure 55: Comparison between OCT and topography

A: OCT against topography measurement corneal power B: Bland-Altman plot of OCT against topography measurement of corneal power. The mean difference is 0.52D and the standard deviation of the difference is 1.1D. Units are in Diopters.

The mean difference between OCT and Scheimpflug photography for 20 eyes to date was $0.19 \text{ D} \pm 1.05 \text{ D}$. The data is represented in the Bland-Altman plot below:

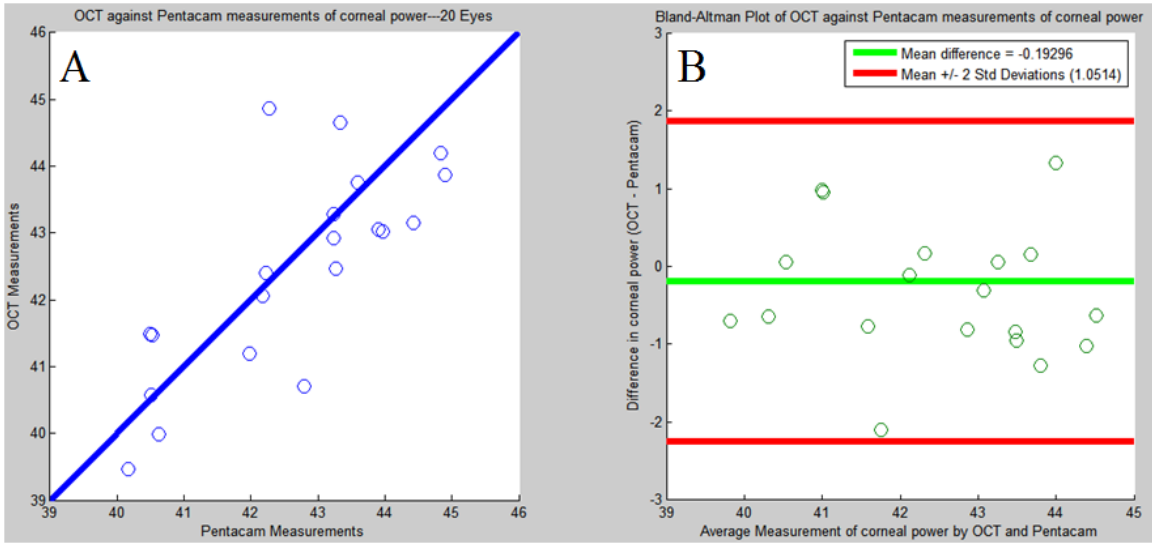


Figure 56: Comparison between OCT and Pentacam

A: OCT against Pentacam measurement of corneal power. B: Bland-Altman plot of OCT against Pentacam measurement of corneal power. The mean difference is 0.19D and the standards deviation of the difference is 1.05D. Units are in Diopters.

The mean difference between Topography and Scheimpflug photography for the enrolled subjects to date was $0.33 \text{ D} \pm 0.37 \text{ D}$. The data is represented in the Bland-Altman plot below:

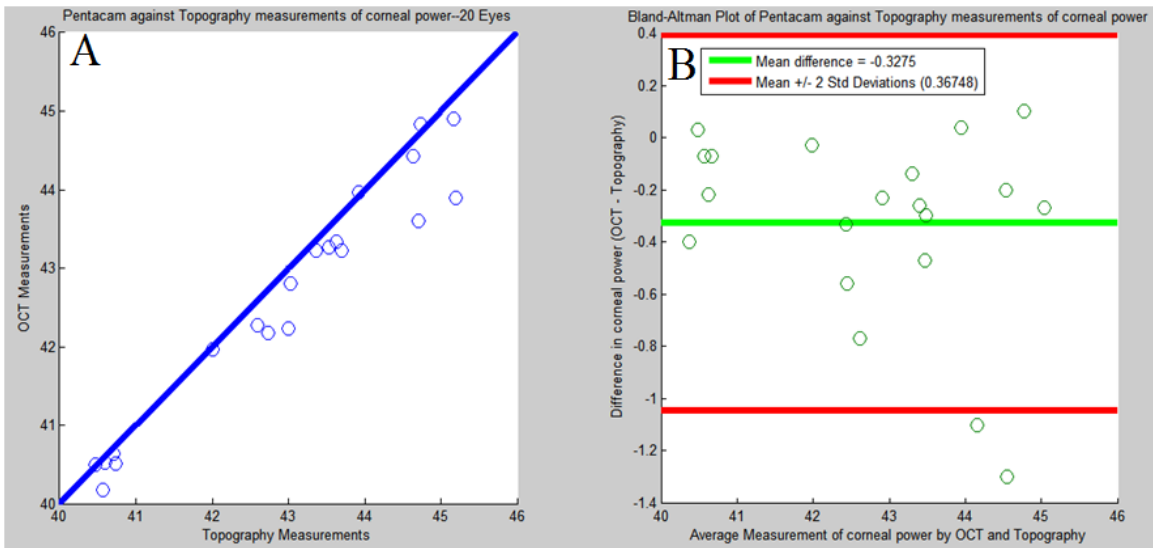


Figure 57: Comparison between Topography and Pentacam

A: Topography against Pentacam measurement of corneal power. B: Bland-Altman plot of Topography against Pentacam measurement of corneal power. There is a constant offset 0.33D between those two instruments. The standard deviation of the differences is 0.37D. Units are in Diopters.

The following figure summarized the performance of the SDOCT, Topography and Pentacam.

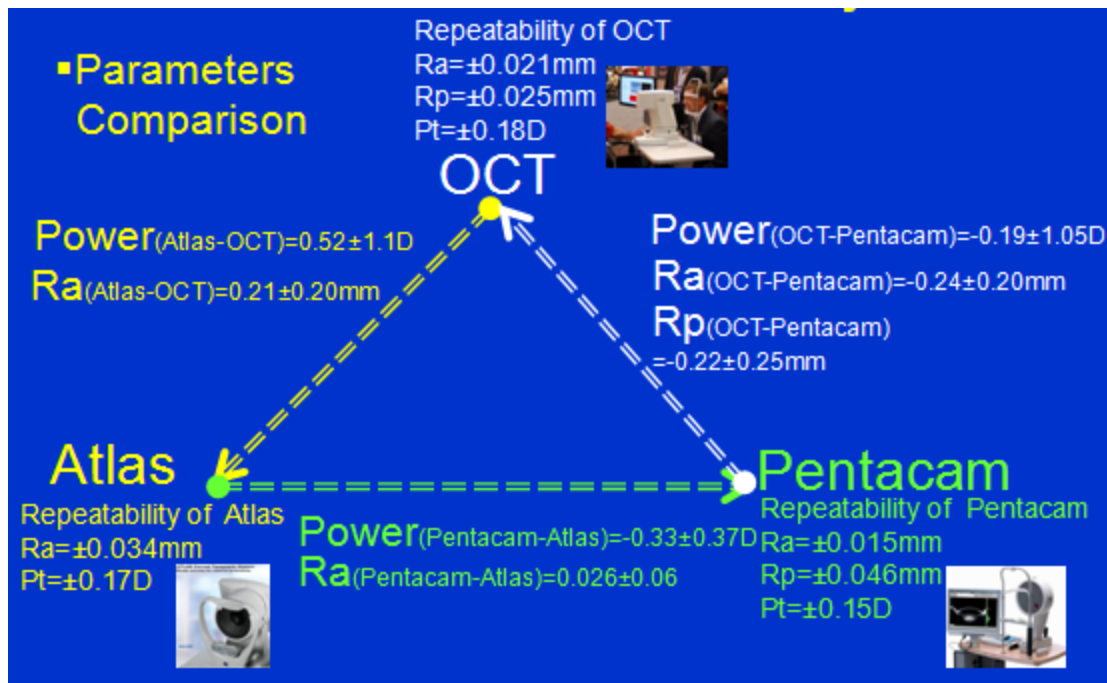


Figure 58: Performance summary of SDOCT, Pentacam and Topography
 (Notes: The figures of Atlas and Pentacam are downloaded from each company's home page.)

While we can accurately extract physical parameters and power of a contact lens phantom from SDOCT images with correction for non-telecentric scanning and 3D refraction correction, central corneal power as measured by SDOCT currently does not agree well with other imaging instruments as measured by Bland-Altman plot. Possible differences and errors include the use of an artificial keratometric refractive index by the other devices, acquisition artifacts (patient motion, decentration of the radial scan from the corneal apex), and segmentation errors. More conclusive statements can be made as

the enrollment of subjects eventually surpasses the minimum sample size needed. The amount of error introduced by bulk motion is described in the following section.

4.6.2 Error Analysis

Sag error analysis

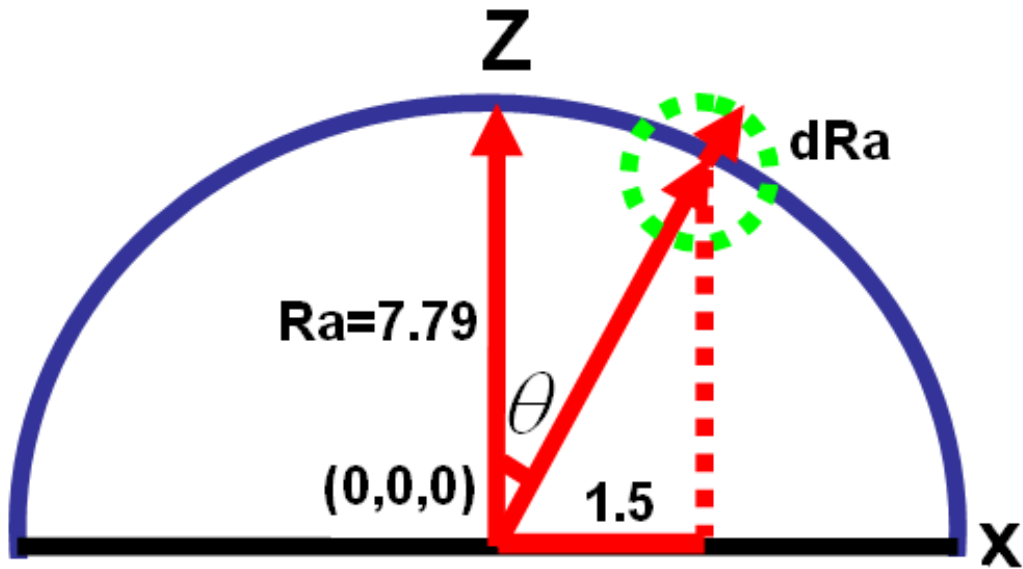


Figure 59: Sag error analysis

Corneal power is defined as the change in refractive index over the radius of curvature of the cornea:

$$K = \frac{n_k - n_0}{R_a} \quad (29)$$

Here $n_k = 1.3375$, $n_0 = 1.0$, $R_a = 7.79$ mm[74]. The change in corneal power as a function of the change in radius of curvature (error) can then be describe as,

$$dK = -\frac{n_k - n_0}{R_a^2} dR_a \quad (30)$$

If we let $dK = 0.25D$ which is the acceptable clinical standard, then we get

$$dR_a = 45 \mu\text{m} \quad (31)$$

Since

$$dR_a = \frac{1}{R_a} (zdz + rdr) \quad (32)$$

Where dz represents the axial movement and $dr = d\sqrt{x^2 + y^2}$ represents the lateral movement. Corneal power fitting typically occurs over the central 3mm (diameter). An extreme lateral position of $r = 1.5\text{mm}$ can then be used to examine changes resulting from axial or transverse motion at that position. When $dr = 0$, then

$$dz = 46 \mu\text{m} \quad (33)$$

When $dz = 0$, then

$$dr = 233 \mu\text{m} \quad (34)$$

The above results show that the axial bulk motion must be less than $46\mu\text{m}$ and the lateral bulk motion must be less than $233 \mu\text{m}$ if we want to obtain an accuracy of at least $0.25D$. Actually the axial bulk motion is much stronger than $46\mu\text{m}$. With an axial change of around $150\mu\text{m}$, the corresponding error in corneal power is $0.82D$. The axial change required to produce a $1.1D$ change is $200\mu\text{m}$. The potential solution is full field imaging or ultra high speed imaging; otherwise the measurement error will be large.

Calibration error analysis

Do calibration errors cause the problem if we want to obtain an accuracy of at least 0.25D? To answer this question, we go through the same procedure as sag error analysis. The only difference is that the setting scanning range is 6mm instead of 3mm which is illustrated in the following figure.

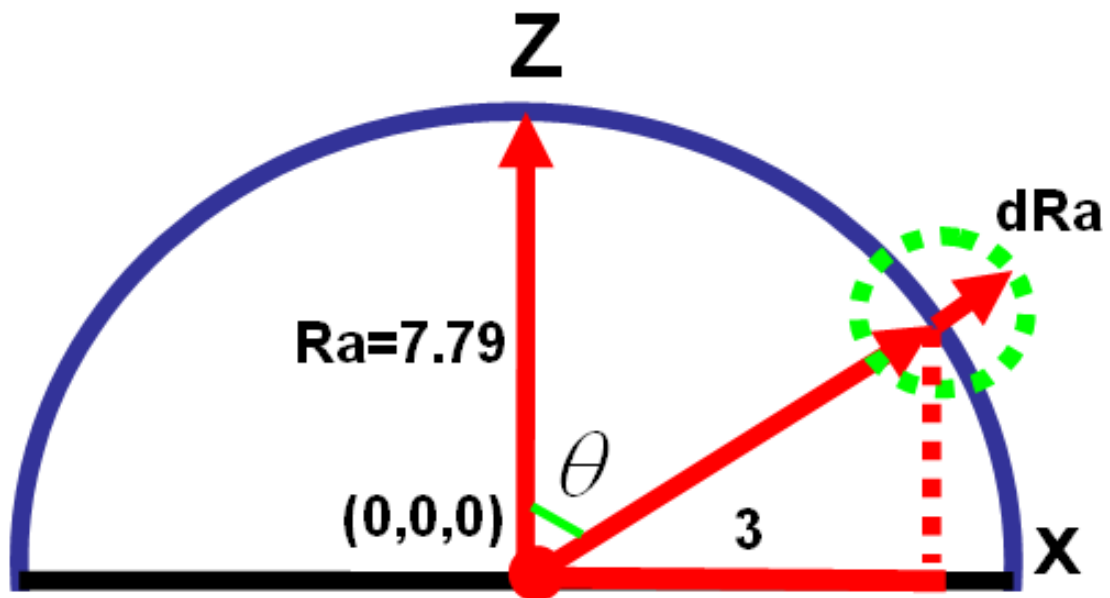


Figure 60: Calibration error analysis

An extreme lateral position of $r = 3.0mm$ can then be used to examine changes resulting from axial or lateral calibration errors. When $dr = 0$, then

$$dz = 49 \mu m \quad (35)$$

When $dz = 0$, then

$$dr = 117\mu m \quad (36)$$

The above results show that the axial calibration error must be less than $49\mu m$ and the lateral calibration error must be less than $117\mu m$ if we want to obtain an accuracy of at least 0.25D. In the lateral calibration, the result is $6.125 \pm 0.009\text{ mm}$. So the 3 standard deviation (3σ) is $28.47\mu m$, which is much less than $117\mu m$. Similarly the maximum imaging depth is $4.700 \pm 0.016\text{mm}$ and its 3 standard deviation is $48\mu m$ which is less than $49\mu m$. According to normal Gaussian probability distribution, the $\pm 3\sigma$ will occupy 99.73% of the overall area. The conclusion is that our calibration is accurate enough to ensure 99.73% measurement results within 0.25 Diopters.

4.6.3 Raster Scanning Mode

I have also migrated above 3D refraction correction algorithm to the raster scanning pattern. Raster scanning pattern does not request resembling, however the OCT signal will be severely degraded when the location of B-scan image is more than 2.5mm away from apex. As a result, it will have an influence over the measurement accuracy. The testing data was taken from a 3 by 3 swept source system which was developed by Marinko V. Sarunic. The central wavelength of the system is 1.3 micrometers and it provides a swept rate of 6.7 KHz. The axial resolution of the OCT system is 9 micrometers in air[72]. The following image shows B-scan image after 3D refraction correction.

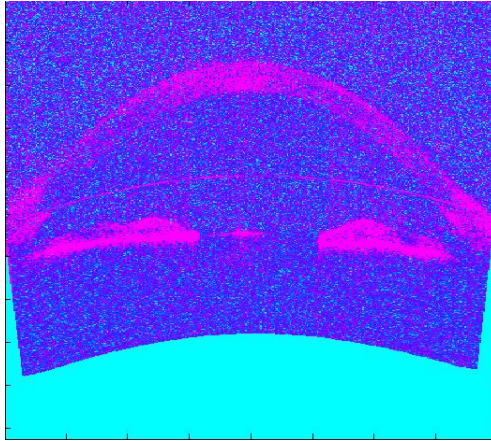


Figure 61: 3D refraction correction

Both the side edge and bottom edge become into a curved shape after refraction correction. The data is from a 3 by 3 swept source OCT (SSOCT) with its central wavelength $1.3\mu\text{m}$.

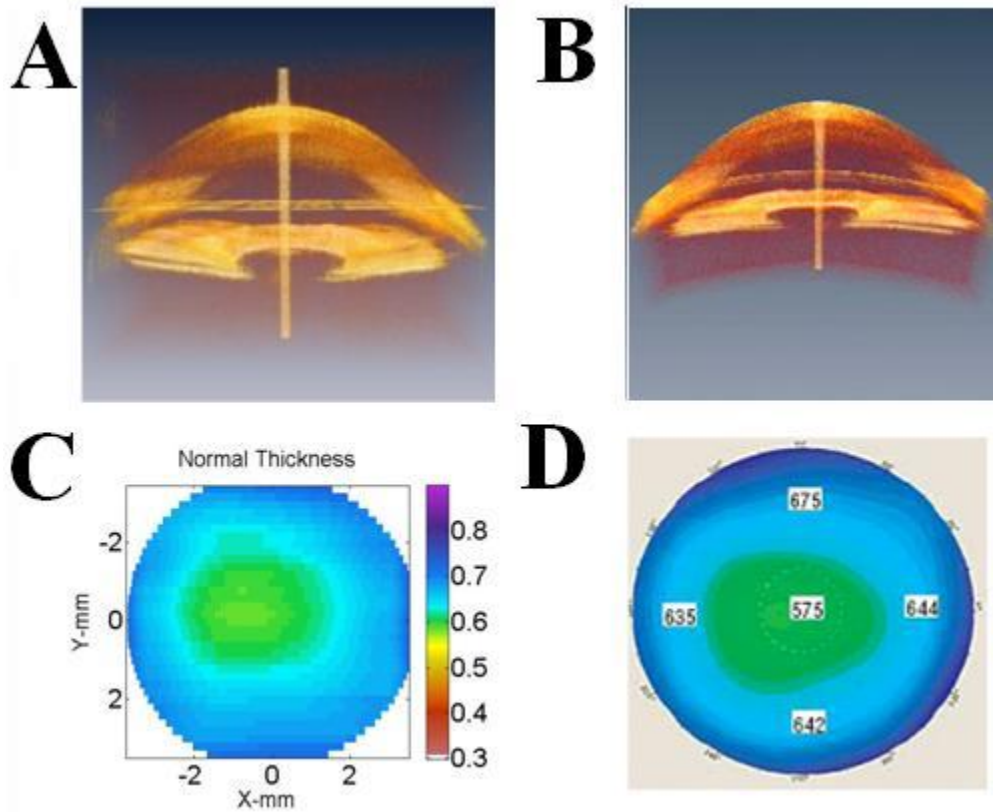


Figure 62: Three dimensional refraction correction and corneal thickness mapping after refraction correction processing

A: 3D rendering of unprocessed corneal volumetric dataset composed of 512x400x60 voxels spanning 7.5x12x12 mm (axial x lateral x elevation), acquired in 4.5 seconds. **B:** 3D refraction corrected dataset. **C:** Corneal thickness map obtained from 3D refraction corrected data. **D:** Corneal thickness map of the same patient as recorded by an Oculus Pentacam® instrument. Both corneal thickness maps were smoothed by a 2D low-pass convolution filter.

Above figure illustrates preliminary results obtained by applying this procedure to a volumetric dataset obtained using a previously described swept-source OCT system with sufficient imaging depth to image the entire anterior segment. Figure 62(A) illustrates the corneal volumetric dataset before refraction correction. Note that

saturation artifacts from the data acquisition are manifested as a bright vertical stripe through the corneal apex and also a horizontal artifactual band at approximately the level of the corneo-scleral interface. Following 3D refraction dewarping (Figure 62 (B)), the axial dimension is contracted, leading to a more realistic depiction of the corneal shape and anterior angle. In Figure 62 (C) and (D), the refraction-corrected corneal thickness map is compared to the result in the same patient measured using an Oculus Pentacam® instrument, and found to correspond within 8 μ m.

4.7 Summary

In conclusion, we describe an algorithm for quantitative image correction and clinical parameter computation which is generally applicable for any OCT sample containing refracting interfaces and regions of different refractive indices. The algorithm is particularly suitable for quantitative correction of 3D OCT images of the cornea and anterior segment of the eye. Two specific implementations for two different scanning patterns are introduced for corneal imaging. Zernike 3D interpolation is proposed to represent the corneal surfaces (epithelium, uncorrected endothelium, and refraction corrected surfaces). This interpolation method makes it possible for the implementation of a recursive half searching algorithm (RHSA) to measure the corneal thicknesses and map them in an en face clinical view. 3D corneal volumetric refraction correction provides the foundation for generating further clinical parameters. These include known

clinical ones such as wavefront analysis, asphericity, refractive curvature maps, and best fit sphere float maps as well as novel ones such as angle magnitude maps. 3D refraction correction and the accurate representation of ocular structures it creates provide an important tool in the visualization and management of ocular disease. Full field single shot or ultra high speed scanning is a must to get accurate result.

5 Future Works in Spectral Domain Optical Coherence Tomography

5.1 From High Speed SDOCT to Ultra High Speed SDOCT

There are mainly three factors which influence the imaging speed of SDOCT, which are laser tunable speed, Fast Fourier transform (FFT) and detector speed. There are two solutions for tunable laser, which are FDML[3] (a sweep rate of 290 kHz) and optical demultiplexers imaging (60,000,000 lines/s)[2]. As to the Fast Fourier transform, current high speed SDOCT is based on CPU to calculate the Fast Fourier transform. The typical library is Intel Math Kernel library and FFTW. GPU is another alternative choice for FFT and it is generally 6 times faster than Intel library. The only problem with GPU is that it only supports single float point computation. The possible solution for real time processing could be optical computation. One of the potential problems is that the coherence property of the source could be an obstacle.

5.2 Fiber Based Polarization Sensitive OCT

The continue project for PSOCT should be to develop fiber based PSOCT for clinical application or free space based but with fewer input polarization states[44, 46]. The direction application is to segment and measure the thickness of optic nerve fiber layer. The combined estimation and correlation of the thickness mapping of ONFL and blood flow in the retina should be a powerful tool for glaucoma detection. To segment

RPE from drusen, the degree of polarization of the retina should be correctly mapped. There are two methods to obtain the degree of depolarization (DOP) of the retinal layers, which are Stoke vectors method and the multiplication of the standard deviation of the retardance and the fast axis orientation in the single spectrometer based SDOCT. The RPE is segmented based on the DOP. For Stoke vectors measurement, it looks like that we have to use two channels or single channel with a carrier frequency to encode another orthogonal polarization state.

5.3 Brewster Angle to Improve Anterior Segment Imaging

To improve the image intensity fall off caused by the epithelium surface reflection for big scanning range, we here employed radial scanning pattern. However the degradation of image quality is still there when the scanning range is higher than 6mm.

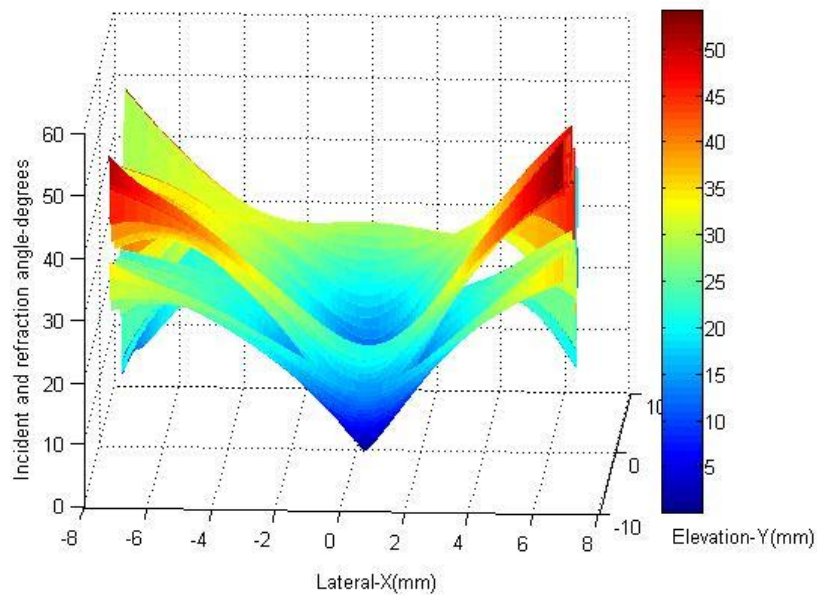


Figure 63: The incidence and refraction angle of the epithelium surface of an in vivo cornea

The top 3D surface is the incidence angle and second 3D surface is the refraction angle. The incident angle is around 40° which are close to the Brewster angle.

In this regard, it is useful to point out that Brewster's angle for the cornea is $\text{Arc tan}(n_c / n_{air}) \approx 54^\circ$. Where n_c is the refractive index of cornea (1.385) and n_{air} is the refractive index of air (1.0). When the diameter of the scanning range is bigger than about 6 mm, the majority of the incident light will be obliquely reflected by the epithelial surface and thus lost if the incident polarization state is random. Thus, OCT images of the cornea in that region are very weak. However, the incident angle is quite close to Brewster's angle when the scanning range is bigger than 8 mm. As a result, part of the s-polarized light perpendicular to the incident plane will be reflected, but all the p-

polarized light within the incident plane will be transmitted with no loss. To enhance brightness of OCT images of the cornea for large scan widths, p-polarized light is thus preferable, although the cornea has strong birefringence effects which will change the polarization states of the transmitted p-polarization light into elliptical states.

5.4 Cellular Corneal Imaging Based on Light Scattering

OCT's lateral resolution is around 25 microns and its axial resolution is 5 microns with 3mm imaging depth. The lateral resolution of optical coherence microscopy (OCM) can be around 2 micron if a very big numerical aperture is used. However OCM's depth of field is very limited. To simultaneously get both high resolutions in lateral and axial dimension, I suggest combining light scattering technique with OCT to get cellular imaging in cornea. There are two reasons why it works for cellular corneal imaging[37, 80, 81]:

(A) There is no blood vessel in the cornea; hence there are no hemoglobin negative effects on the Mie scattering pattern.

(B) Corneal image is different from the retinal imaging. The imaging optics in the retina limits the collection range of scattering angles in the retina. However it is not a problem for cornea. The outside of the cornea is air; we can design an optical system to collect the scattering light with a range of 180° .

5.5 Estimation of the Wave Aberration of Each Component in the Cornea

The advantage of OCT over other technologies is that OCT has a very high sampling density which will help clinicians to accurately measure several aberrations of cornea. Optical aberration, such as astigmatism and spherical error, in the human eye plays an important role in determining the physical limit on spatial vision. Combining with Hartmann-Shack (H-S) sensor, OCT allows us to measure the relative aberration contribution of anterior segment, posterior segment and crystalline lens[82] individually. Those aberrations will determine the quality of image on the retina. Hence the future direction is to estimate the wave aberration of the crystalline lens using OCT and 3D refraction correction algorithm. H-S sensor[83, 84] gives the overall aberration and OCT provides that of cornea and crystalline lens. After subtraction, we can infer the aberration contribution of the rest component in the retinal optical imaging system.

References

1. A. F. Fercher, C. K. Hitzenberger, G. Kamp, and S. Y. El-Zaiat, "Measurement of intraocular distances by backscattering spectral interferometry," *Opt. Commun.* **17**, 6 (1995).
2. D. Choi, H. Hiro-Oka, H. Furukawa, R. Yoshimura, M. Nakanishi, K. Shimizu, and K. Ohbayashi, "Fourier domain optical coherence tomography using optical demultiplexers imaging at 60,000,000 lines/s," *Opt.Lett.* **33**, 3 (2008).
3. R. Huber, D. C. Adler, V. J. Srinivasan, and J. G. Fujimoto, "Fourier domain mode locking at 1050 nm for ultra-high-speed optical coherence tomography of the human retina at 236,000 axial scans per second," *Opt.Lett.* **32**, 3 (2007).
4. R. Zawadzki, S. Jones, S. Olivier, M. Zhao, B. Bower, J. Izatt, S. Choi, S. Laut, and J. Werner, "Adaptive-optics optical coherence tomography for high-resolution and high-speed 3D retinal in vivo imaging," *Opt.Express* **13**, 15 (2005).
5. J. M. Schmitt and A. K. ttel, "Model of optical coherence tomography of heterogeneous tissue," *J. Opt. Soc. Am. A* **14**, 12 (1997).
6. A. F. Fercher, W. Drexler, C. K. Hitzenberger, and T. Lasser, "Optical coherence tomography - principles and applications," *Rep. Prog. Phys.* **66**, 66 (2003).
7. J. A. Izatt, M. D. Kulkarni, H.-W. Wang, K. Kobayashi, and M. V. Sivak, Jr., "Optical coherence tomography and microscopy in gastrointestinal tissues," *IEEE J. Sel. Top. Quantum Electron* **2**, 12 (1996).
8. M. Wojtkowski, V. Srinivasan, T. Ko, J. Fujimoto, A. Kowalczyk, and J. Duker, "Ultrahigh-resolution, high-speed, Fourier domain optical coherence tomography and methods for dispersion compensation," *Opt. Express* **12**(2004).
9. G. Ha^uusler and M. W. Lindner, "Coherence Radar and Spectral Radar—New Tools for Dermatological Diagnosis," *J. Biomed. Opt.* **3**, 11 (1998).
10. M. A. Choma, M. V. Sarunic, C. Yang, and J. A. Izatt, "Sensitivity advantage of swept source and Fourier domain optical coherence tomography," *Opt.Express* **11**, 7 (2003).

11. S. H. Yun, G. J. Tearney, J. F. d. Boer, N. Iftimia, and B. E. Bouma, "High-speed optical frequency-domain imaging," *Opt.Express* **11**, 11 (2003).
12. R. Leitgeb, C. K. Hitzenberger, and A. F. Fercher, "Performance of fourier domain vs. time domain optical coherence tomography," *Opt.Express* **11**, 6 (2003).
13. E. D. P. R. Group, "Prevalence of Open-Angle Glaucoma Among Adults in the United States," *Arch Ophthalmol.* **122**, 7 (2004).
14. K. A. Townsend, G. Wollstein, and J. S. Schuman, "Imaging of the retinal nerve fibre layer for glaucoma," *Br. J. Ophthalmol.* **93**, 5 (2009).
15. N. J. Kemp, H. N. Zaatari, J. Park, H. G. R. III, and T. E. Milner, "Form-biattenuance in fibrous tissues measured with polarization-sensitive optical coherence tomography (PS-OCT)," *Opt.Express* **13**(2005).
16. Z. Q, "Retinal scanning laser polarimetry and methods to compensate for corneal birefringence," *Bull. Soc. belge Ophtalmol.* **302**, 18 (2006).
17. D. Huang, E. A. Swanson, C. P. Lin, J. S. Schuman, W. G. Stinson, W. Chang, M. R. Hee, T. Flotte, K. Gregory, C. A. Puliafito, and J. G. Fujimoto, "Optical coherence tomography," *Science* **254**, 4 (1991).
18. J. F. d. Boer, B. Cense, B. H. Park, M. C. Pierce, G. J. Tearney, and B. E. Bouma, "Improved signal-to-noise ratio in spectral-domain compared with time-domain optical coherence tomography," *Opt.Lett.* **28**, 3 (2003).
19. S. H. Yun, G. J. Tearney, B. E. Bouma, B. H. Park, and J. F. d. Boer, "High-speed spectral-domain optical coherence tomography at 1.3 μm wavelength," *Opt.Express* **11**, 7 (2003).
20. N. Nassif, B. Cense, B. H. Park, S. H. Yun, T. C. Chen, B. E. Bouma, G. J. Tearney, and J. F. d. Boer, "in vivo human retinal imaging by ultrahigh-speed spectral domain optical coherence tomography," *Opt.Lett.* **29**, 3 (2004).
21. A. JL, M.O., O. D, P.-S. JJ, A. A, A. MJ, G. MJ, and d. L. GC, "Ten-Year Follow-Up of Laser In-Situ Keratomileusis for Myopia up to -10 Diopters," *Am. J. Ophthal.* **145**, 9 (2008).

22. A. S. o. C. a. R. Surgery, "ASCRS to Participate In and Co-Fund Study on Post-LASIK Quality of Life with U.S. Food and Drug Administration [press release].," Available from: http://www.ascrs.org/press_releases/ASCRS-TO-PARTICIPATE-IN-AND-CO-FUND-STUDY-ON-POST-LASIK-QUALITY-OF-LIFE-WITH-US-FOOD-AND-DRUG-ADMINISTRATION.cfm. (2008).
23. M. C. Cairns G, "Orbscan computerized topography: attributes, applications, and limitations," *J.Cataract.Refract.Surg* **31**, 16 (2005).
24. E. Donnenfeld, "Discussion of article by Seitz B, Torres F, Langenbucher A, et al.," *Ophthalmology* **108**(2001).
25. R. SN, R. T, M. PA, and E. RJ, "Role of Orbscan II in Screening Keratoconus Suspects before Refractive Corneal Surgery," *Ophthalmology* **109**, 5 (2002).
26. M. Tang, Y. Li, M. Avila, and D. Huang, "Measuring total corneal power before and after laser in situ keratomileusis with high-speed optical coherence tomography," *J Cataract Refract Surg* **32**, 8 (2006).
27. B. A. Bower, M. Zhao, R. J. Zawadzki, and J. A. Izatt, "Real-time spectral domain Doppler optical coherence tomography and investigation of human retinal vessel autoregulation," *J.Biomed. Opt.* **12**, 8 (2007).
28. M. Zhao, Y. Tao, and J. A. Izatt, "High-speed fiber-based polarization sensitive retinal SDOCT," *Invest. Ophthalmol. Vis. Sci. E-Abstract* **48**(2007).
29. R. Zawadzki, J. Steven, O. Scot, M. Zhao, B. Bradley, J. A. Izatt, S. Choi, S. Laut, and J. Werner, "Adaptive-optics optical coherence tomography for high-resolution and high-speed 3D retinal in vivo imaging," *Opt.Express* **13**, 15 (2005).
30. B. A. Bower, M. Zhao, A. Chu, R. J. Zawadzki, C. Toth, and J. A. Izatt, "Rapid volumetric imaging of the human retina in vivo using a low-cost, spectral domain optical coherence tomography system," *Invest. Ophthalmol. Vis. Sci.E-Abstract* **46**(2005).
31. B. A. Bower, M. Zhao, Y. Wang, A. Chu, R. J. Zawadzki, M. V. Sarunic, and J. A. Izatt, "Rapid volumetric imaging of the human retina in vivo using a low-cost spectral domain optical coherence tomography system," *Proc. SPIE* **5690**, 6 (2005).

32. M. Zhao, H. C. Hendargo, and J. A. Izatt, "Synthetic wavelength-based phase unwrapping in Fourier domain optical coherence tomography," U.S. provisional patent application, Duke File No.3114 (2008).
33. H. C. Hendargo, M. Zhao, N. Shepherd, and J. A. Izatt, "Synthetic wavelength based phase unwrapping in spectral domain optical coherence tomography," *Opt.Express* **17**, 13 (2009).
34. Y. Tao, M. Zhao, and J. A. Izatt, "High-speed complex conjugate resolved retinal spectral domain optical coherence tomography using sinusoidal phase modulation," *Opt.Lett.* **32**, 3 (2007).
35. M. R. Hee, D. Huang, E. A. Swanson, and J. G. Fujimoto, "Polarization-sensitive low-coherence reflectometer for birefringence characterization and ranging," *J. Opt. Soc. Am. B* **9**, 903 (1992).
36. J. F. d. Boer, S. M. Srinivas, A. Malekafzali, Z. Chen, and J. S. Nelson, "Imaging thermally damaged tissue by polarization sensitive optical coherence tomography," *Opt.Express* **3**, 212 (1998).
37. J. W. Pyhtila, J. D. Boyer, K. J. Chalut, and A. Wax, "Fourier-domain angle-resolved low coherence interferometry through an endoscopic fiber bundle for light-scattering spectroscopy," *Opt.Lett.* **3**, 3 (2006).
38. B. Cense, T. Chen, H. Park, M. Pierce, and J. de Boer, "Thickness and Birefringence of Healthy Retinal Nerve Fiber Layer Tissue Measured with Polarization-Sensitive Optical Coherence Tomography," *Invest. Ophthalmol. Vis. Sci.* **45**, 2606 (2004).
39. M. Pircher, E. Goetzinger, R. Leitgeb, and C. K. Hitzenberger, "Transversal phase resolved polarization sensitive optical coherence tomography," *Med. Biol.* **49**, 4 (2004).
40. M. Pircher, E. Götzinger, R. Leitgeb, H. Sattmann, O. Findl, and C. Hitzenberger, "Imaging of polarization properties of human retina in vivo with phase resolved transversal PS-OCT," *Opt. Express* **12**(2004).
41. E. Götzinger, M. Pircher, and C. K. Hitzenberger, "High speed spectral domain polarization sensitive optical coherence tomography of the human retina," *Opt.Express* **13**, 10217 (2005).

42. E. Götzinger, M. Pircher, R. A. Leitgeb, and C. K. Hitzenberger, "High speed full range complex spectral domain optical coherence tomography," *Opt.Express* **13**, 12 (2005).
43. M. Yamanari, S. Makita, V. D. Madjarova, T. Yatagai, and Y. Yasuno, "Fiber-based polarization-sensitive Fourier domain optical coherence tomography using B-scan-oriented polarization modulation method," *Opt. Express* **14**, 6502 (2006).
44. M. Yamanari, Y. Lim, S. Makita, and Y. Yasuno, "Visualization of phase retardation of deep posterior eye by polarization-sensitive swept-source optical coherence tomography with 1- μ m probe," *Opt.Express* **17**, 12 (2009).
45. C. L. Nordgaard, K. M. Berg, R. J. Kapphahn, C. Reilly, X. Feng, T. W. Olsen, and D. A. Ferrington, "Proteomics of the Retinal Pigment Epithelium Reveals Altered Protein Expression at Progressive Stages of Age-Related Macular Degeneration," *Invest. Ophthalmol. Vis. Sci.* **47**, 8 (2006).
46. E. Götzinger, M. Pircher, W. Geitzenauer, C. Ahlers, B. Baumann, S. Michels, U. Schmidt-Erfurth, and C. K. Hitzenberger, "Retinal pigment epithelium segmentation by polarization sensitive optical coherence tomography," *Opt.Express* **16**, 13 (2008).
47. M. Zhao and J. A. Izatt, "Single-camera sequential-scan-based polarization-sensitive SDOCT for retinal imaging," *Opt. Lett.* **34**, 3 (2009).
48. A. N. Kuo, M. Zhao, and J. A. Izatt, "Corneal aberration measurement with three-dimensional refraction correction for high-speed spectral domain optical coherence tomography," *Invest. Ophthalmol. Vis. Sci.*E-Abstract (2009).
49. M. Zhao, A. N. Kuo, and J. A. Izatt, "Quantitative 3D image correction and clinical parameter computation in optical coherence tomography " U.S. Provisional patent application No.61/175,170 (2009).
50. R. J. Zawadzki, B. A. Bower, M. Zhao, M. Sarunic, S. Laut, J. S. Werner, and J. A. Izatt, "Exposure time dependence of image quality in high-speed retinal in vivo Fourier domain OCT," *Proc. SPIE* **5688**, 8 (2005).
51. R. J. Zawadzki, S. Choi, S. Laut, J. S. Werner, S. M. Jones, S. S. Olivier, M. Zhao, B. A. Bower, and J. A. Izatt, "Adaptive-optics optical coherence tomography for

- high-resolution and high-speed in vivo retinal imaging," Proc. SPIE **5861**, 8 (2005).
52. B. A. Bower, M. Zhao, and J. A. Izatt, "Investigation of retinal vessel autoregulation using real-time spectral domain Doppler optical coherence tomography," Proc. SPIE **6079**, 4 (2006).
 53. R. J. Zawadzki, S. M. Jones, M. Zhao, S. S. Choi, S. S. Laut, S. S. Olivier, J. A. Izatt, and J. S. Werner, "Adaptive optics-optical coherence tomography for in vivo retinal imaging: effects of spectral bandwidth on image quality," Proc. SPIE **6138**, 9 (2006).
 54. J. W. Goodman and E. G. Rawson, "Statistics of modal noise in fibers: a case of constrained speckle," Opt.Lett. **6**, 3 (1981).
 55. Y. Zhao, Z. Chen, C. Saxer, Qimin Shen, S. Xiang, J. F. d. Boer, and J. S. Nelson, "Doppler standard deviation imaging for clinical monitoring of in vivo human skin blood flow," Opt.Lett. **25**, 3 (2000).
 56. Y. Zhao, Z. Chen, C. Saxer, S. Xiang, J. F. d. Boer, and J. S. Nelson, "Phase-resolved optical coherence tomography and optical Doppler tomography for imaging blood flow in human skin with fast scanning speed and high velocity sensitivity," Opt.Lett. **25**, 3 (2000).
 57. M. Zhao, D. J. Brady, and J. A. Izatt, "Synthesized long coherent wavelengths to improve OCT phase imaging dynamic range," Duke ECE 299 research report, 6 (2006).
 58. Y.-Y. Cheng and J. C. Wyant, "Two-wavelength phase shifting interferometry," Appl.Opt. **23**(1984).
 59. M. G. Ducros, J. F. d. Boer, H. Huang, L. C. Chao, Z. Chen, J.S.Nelson, T.E.Milner, and I. R. H.G., "Polarization sensitive optical coherence tomography of the rabbit eye," IEEE J. Sel. Topics Quantum Electron. **5**, 9 (1999).
 60. C. K. Hitzenger, E. Götzinger, M. Sticker, M. Pircher, and A. F. Fercher, "Measurement and imaging of birefringence and optic axis orientation by phase resolved polarization sensitive optical coherence tomography," Opt. Express **9**, 780 (2001).

61. J. E. Roth, J. A. Kozak, S. Yazdanfar, A. M. Rollins, and J. A. Izatt, "Simplified method for polarization-sensitive optical coherence tomography," *Opt. Lett.* **26**, 1069 (2001).
62. B. Cense, T. C. Chen, B. H. Park, M. C. Pierce, and J. F. d. Boer, "In vivo depth-resolved birefringence measurements of the human retinal nerve fiber layer by polarization-sensitive optical coherence tomography," *Opt.Lett.* **27**, 3 (2002).
63. S. Jiao and L. V.Wang***, "Reply to Comment on "Optical-fiber-based Mueller optical coherence tomography"," *Optics Letters* **29**, 2875 (2004).
64. R. C. Jones, "New calculus for the treatment of optical systems. I. Description and discussion of the calculus," *J. Opt. Soc. Am. A* **31**, 6 (1941).
65. E. Wolf, "Introduction to the theory of coherence and polarization of light," Cambridge Press (2007).
66. N. J. Kemp, J. Park, H. N. Zaatari, H. G. Rylander, and T. E. Milner, "High-sensitivity determination of birefringence in turbid media with enhanced polarization-sensitive optical coherence tomography " *J. Opt. Soc. Am. A* **22**, 552 (2005).
67. M. Dubbelman, V. A. D. P. Sicam, and G. L. V. d. Heijde, "The shape of the anterior and posterior surface of the aging human cornea " *Vision Research* **46**, 9 (2006).
68. O. Antonio Calossi, "Corneal Asphericity and Spherical Aberration," *Journal of Refractive Surgery* **23**(2005).
69. R. C. Lin, M. A. Shure, A. M. Rollins, J. A. Izatt, and D. Huang, "Group index of the human cornea at 1.3-mm wavelength obtained in vitro by optical coherence domain reflectometry," *Opt. Lett.* **29**, 3 (2004).
70. I. Grulkowski, M. Gora, M. Szkulmowski, I. Gorczynska, D. Szlag, S. Marcos, A. Kowalczyk, and M. Wojtkowski, "Anterior segment imaging with Spectral OCT system using a high-speed CMOS camera," *Opt.Express* **17**, 17 (2009).
71. V. Westphal, A. Rollins, S. Radhakrishnan, and J. Izatt, "Correction of geometric and refractive image distortions in optical coherence tomography applying Fermat's principle," *Opt.Express* **10**, 8 (2002).

72. M. V. Sarunic, S. Asrani, and J. A. Izatt, "Imaging the Ocular Anterior Segment With Real-Time, Full-Range Fourier-Domain Optical Coherence Tomography," *Arch Ophthalmol* **126**, 6 (2008).
73. R. J. Zawadzki, C. Leisser, R. Leitgeb, M. Pircher, and A. F. Fercher, "Three-dimensional ophthalmic optical coherence tomography with a refraction correction algorithm," *Proceedings of SPIE-OSA Biomedical Optics* **5140**, 8 (2003).
74. V. A. D. P. Sicam, M. Dubbelman, and R. G. L. v. d. Heijde, "Spherical aberration of the anterior and posterior surfaces of the human cornea," *J. Opt. Soc. Am. A* **23**, 6 (2006).
75. R. J. Noll, "Zernike polynomials and atmospheric turbulence," *J. Opt. Soc. Am.* **66**, 5 (1976).
76. W. Drexler, C. K. Hitzenberger, A. Baumgartner, O. Findl, H. Sattmann, and A. F. Fercher, "Investigation of dispersion effects in ocular media by multiple wavelength partial coherence interferometry," *Exp. Eye Res.* **66**, 9 (1998).
77. B. Rosner, "Fundamental of Biostatistics," Duxbury Thomson Learning, 792 (2000).
78. B. JM and A. DG, "Statistical methods for assessing agreement between two methods of clinical measurement," *Lancet* **i**, 4 (1986).
79. M.Tang, Y.Li, and D.Huang, ".Corneal topography and power measurement with optical coherence tomography," *ARVO E-Abstract*, 2 (2009).
80. J. W. Pyhtila and A. Wax, "Polarization effects on scatterer sizing accuracy analyzed with frequency-domain angle-resolved low-coherence interferometry," *Appl. Opt.* **46**, 7 (2007).
81. T. S. Ralston, D. L. Marks, S. A. Boppart, and P. S. Carney, "Inverse scattering for high-resolution interferometric microscopy," *Optics Letters* **31**, 3 (2006).
82. H. Zhao, "Optical ensemble analysis of intraocular lens performance through a simulated clinical trial with zemax," *Opt.Lett.* **34**, 3 (2009).
83. P. Artal, A. Guirao, E. Berrio, and D. R. Williams, "Compensation of corneal aberrations by the internal optics in the human eye," *Journal of Vision* **1**, 8 (2001).

84. S. SC, H. D. F.A., B. W. BS, T. WB, T. DJ, M. PA, and S. A., "Wavefront Guided LASIK for the Correction of Primary Myopia and Astigmatism: A Report by the American Academy of Ophthalmology," *Ophthalmology* **115**, 14 (2008).

Biography

Mingtao Zhao is a Chinese, married and has a happy family. Mingtao was born in Yantai, Shandong province, China. He received a master degree and bachelor degree from Xi'an Jiaotong University and Shandong University respectively. "Become A Better You" ___Joel Osteen.

Thesis Publications

Patents

1. M. Zhao, A. N. Kuo, and J. A. Izatt, "Computation and Generation of Clinical Parameters for Anterior Segment Optical Coherence Tomography.", U.S. Provisional patent application, Sept 15, (2009).
2. M. Zhao, A. N. Kuo, and J. A. Izatt, "Quantitative 3D image correction and clinical parameter computation in optical coherence tomography", U.S. Provisional patent application No.61/175, 170, May 4, (2009).
3. M. Zhao, H. C. Hendargo, and J. A. Izatt, "Synthetic wavelength-based phase unwrapping in Fourier domain optical coherence tomography", U.S. provisional patent application, Duke File No.3114 (2008).
4. Y. Tao, M. Zhao, and J. A. Izatt, "Methods, systems, and computer program products for removing undesired artifacts in Fourier domain optical coherence tomography (FDOCT) systems using integrating buckets", U.S. patent #0204762 (2008).

Peer Reviewed Journal Publications

1. M. Zhao, A. N. Kuo, and J. A. Izatt, "Extraction of clinical refractive parameters from spectral domain-optical coherence tomography of the cornea," Arch Ophthalmol (In preparation) (2009).
2. M. Zhao, A. N. Kuo, and J. A. Izatt, "In vitro group refractive index measurement of the human cornea at 840-nm wavelength using spectral domain optical

- coherence tomography", *Ophthalmic Surgery, Lasers & Imaging* (In preparation) (2009).
3. M. Zhao, A. N. Kuo, and J. A. Izatt, "3D refraction correction and extraction of clinical parameters from spectral domain optical coherence tomography of the cornea ", *Opt.Express*.(Submitted) (2009).
 4. M. Zhao and J. A. Izatt, "Single camera sequential scan based polarization sensitive SDOCT for retinal imaging", *Opt.Lett.* **34**, 3 (2009).
 5. H. C. Hendargo, M. Zhao, N. Shepherd, and J. A. Izatt, "Synthetic wavelength based phase unwrapping in spectral domain optical coherence tomography," *Opt.Express* **17**, 13 (2009).
 6. Y. Tao, M. Zhao, and J. A. Izatt, "High-speed complex conjugate resolved retinal spectral domain optical coherence tomography using sinusoidal phase modulation," *Opt.Lett.* **32**, 3 (2007).
 7. B. A. Bower, M. Zhao, R. J. Zawadzki, and J. A. Izatt, "Real-time spectral domain Doppler optical coherence tomography and investigation of human retinal vessel autoregulation," *J.Biomed. Opt.* **12**, 8 (2007).
 8. R. Zawadzki, J. Steven, O. Scot, M. Zhao, B. Bradley, J. A. Izatt, S. Choi, S. Laut, and J. Werner, "Adaptive-optics optical coherence tomography for high-resolution and high-speed 3D retinal in vivo imaging," *Opt.Express* **13**, 15 (2005).

Conference Oral Presentations

1. M. Zhao, A. N. Kuo, and J. A. Izatt, "Extraction of clinical refractive parameters from spectral domain-optical coherence tomography of the cornea," *Photonic West 2010*(Accepted) (2009).
2. M. Zhao, A. N. Kuo, and J. A. Izatt, "Three-dimensional refraction correction and Zernike polynomial aberration decomposition for high-speed corneal spectral domain OCT " *Photonic West 2009 Ophthalmic Technologies XIX*(2009).
3. M. Zhao, Y. Tao, and J. A. Izatt, "Single channel high-speed polarization sensitive retinal SDOCT," *Photonic West 2008 Ophthalmic Technologies XIX*(2008).

4. M. Zhao and J. A. Izatt, "Simplified single channel high-speed polarization sensitive retinal SDOCT," Biomedical Optics (BIOMED) 2008 paper: BWF7 (2008).

Conference Posters

1. M. Zhao and J. A. Izatt, "Quantitative measurement of degree of polarization of retinal layers and retinal pigment epithelium segmentation using single camera based polarization sensitive SDOCT " Invest. Ophthalmol. Vis. Sci.E-Abstract (2009).
2. M. Zhao, Y. Tao, and J. A. Izatt, "High-speed fiber-based polarization sensitive retinal SDOCT," Invest. Ophthalmol. Vis. Sci. E-Abstract **48**(2007).

Conference Proceedings and E-Abstracts

1. M. Zhao and J. A. Izatt, "Quantitative measurement of degree of polarization of retinal layers and retinal pigment epithelium segmentation using single camera based polarization sensitive SDOCT " Invest. Ophthalmol. Vis. Sci.E-Abstract (2009).
2. A. N. Kuo, M. Zhao, and J. A. Izatt, "Corneal aberration measurement with three-dimensional refraction correction for high-speed spectral domain optical coherence tomography," Invest. Ophthalmol. Vis. Sci.E-Abstract (2009).
3. H. C. Hendargo, M. Zhao, N. Shepherd, and J. A. Izatt, "Synthetic wavelength-based phase unwrapping for nanoscale cellular profiling with spectral domain phase microscopy," Novel Techniques in Microscopy (2009).
4. H. C. Hendargo, M. Zhao, N. Shepherd, and J. A. Izatt, "Synthetic wavelength-based phase unwrapping in Fourier domain optical coherence tomography " Photonic West 2009 **7168**(2009).
5. M. Zhao and J. A. Izatt, "Simplified single channel high-speed polarization sensitive retinal SDOCT," Biomedical Optics (BIOMED) 2008 paper: BWF7 (2008).
6. M. Zhao, Y. Tao, and J. A. Izatt, "High-speed fiber-based polarization sensitive retinal SDOCT," Invest. Ophthalmol. Vis. Sci. E-Abstract **48**(2007).

7. Y. Tao, M. Zhao, C. A. Toth, and J. A. Izatt, "High-speed complex conjugate resolved retinal spectral domain optical coherence tomography," *Invest. Ophthalmol. Vis. Sci.E-Abstract* **48**(2007).
8. Y. Tao, M. Zhao, and J. A. Izatt, "Complex conjugate resolved retinal SDOCT using integrating buckets," *Proc. SPIE* **6429**, 4 (2007).
9. R. J. Zawadzki, S. M. Jones, M. Zhao, S. S. Choi, S. S. Laut, S. S. Olivier, J. A. Izatt, and J. S. Werner, "Adaptive optics/optical coherence tomography for in vivo retinal imaging: comparative analysis of two wavefront correctors," *Proc. SPIE* **6079**, 9 (2006).
10. R. J. Zawadzki, S. M. Jones, M. Zhao, S. S. Choi, S. S. Laut, S. S. Olivier, J. A. Izatt, and J. S. Werner, "Adaptive optics-optical coherence tomography for in vivo retinal imaging: effects of spectral bandwidth on image quality," *Proc. SPIE* **6138**, 9 (2006).
11. R. J. Zawadzki, S. M. Jones, M. Zhao, S. S. Choi, S. Laut, B. A. Bower, S. S. Olivier, J. A. Izatt, and J. S. Werner, "3D retinal imaging with video-rate adaptive optics optical coherence tomography," *Invest. Ophthalmol. Vis. Sci.E-Abstract* **47**(2006).
12. R. J. Zawadzki, A. R. Fuller, M. Zhao, D. F. Wiley, S. S. Choi, B. A. Bower, B. Hamann, J. A. Izatt, and J. S. Werner, "3D OCT imaging in clinical settings: toward quantitative measurements of retinal structures," *Proc. SPIE* **6138**, 11 (2006).
13. B. A. Bower, M. Zhao, and J. A. Izatt, "Investigation of retinal vessel autoregulation using real-time spectral domain Doppler optical coherence tomography," *Proc. SPIE* **6079**, 4 (2006).
14. R. J. Zawadzki, S. Laut, M. Zhao, S. Jones, S. Olivier, J. A. Izatt, and J. S. Werner, "Retinal imaging with adaptive optics high speed and high resolution optical coherence tomography," *Invest. Ophthalmol. Vis. Sci.E-Abstract* **46**(2005).
15. R. J. Zawadzki, S. Laut, J. S. Werner, S. M. Jones, S. S. Olivier, M. Zhao, B. Bower, and J. A. Izatt, "Adaptive-optics high-resolution and high-speed retinal in vivo Fourier domain OCT," *European Conference on Biomedical Optics (ECBO)* (2005).

16. R. J. Zawadzki, S. Choi, S. Laut, J. S. Werner, S. M. Jones, S. S. Olivier, M. Zhao, B. A. Bower, and J. A. Izatt, "Adaptive-optics optical coherence tomography for high-resolution and high-speed in vivo retinal imaging," Proc. SPIE **5861**, 8 (2005).
17. R. J. Zawadzki, B. A. Bower, M. Zhao, M. Sarunic, S. Laut, J. S. Werner, and J. A. Izatt, "Exposure time dependence of image quality in high-speed retinal in vivo Fourier domain OCT," Proc. SPIE **5688**, 8 (2005).
18. S. Werner, R. J. Zawadzki, M. Zhao, and J. A. Izatt, "Three dimensional retinal imaging with high speed and high resolution OCT," Invest. Ophthalmol. Vis. Sci.E-Abstract **46**(2005).
19. Z. Hu, M. Zhao, J. A. Izatt, and A. M. Rollins, "Enhancement of FDOCT imaging range by sub-pixel spectral shifting," Conference on Lasers and Electro-Optics, CLEO **3**, 3 (2005).
20. B. A. Bower, M. Zhao, Y. Wang, A. Chu, R. J. Zawadzki, M. V. Sarunic, and J. A. Izatt, "Rapid volumetric imaging of the human retina in vivo using a low-cost spectral domain optical coherence tomography system," Proc. SPIE **5690**, 6 (2005).
21. B. A. Bower, M. Zhao, A. Chu, R. J. Zawadzki, C. Toth, and J. A. Izatt, "Rapid volumetric imaging of the human retina in vivo using a low-cost, spectral domain optical coherence tomography system," Invest. Ophthalmol. Vis. Sci.E-Abstract **46**(2005).
22. S. Alam, R. J. Zawadzki, M. Zhao, C. Gerth, J. A. Izatt, L. S. Morse, and J. S. Werner, "Comparison of time-domain (OCT-3) and Fourier-domain optical coherence tomography in imaging macular diseases," Invest. Ophthalmol. Vis. Sci.E-Abstract **46**(2005).